
Linking intercellular forces to colony dynamics and fitness in bacterial populations

---

Inaugural-Dissertation

zur Erlangung des Doktorgrades
der Mathematisch-Naturwissenschaftlichen Fakultät
der Universität zu Köln

vorgelegt von

Robert Zöllner

aus Mettingen

Köln 2019

Berichterstatter:	Prof. Dr. Berenike Maier
(Gutachter)	Prof. Dr. Tobias Bollenbach

Tag der mündlichen Prüfung: 21.02.2019

CONTENT

1 ZUSAMMENFASSUNG

Die Bildung von Biofilmen ist ein kollektives Phänomen prokaryotischer Systeme. Zellen zeigen in Biofilmen eine erhöhte Widerstandsfähigkeit gegen Umweltstress. Bakterien können Typ 4 Pili (T4P) zur aktiven Krafterzeugung, Adhäsion und Bildung von Biofilmen verwenden. Der erste Teil dieser Arbeit konzentriert sich auf Einzelzellwechselwirkungen die durch T4P vermittelt werden. Diese T4P-Wechselwirkungen werden mit Hilfe von Laserpinzetten quantifiziert und mit der kollektiven Dynamik junger Biofilme verknüpft. Der zweite Teil dieser Arbeit konzentriert sich auf das Zusammenspiel von T4P-Einzelzellwechselwirkungen, deren Evolution und der Struktur makroskopischer Biofilme. Genom-Sequenzierung wird mit phänotypischen Analysen kombiniert, um Mutationen mit interbakteriellen Wechselwirkungen und kollektiven Phänomenen zu verknüpfen.

Mit einer dualen Laserfalle haben wir gezeigt, dass die Wartezeitverteilung von Zell-Zell-Interaktionsereignissen mit der Wartezeitverteilung von Zell-Kugel-Interaktionsereignissen vergleichbar ist. Monomere der T4P werden posttranslational modifiziert. Wir beobachten, dass interzelluläre Abreiskräfte und Bindungskinetiken durch Pilin-Glykosylierungs- und Phosphoform-Modifizierungen reguliert werden. Darüber hinaus ändern sich die interzellulären Bindungskinetiken mit variierender T4P-Motoraktivität. Diese mikroskopischen Befunde werden mit Ergebnissen mesoskopischer multizellulärer Systeme verknüpft. Unsere Daten zeigen, dass eine Änderung der Abreisskräfte und der Bindungswahrscheinlichkeiten die Zellsortierung induziert. Die Fusionsdynamik von multizellulären Systemen zeigt flüssigkeitsähnliches Verhalten. T4P-Wechselwirkungskinetiken regulieren diese Dynamik und beeinflussen die Materialeigenschaften Oberflächenspannung und Viskosität.

Lange wurde angenommen, dass die T4P-vermittelte Krafterzeugung an die Retraktions-ATPase PilT gekoppelt ist, welche für Oberflächenmotilität und multizelluläre Dynamik unerlässlich ist. Wir beobachten jedoch, dass die Kraftgenerierung durch T4P-Retraktion auch ohne die Retraktions-ATPase PilT erfolgt. Wir zeigen, dass die Retraktion ohne PilT

unabhängig von der protonenmotorischen Kraft und den *pilT*-Paralogen *pilU* und *pilT2* ist. Die Retraktion ist zwei Größenordnungen langsamer als *pilT*-getriebene Retraktion und stoppt bereits bei Gegenkräften von unter 10 pN. Außerdem hängt die Geschwindigkeit der *pilT*-unabhängigen T4P-Retraktion von der anliegenden Gegenkraft und der periplasmatischen PilE-Konzentration ab.

Frühere Studien haben gezeigt, dass die Positionierung einzelner Zellen in Biofilmen die Ausbreitung, das Wachstum, den Nährstoffverbrauch und den kollektiven Schutz vor Umwelteinflüssen bestimmt. Wir untersuchen, ob T4P-Interaktionskräfte die Positionierung und die Populationsdynamik expandierender Biofilme beeinflussen. Unsere Daten zeigen, dass schwach wechselwirkende Zellen ohne T4P an die Außenschicht wachsender Populationen segregieren und dort einen starken selektiven Vorteil erlangen. Räumliche aufgelöste Sequenzierung zeigt, dass antigenische- und Phasen-Variation der Pili Diversität von Pilin-Sequenzen erzeugen und Zellsortierung bedingen.

In Flüssigmedium evolvierende Populationen bevorzugen disperse Anordnungen gegenüber dichter Aggregation und können dennoch T4P zur aktiven Krafterzeugung nutzen. Sequenzierung des gesamten Genoms zeigt, dass Mutationen in *pilC* und *pilE* aller Wahrscheinlichkeit nach an der Veränderung interzellulärer T4P-Wechselwirkung beteiligt sind und disperse Anordnungen zu ermöglichen.

Zusammenfassend lässt sich sagen, dass verschiedene posttranslationale Modifikationen und eine Veränderung der Motoraktivität die attraktive T4P-Wechselwirkung optimieren. Veränderte Einzelzellwechselwirkungen wirken sich auf Zellgemeinschaften aus und haben drastische Auswirkungen auf die Materialeigenschaften multizellulärer Systeme. Die Untersuchung der Retraktion von T4P in Abwesenheit von PilT weist darauf hin, dass die nicht angetriebene Depolymerisation ein universelles Phänomen der T4P ist. Unsere Ergebnisse weisen darauf hin, dass T4P-Wechselwirkungen einer raschen evolutionären Entwicklung unterliegen, die es den Zellen ermöglicht, Aggregation zu verändern, anzupassen und auf Umgebungsbedingungen zu reagieren.

2 ABSTRACT

Biofilm formation is a collective phenomenon of prokaryotic systems. Within biofilms cells show enhanced resistance against environmental stresses. Bacteria can use type 4 pili (T4P) for active force generation, adhesion and formation of biofilms. The first part of this work focusses on T4P-mediated single cell interactions. These interactions are quantified by means of laser tweezers and connected to dynamics of early biofilms. The second part of this work focusses on the interplay of T4P-mediated single cell interactions, evolution and structure of macroscopic biofilms. Genome sequencing in combination with phenotypic analysis is used to connect mutations to interbacterial interaction and collective phenomena.

Using a dual laser trap, we showed that the waiting time distribution of cell-cell interaction events is comparable to the waiting time distribution of cell-bead interaction events. Monomers of T4P are post-translationally modified. We observe that cell-cell rupture forces and binding kinetics are fine-tuned by pilin glycosylation and phosphoform modification pathways. In addition, intercellular binding kinetics change with varying T4P-motor activity. These microscopic findings are correlated with results from mesoscopic multicellular systems. Our data indicate that diversification of rupture forces and binding probabilities induces cell sorting. Fusion dynamics of multicellular aggregates shows liquid-like behavior. T4P-mediated interaction kinetics regulate these dynamics and strongly affect the material properties surface tension and viscosity.

For a long time T4P mediated force generation was thought to be coupled to the retraction ATPase PilT, which is essential for twitching motility and multicellular dynamics. However, we observed that force generation by T4P retraction occurs without retraction ATPase PilT. We demonstrate that retraction in the absence of PilT is independent of proton motive force and of the *pilT*-paralogues *pilU* and *pilT2*. Retraction is two orders of magnitude slower than *pilT*-driven T4P retraction and stalls frequently at opposing forces smaller than 10 pN. Furthermore, the velocity of *pilT*-independent T4P retraction depends on the opposing force and the periplasmatic PilE-concentration.

Previous studies show that positioning of individual cells within biofilms governs dispersal, growth, nutrient consumption and collective protection against environmental stresses. We tested whether tuning of T4P-mediated interaction forces governs positioning and affects population dynamics of expanding biofilms. Our data shows that weakly interacting cells without T4P segregate to the periphery of growing populations and show a strong selective advantage. Spatially resolved sequencing demonstrates that pilin antigenic- and phase-variation are natural mechanisms that generate a standing diversity of pilin sequences within the populations and cause segregation of subpopulations.

Populations evolving in liquid medium favor dispersive arrangements over dense aggregation while maintaining their ability to use T4P for active force-generation. Whole genome sequencing data suggests, that mutations in *pilC* and *pilE* are likely to be involved in changing intercellular T4P-mediated interactions as to enable disperse arrangements.

In conclusion, different pilin post-translational modifications and variations in motor activity fine-tune attractive T4P-mediated interactions. Altered single-cell interactions affect cell communities and have drastic effects on material properties of multicellular systems. Investigation of T4P retraction in the absence of *pilT* indicates that PilT-independent T4P retraction is a universal T4P phenomenon. Our results suggest that T4P-mediated interactions are subject to rapid evolution, which enables cells to change and adjust aggregation, and react to environmental conditions.

3 INTRODUCTION

Biological systems have evolved to enormous complexity on various time and length scales. The largest isogenic organisms, for instance, cover distances of several kilometers and areas of up to 9.7 square kilometers [1][2][3]. In contrast to that, there are viruses that only consist of approximately 958,980 single atoms [4][1].

Bacteria are micrometer-sized organisms which live at low Reynolds-numbers, where viscous forces dominate over inertia [5]. In this environment, many bacterial species have developed microscopic machines that enable them to interact with each other and perform active movement in liquids or on surfaces. Bacterial communities often comprise of large numbers of individual cells. In order to study collective phenomena such as swarming or auto-aggregation in a biophysical context, it is often convenient to treat single cells as single particles [6][7][8][9]. As such, the individual properties of single cells and their interactions have been shown to determine the behavior and structure of collective communities [10][11][12]. Recently, it was demonstrated that molecular machines involved in cell-cell interaction have the potential to directly regulate dynamics of cellular communities in space and time [12][13]. However, the question of how bacteria control their molecular machines and cell-cell interactions in order to regulate collective dynamics remains unclear. This study addresses this question and investigates physical properties of single cells, their interactions and their relevance for collective traits. To this end, we studied *Neisseria gonorrhoeae*, an organism that regulates collective behavior using type 4 pili (T4P).

The first part of the introduction provides an overview of different types of collective behavior in bacterial systems and the molecular motors involved. In second section, an overview of force generation of molecular motors, in particular the T4P-machinery will be given to provide a basic understanding of single cell dynamics of our applied model system. Subsequently, variation of T4P-mediated interactions by genetic and post-translational modifications will be explained. The next paragraph focusses on multicellular communities and introduces important aspects of biofilms and spatial organization within cellular communities. The final part links the evolutionary factors selection, mutation and genetic drift to bacterial communities.

3.1 MOLECULAR MOTORS GOVERN COLLECTIVE BEHAVIOR OF BACTERIAL SYSTEMS

Many bacterial species have evolved extracellular structures that enable physical interactions with their environment and other bacteria. They include pili, focal adhesions, curli, flagella, and exopolysaccharides. From a biophysical point of view pili and flagella are particular interesting because they function both as adhesins and are driven by molecular motors enabling complex collective dynamics of bacterial populations. Some species including *Pseudomonas aeruginosa* and some *Escherichia coli* strains produce both flagella and type 4 pili (T4P). Other species generate only a single type of motor.

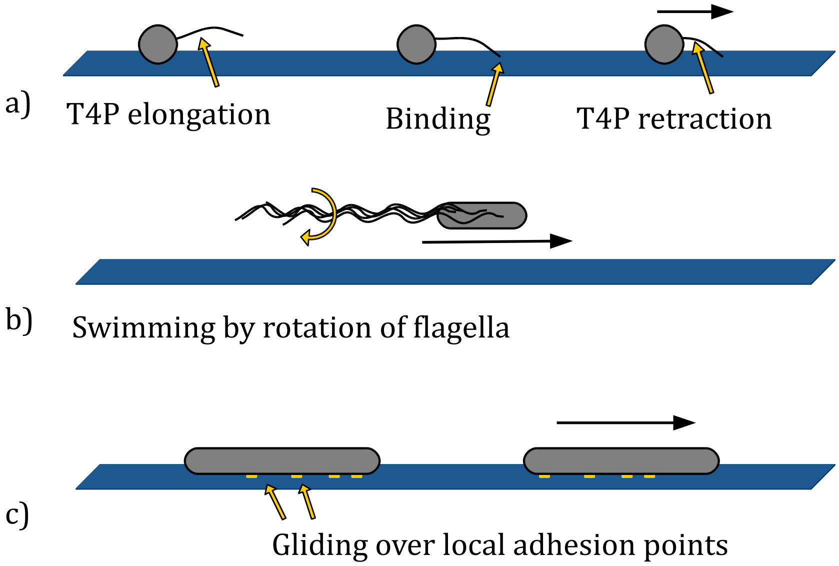

Figure 1: Molecular motors are used for bacterial motility. a) Twitching motility. The T4P-machinery generates propulsive forces by sequential elongation, binding and retraction of T4P. b) Swimming motility. The flagellar rotary motor propels bacteria through aqueous environment or on moist surfaces. c) Gliding motility. Molecular motors are fixed in focal adhesion points and push the cell-body along a helical trajectory.

Many bacterial species use the (de-)polymerization motor of T4P to interact with surfaces and other bacteria. On surfaces, T4P-mediated twitching motility is performed by periodic cycles of polymerization (T4P elongation), binding, depolymerization (T4P retraction) and rupture events [14] (Figure 1a). Both *Neisseria gonorrhoeae* and *Synechocystis* exclusively use type 4 pili (T4P) to interact with the environment. Single cells are able to move over surfaces via T4P. In addition to surface motility cells can use their pili to exert forces on adjacent cells. These forces are applied in a tug-of-war mechanism until intercellular bonds rupture. Collectively, these single-cell interaction patterns lead to auto-aggregation of gonococci (Figure 2) [15]. While there is no evidence for tactic behavior of *N. gonorrhoeae*, T4P driven cellular dynamics are regulated by chemotaxis or phototaxis in other species [16][17]. In case of photosynthetic *Synechocystis* it was shown that the subcellular location of pilus production can be manipulated by light [18]. Interestingly, these cells move collectively towards light sources in regular, finger-like projections [17]. This collective motion depends on the direct physical interactions between bacteria, mediated through their T4P [19].

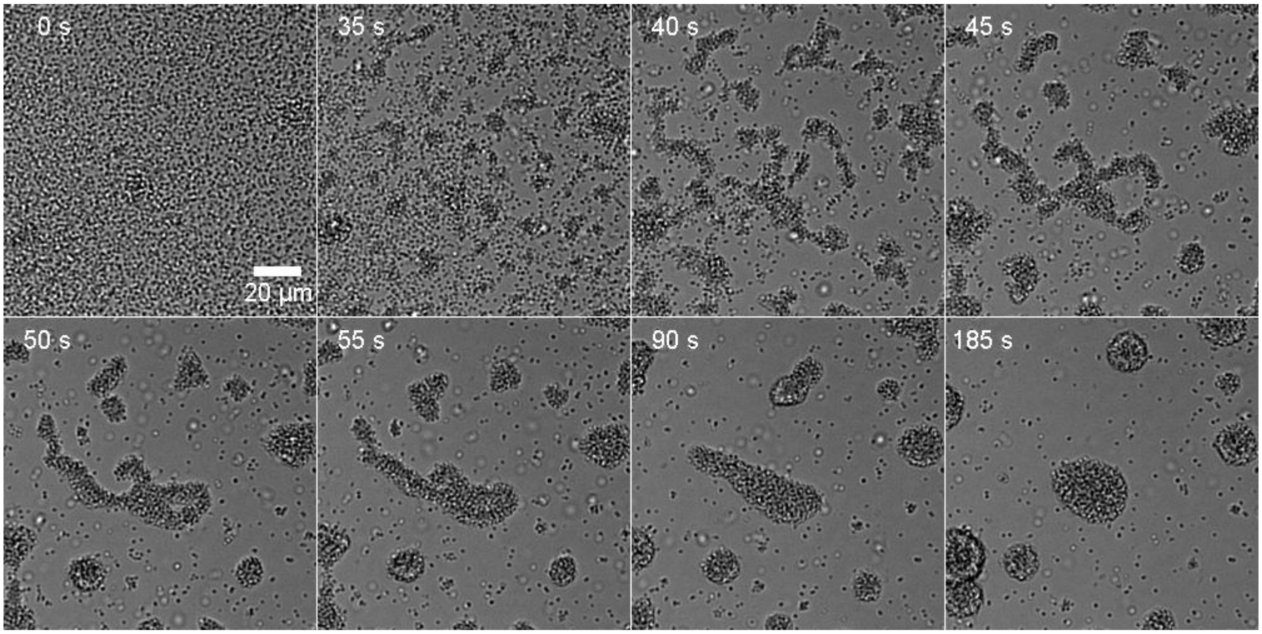

Figure 2: Auto-aggregation of *N. gonorrhoeae*. Well mixed and homogeneously distributed cells were inoculated in a flow chamber (t = 0 s). Oxygen supply triggers T4P-mediated self-assembly and generation of spherical colonies within 185 seconds. (Imaging was done by Tom Cronenberg.)

Different bacterial species use rotating flagella for directed movement in liquid environments. These extracellular filaments are rotated clock-wise or counter clock-wise by a rotary molecular motor [20][21]. Depending on the flagellas' direction of rotation the cells swim straight or change direction by tumbling [22] (Figure 1b). *E. coli* and *Bacillus subtilis* use flagella to swim or swarm. Both species employ their flagella during chemotaxis [23]. Communities of *B. subtilis*, function as model systems for a behavior called swarming. Here, highly mobile cells use their flagella to move collectively over surfaces in a dendrite shaped morphology [24] (Figure 3). Swarming has several phases and is induced by hyperactive swimmers. Pattern formation depends on the presence of surfactin molecules that are produced by the cells. Interestingly, dendrite formation of *B. subtilis* is tightly regulated and depends on nutrient supply and temperature [25][26].

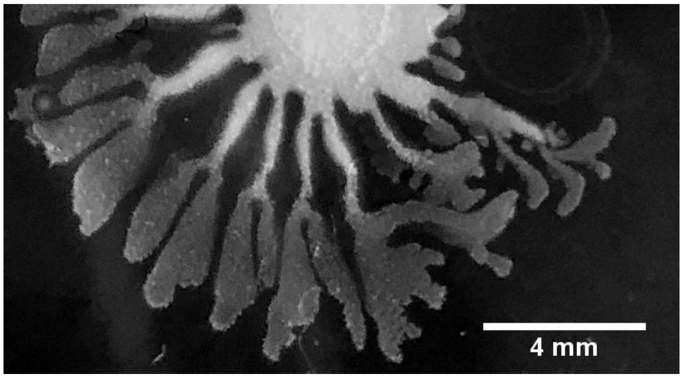

Figure 3: Swarming of *B. subtilis*. A population of *B. subtilis* was inoculated on an agar plate (white circle). After 24 h of growth dendrites have formed due to collective motion of cells. (The image was acquired by Thorsten Volkmann.)

A species that uses both molecular machineries, flagella as well as T4P to interact with the environment is *Pseudomonas aeruginosa*. The cells swim in liquid environments by utilizing their flagella-machinery. Their T4P enable *P. aeruginosa* to interact with adjacent cells and bind to surfaces [27]. Cells are able to swarm on wet surfaces. T4P influence flagella-driven swarming behavior in *P. aeruginosa*, whereby T4P-mediated cell-cell contact slows down expansion of swarming colonies [28]. Interestingly, this swarming-ability is linked to virulence and antibiotic resistance [29]. The combination of flagella and T4P machineries makes *P. aeruginosa* highly versatile and a primary target to study complex collective behavior [30][31].

The species *Myxococcus xanthus* uses T4P but combines it with gliding-motility to move over surfaces. The molecular motors that drive gliding are linked to the bacterial cytoskeleton. These motors generate a propulsive force by moving along a helical counterclockwise trajectory around the cell contour [32][33]. The machinery is fixed in focal adhesion points and pushes the cell in a screw-like fashion (Figure 1c). Collective gliding motility is used for swarming and aggregation into fruiting bodies [34][35].

3.2 CHARACTERIZING T4P INTERACTIONS: MOLECULAR MOTORS, T4P AND OPTICAL TWEEZERS

The previous section introduced different molecular motors present in various species and emphasized their importance for collective behavior. Now, we will focus on the type 4 pilus (T4P) motor of *N. gonorrhoeae* as this was used throughout this study to investigate intercellular forces and their relevance for collective behavior. In the following section, an overview of force generation by molecular motors, in particular the T4P-machinery will be given to provide a basic understanding of single cell dynamics of our applied model system. In addition, important aspects of optical tweezers will be introduced as this method was employed for in vivo characterization of T4P-mediated single cell interactions.

3.2.1 Force generation by molecular motors

Biological cells generate mechanical forces using molecular machines. These convert chemically stored energy into mechanical work by for example using ion-gradients across membranes. Besides this, many motors use the hydrolysis of ATP as energy source where ATP is converted to ADP [36]. ATP hydrolysis generates ADP and a phosphate P. The free energy change of this reaction is concentration dependent and given by

$$\Delta G = \Delta G_0 + k_B T \ln\left(\frac{[ADP][P]}{[ATP]}\right), \tag{1}$$

where $\Delta G_0 = -k_B T \ln(\prod_i c_{i,eq}^{\nu_i})$ with the stoichiometric coefficient ν_i counting the number of the i-th particle type during the retraction and the standard state concentration $c_{i,eq}$ [37]. Typical values of free energy provided by ATP hydrolysis are in the range of $\Delta G \approx 20 k_B T \approx$ 80 pNnm [37].

Looking at the level of single molecules, the example of ATP hydrolysis shows that molecular motors operate in discrete (energy) steps. On these scales, thermodynamic fluctuations are dominating and strongly affect (and even enable) the driving of molecular machines [38]. A basic approach to the theoretical understanding of molecular motors is the one-state model and diffusion along a free energy landscape. If one considers a motor moving along a periodic track or filament with local energetic minima, the transition rates $k_\pm$ to move from position

n to $n \pm 1$ are functions of the surrounding energy landscape and dependent on the adjacent energy barriers $\Delta G_{\pm}$. $k_{\pm}$ are the inverse average times the motor needs to diffuse over the barrier and step in positive/negative direction. A detailed description of transition rates is given in [39]. The system moves along a tilted landscape along local minima and uses the energy ΔG_{ATP} provided by ATP hydrolysis to jump from position n to $n+1$ with increased probability. One can use rate equations to derive that under an applied external force F the transition rates fulfil the relation

$$\frac{k_+}{k_-} = \exp[-\beta(\Delta G + Fa)] \tag{2}$$

[37]. Equivalent statements can be derived for molecular motors with an arbitrary number of transitions [40]. The velocity of the motor is given by $v = a(k_+ - k_-)$. In the special case of the external force reaching the stalling force where $Fa = \Delta G$, one finds $k_+ = k_-$. In the context of energy landscapes, this is understood as a tilted landscape so that $\Delta G_+ = \Delta G_-$. This makes transitions in positive and negative direction equally likely, resulting in no net movement.

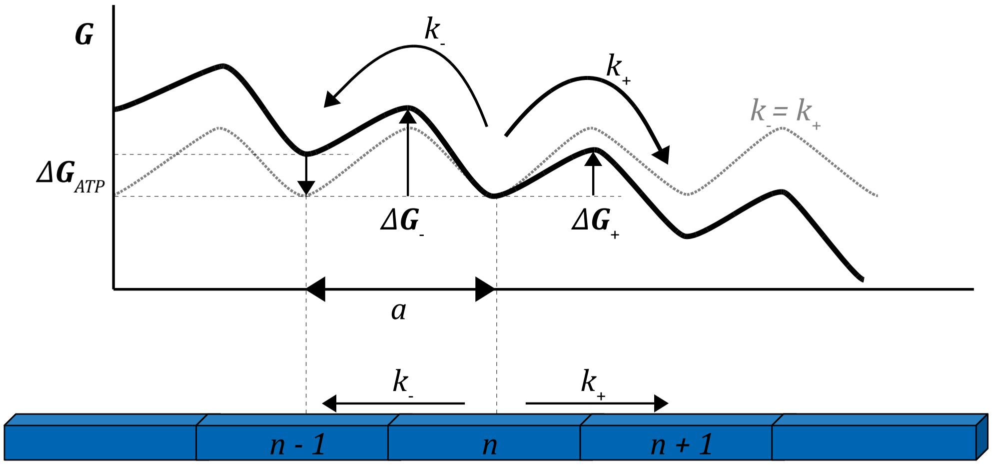

Figure 4: Free energy landscape of an one-state motor moving along a track/filament (blue). The discrete positions along the track are labeled by n. A tilt of the free energy landscape increases the transition rate k_+ and forces the motor to the right. Forward and backward rates depend on the barrier height $\Delta G_{\pm}$. In case of an opposing external force the landscape tilts until movement stops because of equal transition rates $k_+ = k_-$ (grey dashed line).

The simple one-state motor model can be generalized by including sub transitions with proper energy levels and transition rates [40]. This enables modeling of motors that exhibit arbitrary subsequent transitions, for example between conformational changes, prior to mechanical movement. However, sub-steps often occur fast and thus only the rate-limiting step of the motor cycle can be resolved for some motors including the bacterial flagella motor [41].

3.2.2 The Type 4 Pilus machinery

In the previous paragraph it was described how ATP hydrolysis drives complex molecular motors. The T4P is a molecular motor that uses ATP hydrolysis and generates forces by cycling through multiple transition states while utilizing the complex interplay of several proteins.

The motor complex is located in the membrane of the bacteria and consists of multiple proteins [14][42]. In the following description we follow the nomenclature of *N. gonorrhoeae*. The pilus fiber consists of the major pilin PilE and various minor pilins. The T4P is connected to the inner membrane protein PilG and extends into the extracellular milieu via the outer membrane pore PilQ. Interestingly it was suggested that PilG is able to perform rotational motion. Due to the helical geometry of the pilus fibre, clockwise rotation would insert and counterclockwise rotation would remove pilin subunits. The two hexameric ATPases PilF and PilT fuel elongation and retraction, respectively. Both contain a Walker A motif involved in ATP binding and a Walker B motif involved in ATP hydrolysis [43]. Notably, it was proposed that clockwise nucleotide-driven conformational deformations of the hexameric assembly ATPase PilF and counterclockwise deformation of the disassembly ATPase PilT drive rotation of PilG in opposite directions [44]. PilC is associated with adhesion and was proposed to be located at the tip of T4P [45][46]. However, its precise function remains unclear.

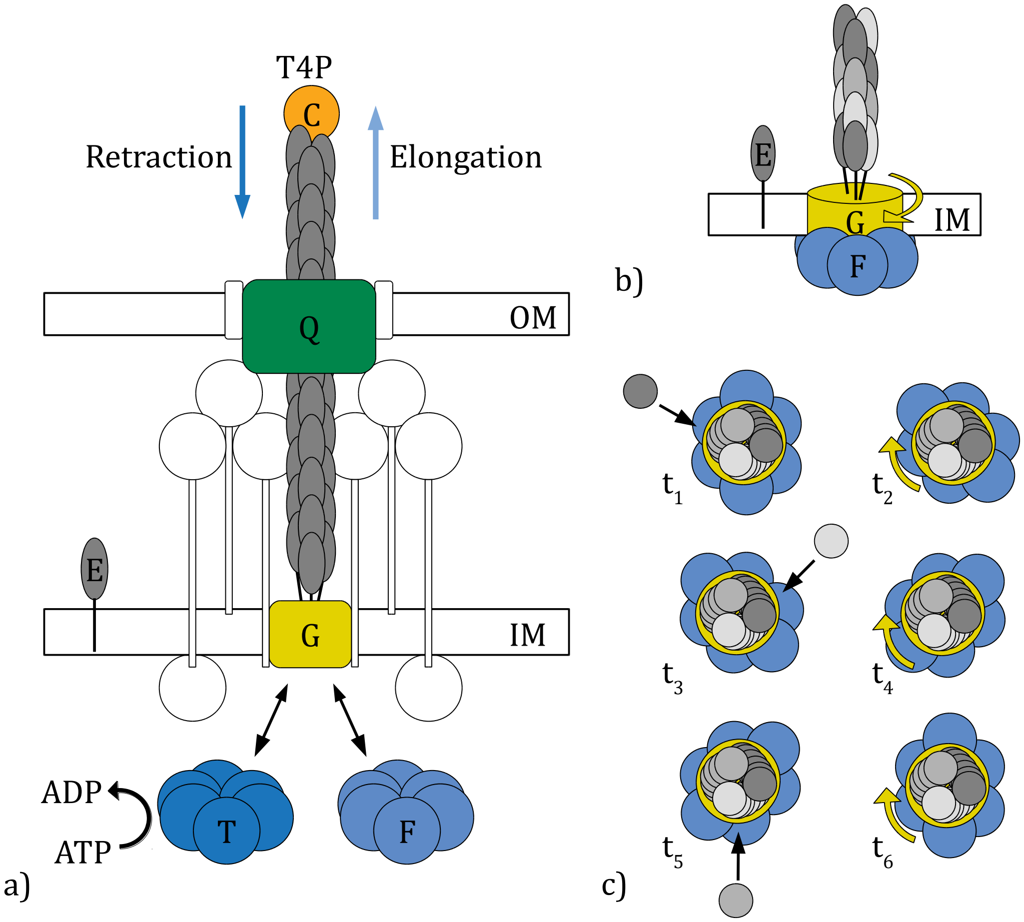

Figure 5: Type 4 pilus (T4P) machinery. a) The T4P-machinery is located in inner (IM) and outer membrane (OM). The T4P interacts with the IM protein PilG and passes the OM via the pore PilQ. The pilus fiber consists of PilE proteins that are assembled into the pilus by the ATPase PilF. As a consequence, the polymerized T4P elongates. The ATPase PilT depolymerizes and retracts the T4P. PilC is associated with pilus assembly and has been shown to be located in the extracellular milieu. b) A rotary mechanism was proposed for T4P elongation/retraction: For elongation, PilF is bound to the PilG complex and generates clockwise rotation of PilG. As a consequence, PilE is 'scooped' into the non-rotating fiber. Different grey tones of equal PilE proteins highlight the helical structure of the pilus fiber. c) Top view of (b) at various points in time: The PilG complex rotates within the inner membrane relative to the ATPase, which is fixed. Clockwise ring conformational deformation in the assembly ATPase PilF drives clockwise rotation of PilG and the polymerization of the non-rotating pilus fiber.

Many different bacterial species generate T4P. They use the T4P machinery to generate mechanical forces and interact with the environment [14][27][47]. Importantly, T4P mediate attractive interactions with adjacent cells. This is a key feature for aggregation and adhesion in various species [48]. The T4P (de-)polymerization machinery is among the strongest molecular motors known [47][49]. Generation of high forces by T4P is a conserved property between species [50]. For our model organism *N. gonorrhoeae,* it was discovered that force and velocity can be approximately described by the empirical formula

$$v(F) = v_{max}\left(1 - \frac{F}{F_S}\right), \tag{3}$$

where F_S is the stalling force and v_{max} the maximum velocity [47]. Notably, it was demonstrated that the pilus machinery can show different velocity regimes [51][52]. Gonococcal T4P dynamics and force generation are important for interactions with adjacent cells, host cells and surfaces (Figure 1) [53][54]. On flat surfaces, piliated cells perform a two-dimensional correlated random walk (Figure 6) [55]. It was demonstrated that twitching motility is coordinated by a two-dimensional tug-of-war mechanism with directional memory [53]. Pilus-mediated movement strongly depends on the stiffness and curvature of the surfaces [56][57]. Interestingly, recent reports show evidence that pili are used for surface detection [58][59]. However, the necessary signal transmission by T4P has not been shown directly and is subject to ongoing investigation.

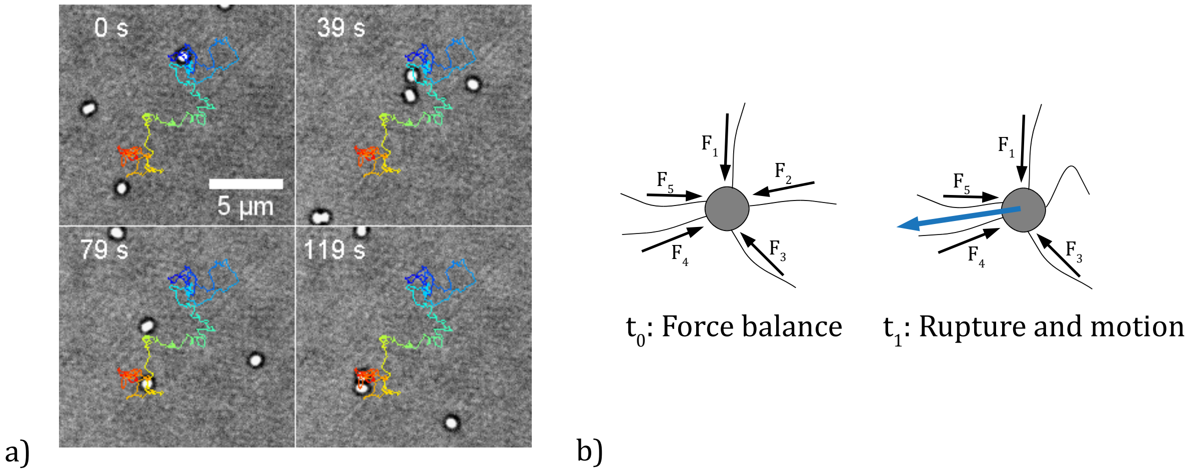

Figure 6: Twitching motility and the tug-of-war mechanism of *N. gonorrhoeae*. a) Using their T4P, cells perform a two-dimensional correlated random walk on surfaces. The track of one cell is shown. Time is color-coded: t = 0 s blue, t = 119 s red. b) Hypothetical arrangements of T4P. t_0: Five surface bound pili extend from a cell body and generate forces (black arrows) by pilus retraction. t_1: A pilus bond ruptures. As a consequence, a net force in the direction where most T4P are located generates cellular movement (blue arrow).

3.2.3 Characterizing T4P-mediated interactions with optical tweezers

As mentioned in the previous paragraph, T4P enable bacteria to interact with surfaces and other cells. In this study, we investigated cell-cell interactions mediated by the T4P machinery. Such motors generate forces in pico-newton range and move in nanometer sized steps. Optical tweezers are highly useful tools to measure these quantities. We utilized dual optical tweezers to characterize T4P-mediated interactions of *N. gonorrhoeae*. In the following, optical tweezers and the generation of multiple trapping potentials will be introduced.

Optical tweezers were pioneered by A. Ashkin and colleagues. In 1986 they reported the first controllable optical trap [60]. For his work on optical trapping, Ashkin received the Nobel Prize in 2018 [61]. Since the development of optical tweezers in the 1980s, enormous progress has been made enabling length measurements down to 1 Å [62]. The high accuracy and experimental flexibility of laser tweezers enables the characterization of molecular motors and sets this tool apart from other single molecule techniques including magnetic tweezers and atomic force microscopy (AFM) [14]. Additional techniques such as traction force microscopy (TFM) and elastomeric micro pillars have been established to quantify force-generation of migrating bacteria and reveal hidden epitopes of T4P [63][64].

Despite numerous improvements that have been accomplished over the years, optical tweezers are still subject of active research. Recent advances have been made by creating stable trapping potentials without high NA-objectives for trapping of single cells [65]. Furthermore, it was reported that the generation of multiple controllable traps within large areas allows for manipulation of microgranular materials [66].

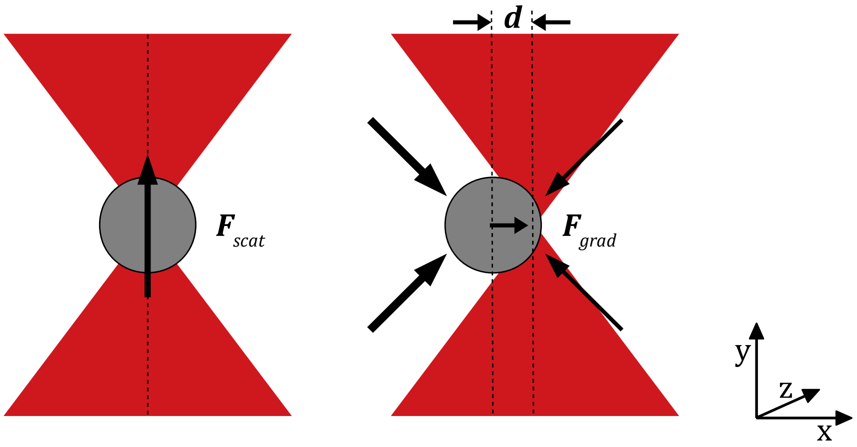

Figure 7: Principle of optical trapping. A strongly focused laser beam is shown in red. Two sketches illustrate the decomposition of the total force into two principal forces: Gradient force F_{grad} and scattering force F_{scat}. In case of a deflection d, F_{grad} leads to a restoring force that points towards the equilibrium position.

Optical traps use interaction of a focused light beam with dielectric particles to generate forces that keep the particle in the center of the beam. In literature these forces are commonly divided into a scattering force $\boldsymbol{F}_{scat}$ and a gradient force $\boldsymbol{F}_{grad}$ so that $\boldsymbol{F} = \boldsymbol{F}_{scat} + \boldsymbol{F}_{grad}$ [67] (Figure 7). $\boldsymbol{F}_{scat} < \boldsymbol{F}_{grad}$ is necessary for stable trapping in three dimensions [68]. There are analytical expressions for $\boldsymbol{F}_{scat}$ and $\boldsymbol{F}_{grad}$ that can be derived by assuming that the wavelength λ of the scattering light is much smaller ($\lambda \ll r$) or much longer ($\lambda \gg r$) than the radius of the trapped object. These regimes are commonly referred to as Mie- and Rayleigh-regime. However, for micro particles such as bacteria, these assumptions are generally not true and a more general description of the scattering process of the incident beam on the trapped object is necessary.

For particles in the Mie-regime $\lambda \ll r$ it is assumed, that the entire light beam can be decomposed into individual rays that propagate in straight lines with appropriate intensity and direction [69]. The scalar scattering and gradient force F_{scat} and F_{grad}, which are force-components parallel and perpendicular to the incident beam are given by

$$F_{scat} = \frac{n_1 P}{c}\left\{1 + R\cos(2\theta) - \frac{T^2[\cos(2\theta - 2\varphi) + R\cos(2\theta)]}{1 + R^2 + 2R\cos(2\varphi)}\right\} \tag{4}$$

and

$$F_{grad} = \frac{n_1 P}{c}\left\{R\sin(2\theta) - \frac{T^2[\sin(2\theta - 2\varphi) + R\sin(2\theta)]}{1 + R^2 + 2R\cos(2\varphi)}\right\}. \tag{5}$$

Here θ and φ are the angles of incidence and refraction, P is the power of the beam, n_1 is the refractive index of the surrounding medium and R and T are reflection and transmission coefficients.

For particles in the Rayleigh-regime $\lambda \gg r$ it is assumed, that the particle is a point-like dipole in an electromagnetic field. The vector scattering force $\boldsymbol{F}_{scat}$ points in the direction of beam propagation. The vector gradient force $\boldsymbol{F}_{grad}$ can be decomposed into components along the tree axes and points towards the focal point of the beam [67]. The forces are given by

$$\boldsymbol{F}_{scat} = \frac{8}{3}\pi(ka)^4 a^2\left(\frac{m^2 - 1}{m^2 + 2}\right)^2\left(\frac{n_2}{c}\right) I(\boldsymbol{r})\hat{\boldsymbol{e}}_{\boldsymbol{z}} \tag{6}$$

and

$$\boldsymbol{F}_{grad} = 2\pi n_2^2 \varepsilon_0 a^3 \left(\frac{m^2 - 1}{m^2 + 2}\right) \nabla I(\boldsymbol{r}) \,. \tag{7}$$

Here, a is the radius and $m = n_1/n_2$ is the relative refractive index (n_2 of the particle and n_1 of the medium), $k = 2\pi/\lambda$ is the wave number of the medium and I is the beam intensity.

It is necessary to create multiple traps in order to investigate for example stretched macromolecules independent of surface effects [62], or in our case, single cell interactions. In order to generate spatially independent trapping potentials there are several experimental possibilities. The simplest solution would be to install more than one trapping laser. However, this solution does not allow for straight forward manipulation of the traps once the lasers are aligned. Furthermore, polarization can be used in order to generate two optical traps [70]. Thereby, the trapping laser is split into two separate light paths. Individual control of each path allows for independent manipulation of each trap. Optical tweezers can be manipulated by installing spatial light modulators within the laser path [71]. This technique is called holographic optical tweezers and allows for splitting the laser beam into many individual traps that can be independently positioned [72]. We used an acousto-optic deflector (AOD) to generate two individual optical traps. Multiple trapping potentials can be created by utilizing AODs [68]. They are tunable diffraction gratings, where an excited sound wave propagates through the acousto-optic (AO) medium [73]. A typical AO-medium for infra-red trapping lasers is crystalline tellurium dioxide TeO_2, which is transparent at 1064 nm. In the AOD the wavelength of an excited sound wave corresponds to the grating constant. As a consequence, the angle at which the incident laser beam is deflected can be manipulated by changing the frequency of the sound wave. The first order angle of deviation can be described by

$$\theta = \frac{\lambda v}{\Lambda} = \frac{\lambda f}{v} \,, \tag{8}$$

where λ is the wavelength of the laser, Λ is the acoustic wavelength, f is the acoustic frequency and v is the acoustic velocity in the AO-medium [73]. In practice the AO-medium is excited by piezo elements which allow for electronic control and generation of acoustic waves up to GHz-regimes.

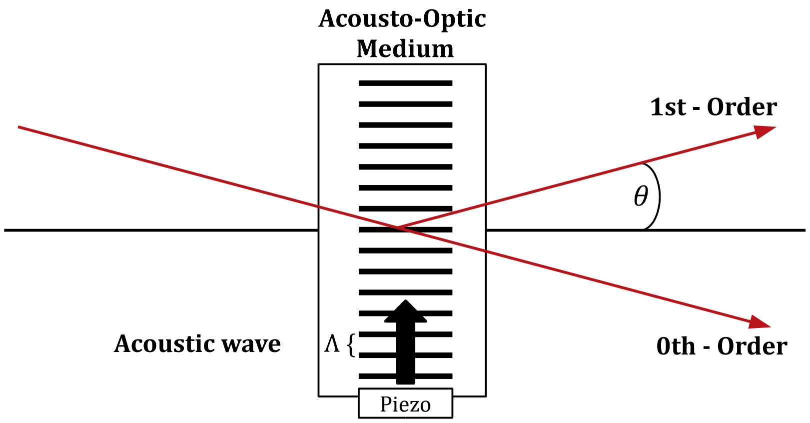

Figure 8: An AOD operated with a single acoustic frequency (wavelength Λ). The deflection angle θ can be adjusted by changing the frequency of the acoustic wave.

3.3 VARIATION OF T4P-MEDIATED INTERACTIONS

In the previous section we introduced the type 4 pilus and our experimental approach to characterize T4P-mediated intercellular interactions of *N. gonorrhoeae*. It is important to note that, specifically in our model organism *N. gonorrhoeae,* T4P are subject to continuous genetic variation. By means of pilin phase- and antigenic variation, T4P-assembly can be switched on and off. Moreover, antigenic variation has the power to fine-tune pilus-mediated interactions by changing the sequence of the major pilin. Furthermore, the mechanism of pilin post translational modification was shown to regulate pilus-mediated interactions. In the following pilin phase- and antigenic variation and pilin post translational modifications will be introduced.

3.3.1 Pilin phase- and antigenic variation

Many bacterial species use phase and antigenic variation to generate genotypic variation [74][75]. Both mechanisms are based on mutational variations within the genome and frequently target outer membrane structures, thus enabling bacteria to escape from immune surveillance [76][77][74]: Phase variation occurs by slipped-strand-mispairing mutations within homopolymeric stretches in the genome and antigenic variation occurs by recombination events where silent gene are (partially) copied into the native locus (Figure 9)[78]. *N. gonorrhoeae's* major pilin gene *pilE* is subject to both types of variation [79][80].

pilE can contain a poly-C stretch where addition or deletion of one base causes a slipped-strand-mispairing mutation switching the gene off (phase variation). A subsequent addition or deletion of one base switches the gene back on. In addition to that, the primary sequence of *pilE* is subject to sequence variation (antigenic variation) via partial recombination events from silent pilin loci (*pilS* genes) into the native *pilE* gene. These recombination events are irreversible and often lead to non-functional proteins or vice versa. Pilin antigenic variation is dependent on *recA* and a guanine quadruplex motif (G4) upstream of *pilE* [81]. While the importance of phase- and antigenic variation are known to be important for bacterial survival during immune surveillance [77], little is known about their role in regulating biofilm structure.

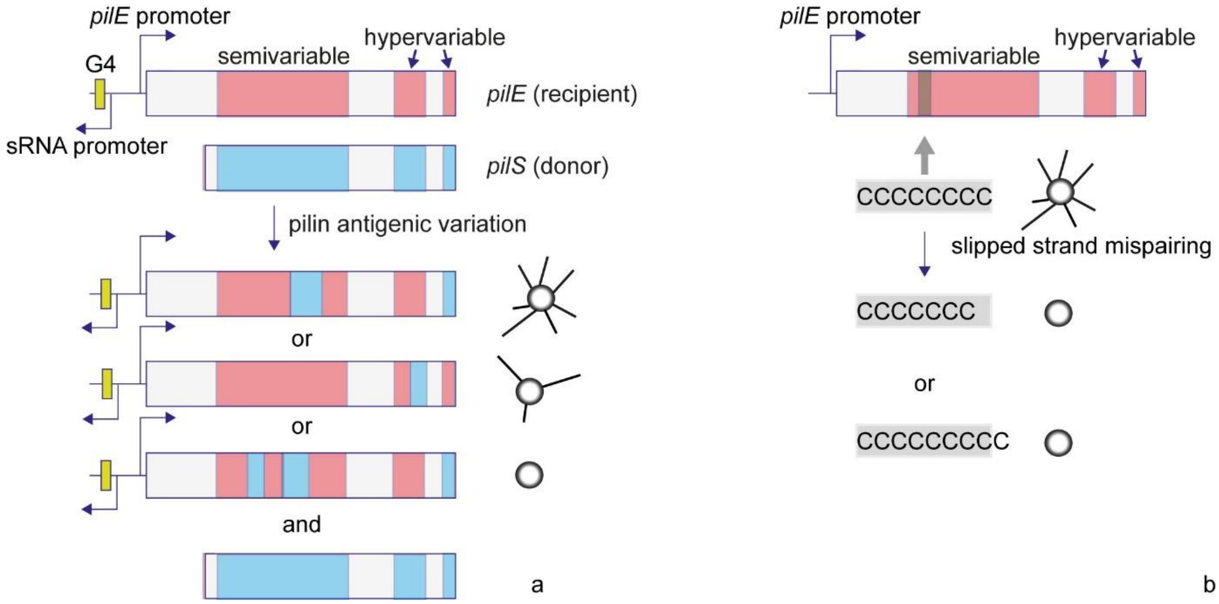

Figure 9: Pilin antigenic and phase variation. a) Antigenic variation. The gene encoding for the major pilin subunit *pilE* contains semi- and hypervariable regions. Silent, promoter-less copies of the pilin, *pilS*, containing different sequences can partially recombine into the *pilE* recipient. This process depends on the G4 motif and *recA*. The pilin sequence of the resulting variant is modified and often non-functional, generating non-piliated variants [82]. b) Phase variation due to homopolymeric repeats. Various genes involved in T4P biogenesis and post-translational modification contain homopolymeric stretches within their ORFs. Through slipped-strand mispairing during replication, the homopolymeric stretch is extended or truncated by a nucleotide at high probability and the gene is switched off. Adapted from [79].

3.3.2 Pilin post translational modifications

In addition to *pilE,* phase variations often target genes that are related to post-translational modifications (PTM) of gonococcal T4P [80]. Recently, it was demonstrated that PTM change the strength of intercellular interaction [13]. Specifically, *N. gonorrhoeae's* major pilin PilE is O-glycosylated at S63 and carries a phosphoform-modification at S68 [83][84]. Naturally, PilE bears a di-N-acetylbacillosamine sugar (diNAcBac) generated by O-linked protein glycosylation (*pgl*) pathway [85]. The *pglA* gene within the glycosylation pathway encodes for a glycosyltransferase that adds a galactose onto the basal diNAcBac which is connected to a lipid-linked monosaccharide precurser [85]. Subsequently, PglE acts as a glycosyltransferase that adds a second galactose to generate a diNAcBac-Gal-Gal trisaccharide [85]. Next, the flippase PglF is involved in membrane translocation (flipping) of the lipid-attached carbohydrate. Finally, the oligosaccharyltransferase PglO transfers the glycan to the pilin [85]. As above-mentioned, *N. gonorrhoeae's* PilE carries phosphoethanolamine or phosphocholine modifications at S68 [84]. The phosphotransferase PptA is required for this post-translational modification [86].

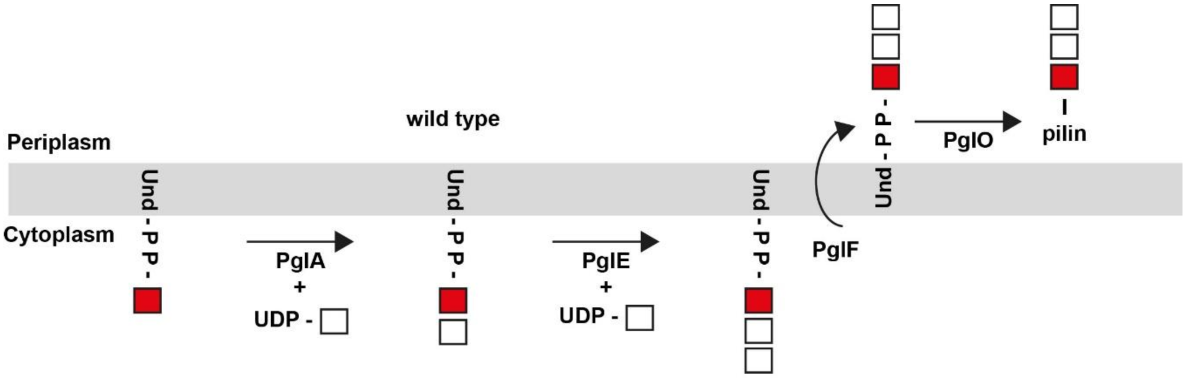

Figure 10: Current model of the pilin post-translational glycosylation pathway *N. gonorrhoeae*. Red square: Bacillosamine; White square: Hexose; UDP: Uridine diphosphate; Und-PP: Undecaprenyl-pyrophosphate. Adapted from [87].

3.4 COLLECTIVE BEHAVIOR IN CELLULAR COMMUNITIES: BIOFILMS AND SPATIAL ORGANIZATION

In the previous section it was demonstrated that bacteria, specifically *N. gonorrhoeae,* has evolved mechanisms to continuously manipulate T4P-mediated interactions. Within cellular communities, such interactions are key to determining collective behavior. It is challenging to find fundamental principles that govern the spatial organization of cell communities [88]. In this chapter, structured bacterial communities termed biofilms will be introduced. Particular focus will be set on cell-sorting, which refers to the rearrangement of mixed cell-types into homogeneous clusters [89][13]. Cell sorting will be explained on the basis of the differential adhesion and the differential strength of adhesion hypothesis (DAH and DSAH).

3.4.1 Definition and relevance of biofilms

Biofilms are multicellular microbial communities living in an extracellular matrix consisting of exopolysaccharides (EPS) and extracellular DNA (eDNA), protein fibres (including pili), and membranes [90][91][92]. This broad definition covers biofilms of most species, each producing a large variety of different matrix components. Typical biofilms are associated with specific architectures and often with high resistance levels against mechanical stresses or antibiotics. Such traits enable microbes for example to stick to surfaces or withstand (chemical) cleaning procedures. In a medical context, increased antibiotic resistance within biofilms is an ongoing challenge for treatment of bacterial infections [93]. Furthermore, cells show different phenotypic behavior in biofilm communities, such as altered growth and gene expression [94][95][96]. Together, these factors led to biofilms being a major focus of fundamental research.

Biofilm formation has several stages: At first, planktonic cells adhere to a surface or a host cell. Subsequently, the cells aggregate and form microcolonies. The biofilm grows and cells produce extracellular matrix. In the last stage the biofilm matures and single cells disperse from it, which in turn are the starting point of new biofilm formation [97].

P. aeruginosa is an opportunistic pathogen, which is specifically known for its ability to form resilient biofilms in clinical environments. *P. aeruginosa* has flagella and uses T4P to initiate surface attachment and surface sensing. Interestingly, pilus assembly proteins contribute to the ability to regulate motility and biofilm formation [98]. Subsequent to surface attachment, *P. aeruginosa* downregulates its flagellar machinery and produces exopolysaccharides which enables biofilm formation [27]. The secreted matrix structure was discovered to be able to obstruct liquid flow and affects population dynamics in the presence of hydrodynamic shear stress [99].

E. coli biofilms are initiated when swimming cells adhere to a surface. Adherence to surfaces is associated with Type 1 Pili (T1P). Subsequent to attachment, cells divide, produce and secrete adhesins that can facilitate infection. In mature biofilms cells secrete exopolysaccharides that are essential structural part of the biofilm matrix [100]. Recently, it was discovered that an amyloid fibre network of curli-polymers is able to shield *E. coli* biofilms against phage attacks. This protection is achieved by physically blocking phage transport into the biofilm via a tight network of curli fibres [101]. This example underscores the role of microbial biofilm formation as an important mechanism for protection against pathogens.

The utilized model system *N. gonorrhoeae* and its relative *Neisseria meningitidis* uses type 4 pili (T4P) to generate biofilms. As both strains are pathogens that form biofilms, they pose an enormous challenge in a medical context. In contrast to many other species gonococci have pili but no flagella. This makes them an excellent minimal model system for investigating the effect of T4P on structure and dynamical formation of biofilms. Gonococcal biofilms are formed in liquid environment, on surfaces and host cells [90]. It was demonstrated that T4P are crucial for auto-aggregation and biofilm initiation [102]. During biofilm formation and maturation gonococci use their T4P to create matrix-like structures in between aggregating cells [90]. Furthermore pili influence collective and infective behavior of aggregated cells and thus early biofilms [103]. Notably, pilus-mediated formation and dynamics of early gonococcal biofilms was studied *in vivo* and *in silico* [104][105]. It was shown that dynamical biofilms show cell sorting and promote spreading of resistant genes [13][106]. Recently it was found, that T4P-mediated interaction facilitates dynamical ordering and allows efficient adaptive colonialization [12].

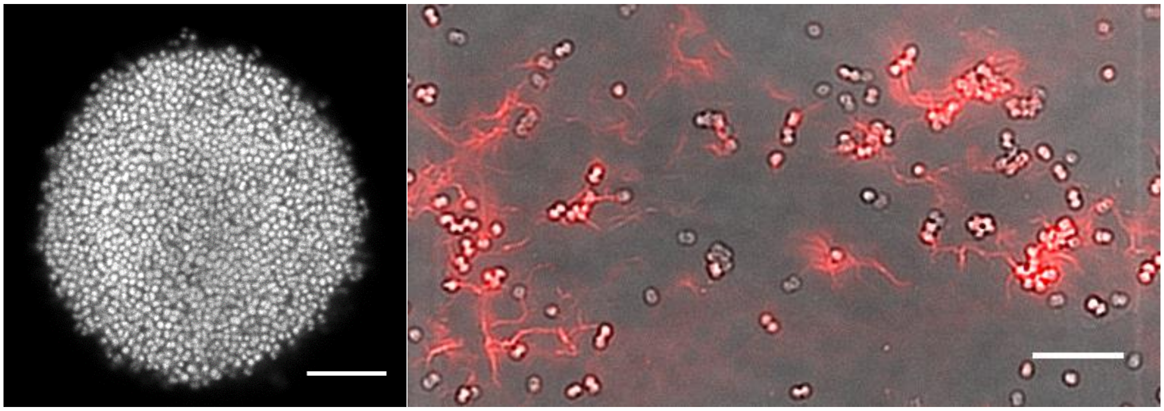

Figure 11: T4P-matrix and biofilm formation. Left: Confocal section of an early gonococcal biofilm after 4h with single cell resolution. These early biofilms are formed by T4P mediated cell-cell interactions. The image was acquired by Anton Welker. Right: Fluorescently labeled T4P form matrix-like structures between fixed cells (red). On larger timescales these structures promote auto-aggregation and initiate biofilm formation. Scale bars: 10 µm.

3.4.2 Collective spatial organization: Differential adhesion and differential strength of adhesion hypothesis

In the previous paragraph biofilms were introduced. Within such cellular communities the phenomenon of cell sorting can be observed [13]. Cell sorting refers to the rearrangement of mixed cell-types and is a general meso- and macroscopic phenomenon of cell communities.

To understand cell sorting in eukaryotic systems, the differential adhesion hypothesis (DAH) was introduced by Steinberg [107]. He proposed that tissues behave in an analogous manner to liquids. Adhesive forces between single cells lead to a certain energy (or work) that has to be overcome in order to separate them. This energy is denoted as the work of adhesion W. Like molecules in a liquid the cells within a tissue will rearrange in order to minimize the free energy. As a consequence, cells tend to form as many adhesions as possible and cell communities will assume a spherical shape. In case of two mixed cell types a and b the DAH predicts different morphotypes depending on the relations of the work of cohesion W_{aa} , W_{bb} and the work of adhesion W_{ab} . The DAH correctly predicts the outcome of sorting experiments [108]. However, it assumes that the multicellular system is in thermodynamic equilibrium. Since cells are far from equilibrium, this assumption is generally not true for biological systems.

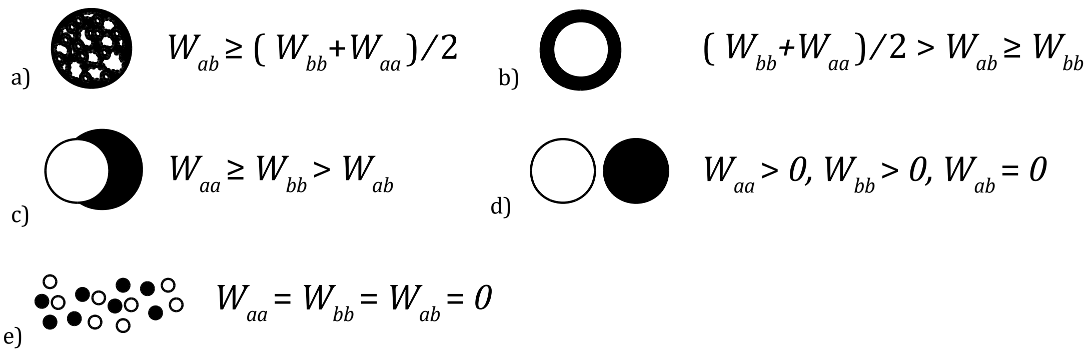

Figure 12: Morphotypes predicted by the differential adhesion hypothesis (DAH). The DAH predicts (a) perfect mixing of cells, (b) encasement, (c) partial segregation, (d) full segregation and (e) dissociation of cells. The observed morphotypes depend on the work of adhesion and cohesion between a-cells (black) and b-cells (white) [107].

Shortly after the DAH was published, an alternative hypothesis, the differential strength of adhesion hypothesis (DSAH) was proposed by Harris [109]. In contrast to the DAH which assumes thermodynamic equilibrium, he proposed the cells within a tissue actively pull on each other, performing a tug-of-war and continuously apply strain on the intercellular bonds. Eventually, the weakest bonds rupture at a specific force which generate a force imbalance that pulls the cell towards the stronger bonds. In principle, the DSAH predicts the same morphotypes as the DAH but assumes an active process as mechanistic basis for cell sorting. More specifically, the DSAH uses rupture forces $F_{rupture}$ instead of the work of adhesion W.

3.5 EVOLUTIONARY DYNAMICS IN STRUCTURED ENVIRONMENTS

Cellular communities, specifically biofilms, show well-adapted properties and enable bacteria to populate challenging environments. Population dynamics are determined by the evolutionary factors recombination, selection, mutation and genetic drift [110]. Microbial evolution is the highly complex interplay between these factors. In the following evolutionary factors and range expansion assays are introduced.

3.5.1 Population dynamics: Selection, mutation and genetic drift

Populations are described by size N and a growth law that defines their fitness f [111]. The Malthusian fitness f_i is defined by $dN_i/dt = f_i N_i$. N_i describes the size and f_i the fitness of the i-th population. The total population size N is given by $N = \sum_i N_i$ and $x_i = N_i/N$ is the fraction of the population with fitness f_i. In the absence of mutations and genetic drift the replicator equation

$$\frac{dx_i}{dt} = x_i(f_i - \bar{f}) \tag{9}$$

describes the dynamics of the population, where $\bar{f} = \sum_i f_i x_i$ is the average fitness. The replicator equation has the simple analytical solution $x_i(t) = x_i(0)\exp(f_i t) / \sum_j x_j(0)\exp(f_j t)$. In case of two competing populations $i \in [1,2]$ the solution simplifies further to a logistic function with a selection coefficient $s_{12} = \Delta F_{12} = f_1 - f_2$ [111]. Depending on the sign of s_{12} the fractions converge to 1 or 0. This summarizes the nature of selection: Differences in the rate of reproduction ensure survival of the fittest and extinction of the competitor (Figure 13).

Mutations are random changes in the genome that occur stochastically within a population [110]. Smallest possible changes are single point mutations, i.e. changes of single base pairs. The rate at which point mutations occur per generation per base-pair is commonly named mutation rate μ. Consider two sequences i and j that differ by point mutations. The hamming distance h_{ij} is the number of positions that differ between sequence i and j. As a consequence, the probability for a given sequence i of size L to be changed into sequence j is $p_{ij} = \mu^{h_{ij}}(1-\mu)^{L-h_{ij}}$. The probabilities p_{ij} are entries of the mutation matrix Q. The sum over each row in Q equals one: $\sum_{j=0}^{n} p_{ij} = 1$, where $n = 2^L - 1$ denotes the number of sequences. Q enables to generalize the replicator equation to the quasi species equation

$$\frac{dx_i}{dt} = \sum_j^n f_j x_j p_{ij} - x_i \bar{f} \tag{10}$$

[110]. In case of perfect replication ($\mu = 0$) the quasi species equation becomes the replicator equation describing pure selection.

Genetic drift is synonymous to demographic noise and describes fluctuations in the reproduction rate [111]. These fluctuations occur in every biological reproductive system and can be included by adding a noise term to the fundamental growth law: $dN_i/dt = f_i N_i + \eta_i$, where η_i is a Gaussian random variable with $\langle \eta_i \rangle = 0$. This formalism changes the replicator equations, which describe the population fractions, to a Langevin equation:

$$\frac{dx_i}{dt} = x_i(f_i - \bar{f}) + \eta_{x_i} \tag{11}$$

with Gaussian random variables $\eta_{x_i} = (\eta_i - \sum_j x_j \eta_j)/N$. Since the noise term scales with $1/N$ one can immediately see that genetic drift is a strong evolution-factor for small populations and bottlenecks but can be neglected for sufficiently large populations.

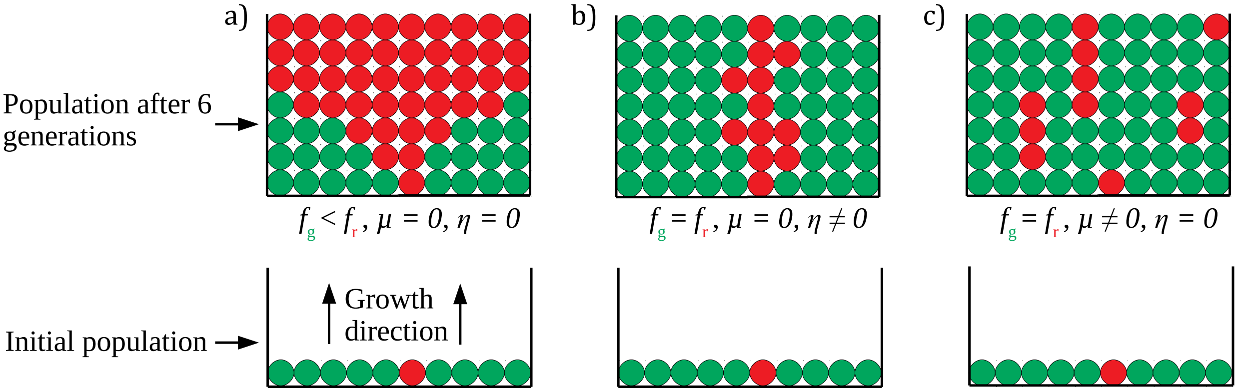

Figure 13: Evolution of a population in confined space. Three cases are distinguished: Deterministic selection without mutations (a), neutral stochastic evolution without mutations (b) and neutral deterministic evolution with mutations (c). Similar patterns can be observed within expanding populations (see section 3.5.2).

3.5.2 Expanding macroscopic biofilms on solid surfaces: Range expansions

In most cases selection, mutation and genetic drift are studied in microbial populations which are either cultured in liquid or on solid growth media. In contrast to growth in liquid environments, growth of expanding microbial populations on solid surfaces allows for spatial investigation of evolutionary factors.

Range expansions are commonly known as expanding microbial populations on solid growth media. They are created by inoculating well-mixed and fluorescently labeled populations agar. The growing macro-colonies show pattern formation that allow for drawing conclusions about cellular interactions, positioning and evolution within the population.

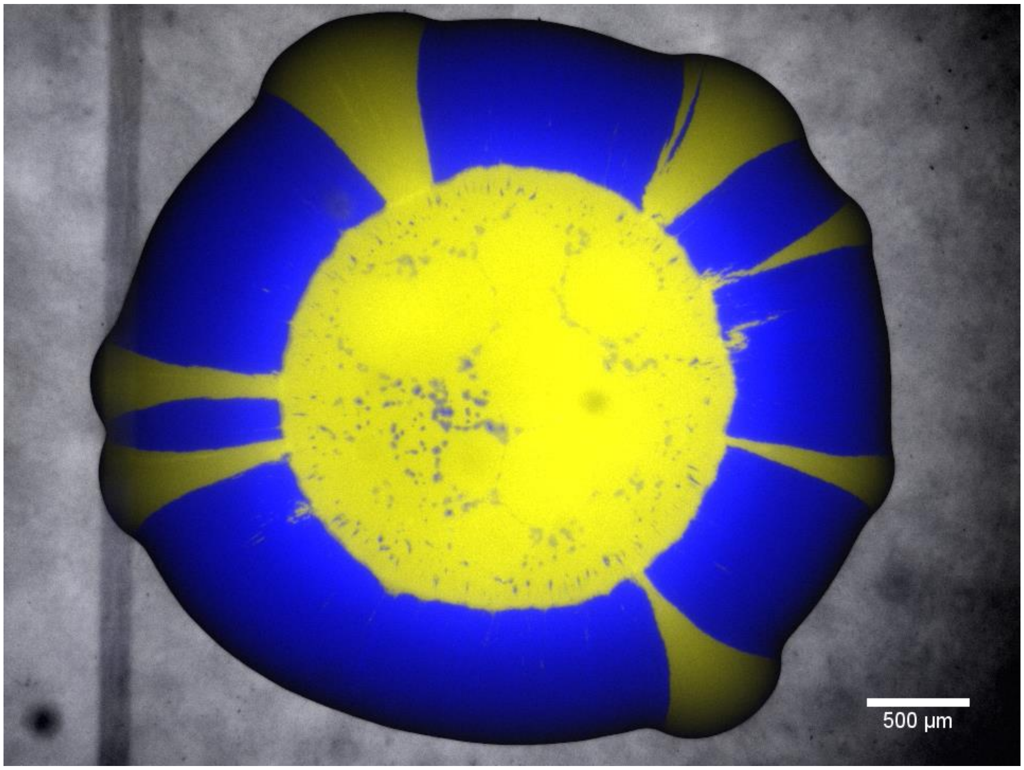

Figure 14: Macroscopic range expansion of 1:100 mixed blue and yellow cells of *N. gonorrhoeae*. Large yellow sectors form at the expanding front. The radially increasing width of the sectors indicates selective advantage of yellow cells and can be predicted by reaction-diffusion models. The initial formation of sectors within the expanding front is strongly dependent on genetic drift due to small local initial populations. Scale bar: 500 µm.

Even though bacteria were cultivated on solid agar surfaces for decades, Hallatschek et al. investigated the resulting growth patterns of expanding populations rigorously [112]. Following this work, studies implemented range expansions as a convenient tool for investigating evolution. It was demonstrated that expanding populations generically show sector-formation [112]. The initial formation of sectors was found to be driven by genetic drift that originate from a small local population sizes within expanding frontiers. This generic effect has strong consequences for the diversity in expanding large populations [112]. Moreover, it was discovered that fundamental reaction-diffusion models can predict sector formation [113]. Importantly, reports provided simple analytic expressions to calculate selection coefficients based on sector shape.

Next to investigation of evolution, range expansion were used to study responses to antibiotic treatment and allowed for investigating correlations between nutrient supply and spatial organization of microbial populations [114][115]. Recently, it was demonstrated that high-frequency mutations are found to be massively enriched in microbial range expansions when compared with well-mixed liquid cultures [116]. Furthermore, positioning was shown to have important effects on bacterial fitness in structured environments [117].

Since range expansions are realized on a timescale of days, this makes them an excellent method for simultaneous investigation of evolutionary effects and interaction-dependent spatial organization. Moreover, range expansions of biofilm-generating species are a suitable tool to investigate these effects within mature and macroscopic biofilms. In this study range expansions are utilized to characterize the effect of bacterial interaction forces on positioning and fitness of macroscopic biofilms.

3.6 AIMS

Biofilms, their formation, structure and dynamical behavior are of special interest for several fields of research. In a medical context, biofilms pose an enormous problem because they are involved in infection and associated with resistance evolution [118][119]. From a biological point of view biofilms are of special interest because they are hotspots for horizontal gene transfer, affect change cellular growth and alter transcription [94][95][96]. From a physics point of view, collective physical traits of cell-aggregates and dynamical biofilms are of particular interest. These traits are fundamentally linked to physical properties of interaction on the single cell level. However, generic effects emerging from the connection between collective behavior and cellular interactions remain unclear.

The evolution and biophysical aspects of biofilms have been focused on by recent studies. It was shown that biofilms can be composed of various species and morphotypes that can interact synergistically [120][121]. Subpopulations within microbial communities may compete with each other [122]. Importantly, it was demonstrated that spatial structure and positioning within microbial communities affect genetic drift and fitness [112][117]. Most of the evolutionary studies target ecological aspects and population dynamics, leaving the question to what extend physical interactions between single cells affect evolution of biofilms. In particular, the link between cell-cell interaction forces, biofilm architecture and fitness remains poorly understood.

In the first part of this work, an assay that allows quantifying cellular interactions at the level of single molecules was developed. To this end, a dual laser trap was established as a method for analyzing T4P-mediated attachment and detachment kinetics. Furthermore, this setup allows for measuring intercellular forces generated by T4P retraction. In collaboration with Anton Welker and Tom Cronenberg, these molecular interactions were correlated with the structure and dynamics of gonococcal colonies.

Using the newly established setup, we found that gonococcal T4P retract in the absence of the retraction ATPase PilT. Kinetics and force generation in strains lacking *pilT* were characterized.

In the next step, we addressed the question how changes in cell-cell interaction forces affect bacterial fitness in expanding macro-colonies. To this end, competition experiments between strains engineered to have different exponential growth rates and different interaction forces were performed. Subsequently, the effect of naturally occurring phase- and antigenic variation of T4P-related genes on population dynamics of macro-colonies was investigated.

Finally, evolution of auto-aggregating cells in liquid environment was addressed and whole genome sequencing was used to link phenotypic changes that emerge from intercellular interactions to evolution.

4 MATERIALS AND METHODS

4.1 BACTERIAL STRAINS, MICROBIOLOGY AND GROWTH MEDIA

4.1.1 Media and cultivation

In this study *N. gonorrhoeae* was cultivated and used as model organism. Cells were stored in GC-Freeze in liquid nitrogen or at -80 °C. If not mentioned differently, cells were cultivated overnight at 37 °C under supply of 5% CO_2 on solid GC-agar plates. Depending on individual experimental design, experiments were done on solid GC-agar in liquid GC-medium or RAM. Isovitalex was added to sterile media.

Ingredient	mass or volume	supplier or remark
NaCl	5 g	Roth
K_2HPO_4	4 g	Roth
KH_2PO_4	1 g	Roth
Proteose Peptone No. 3	15 g	BD
Soluble Starch	0.5 g	Sigma-Aldrich
Bacto Agar	10 g	BD
Isovitalex	10 ml	Custom made
MiliQ Water	1 l	

Table 1: Ingredients of 1 l GC-agar. Isovitalex was added after the agar was autoclaved and cooled down to 55 °C.

Ingredient	mass or volume	supplier or remark
NaCl	5 g	Roth
K_2HPO_4	4 g	Roth
KH_2PO_4	1 g	Roth
Proteose Peptone No. 3	15 g	BD
Isovitalex	10 ml	Custom made
Ascorbic acid 88 mg/ml	1 ml	Depending on experiment
MiliQ Water	1 l	

Table 2: Ingredients of 1 l GC-medium. Isovitalex was added after the medium was autoclaved and cooled down to 55 °C. Ascorbic acid was added to experiments where cells were exposed to a laser beam (dual trap) in order to reduce cell damage by radicals.

Ingredient	mass or volume	supplier or remark
DMEM with Glucose 4,5 g/l	8.1 ml	Thermo Fisher
L-Glutamine 200 mM	0.1 ml	Thermo Fisher
Sodiumpyruvate 100 mM	0.8 ml	Thermo Fisher
Hepes 300 mM	1 ml	Thermo Fisher
Isovitalex	100 µl	Custom made
Ascorbic acid 88 mg/ml	100 µl	Depending on experiment

Table 3: Ingredients of 10 ml reaction assay medium (RAM). Isovitalex was added to the sterile medium. Ascorbic acid was added to experiments where cells were exposed to a laser beam in order to reduce cell damage by radicals.

Ingredient	mass or volume	supplier or remark
Milk Powder	1 g	Thermo Fisher
MiliQ Water	9 g	

Table 4: Ingredients of 9 ml storage medium GC-freeze. Isovitalex was added to the sterile medium. Ascorbic acid was added to experiments where cells were exposed to a laser beam (dual trap) in order to reduce cell damage by radicals.

4.1.2 Microbiological methods

4.1.2.1 DNA-Isolation

Cells were defrosted, grown overnight and diluted in GC-medium to an OD of ~1.0. Chromosomal DNA was isolated with the Dneasy Blood and Tissue kit (Qiagen, Hilden, Germany). After execution of the provided protocol DNA concentration was measured and the solution was stored at -20 °C.

4.1.2.2 Spot transformation

For this study, the “spot transformation” was the main method used for generating new strains with the required genotype. This transformation assay is based on the fact that *N. gonorrhoeae* is a naturally competent species [123]. In principle, spot transformation works with all competent bacterial species, i.e. with cells that can take up extracellular DNA and integrate it into their chromosome via homologous recombination. In the first step cells with the desired genetic background were defrosted and incubated overnight. These cells were taken and co-incubated with specific DNA in one spot on an agar plate. This DNA carries the relevant genes and corresponding selective markers, typically antibiotic resistance cassettes.

After 24 h of co-incubation, the spot of grown cells was picked diluted. Dilutions were spread on antibiotic plates in order to grow single colonies that have acquired the relevant genes and the corresponding resistances. In the end clonal colonies of cells that have the desired genetic background and the newly acquired genes could be picked, frozen and used in further experiments.

4.1.2.3 Creation of pilT-paralog deletion strains

Three knockout strains were generated: *ΔpilT ΔpilT2, ΔpilT ΔpilU* and *ΔpilT ΔpilT2 ΔpilU. ΔpilT2* is associated with a kanamycin-resistance cassette (kanR) and *ΔpilU* is associated with an erythromycin-resistance (ermC). First, genomic DNA was isolated of existing strains that carried deletions of *pilT2* (Ng085 [124]) or *pilU* (Ng085 [124]), respectively. Subsequently, the *ΔG4* strain was transformed with chromosomal DNA isolated from the *pilT2* or *pilU* deletion strains, respectively, resulting in the intermediate strains *ΔG4 ΔpilT2*, *ΔG4 ΔpilU* and *ΔG4 ΔpilT2 ΔpilU*. Subsequently, all three intermediate strains were transformed with chromosomal DNA from the *ΔpilT* strain and selected by the associated chloramphenicol-resistance (cmR).

4.1.2.4 Creation of strains with different pilE expression levels

pilE$_{ind}$ and *3xpilE* were created in order to tune the periplasmatic PilE-concentration. *3xpilE* carries two tandemly arrayed (identical) *pilE* genes expressed ectopically in addition to the *pilE* gene in the native locus [13]. It was constructed essentially as described for strain GE21 [125] with the exception that it carries two gene copies in addition to the native copy resulting in a strain expressing three identical *pilE* genes. This strain was generated by transforming strain Ng150 [126] with genomic DNA from strain Ng109 [125]. In this strain, additionally *pilT* was deleted by transforming the resulting strain with genomic DNA from Ng178 [126].

pilE$_{ind}$ has its native *pilE* promoter replaced by an IPTG-inducible promoter. This strain was generated by transforming strain Ng150 [126] with genomic DNA from strain Ng007 [127]. The strain carrying the inducible promoter has a significantly lowered expression-level

[126]. In this strain, additionally *pilT* was deleted by transforming the resulting strain with genomic DNA from Ng178 [126].

4.1.2.5 Creation of different resistance levels (ermC±)

Two strains with different resistance levels against erythromycin were created: The first strain *red ermC*+, carries an *mcherry* gene under control of the strong *pilE* promoter. A neighboring *ermC* gene is controlled by its own *ermC* promotor and confers erythromycin resistance. The second strain *green*^{Q} *ermC*-, carries a *gfpmut3* gene under control of the strong *pilE* promoter. Again a neighboring *ermC* gene is controlled by its own promotor and confers erythromycin resistance. Both strains are resistant against erythromycin but have different resistance levels: The resistance cassette of the *green*^{Q} *ermC*- is expressed only by the *ermC* promotor, whereas the resistance cassette of the *red ermC*+ is expressed by the *ermC* and the strong *pilE* promoter. In addition to that, *green*^{Q} *ermC*- lacks the gene encoding the outer membrane pore PilQ [79].

4.1.2.6 Sequencing

Whole genome sequencing

Whole genome sequencing was done on entire populations that were frozen previously. Cells were defrosted and grown overnight. Subsequently chromosomal DNA was isolated. The isolated DNA was send to GATC (Konstanz, Germany) for whole genome sequencing. Sequencing was done on an Illumina HiSeq machine with a 100-fold coverage and a reading length of 125 bp. The raw data sets (forward and backward reads) were provided as downloadable file in the format of fastq.bz2. Data processing was done following a previously established protocol that was created by Jeffrey Power [128].

Spatially resolved sequencing of pilE

For sequencing, bacteria were picked from the outgrowth and the inoculation zone of macrocolonies and subsequently inoculated onto an agar plate. After growing the cells overnight single colonies were picked and used for *pilE* amplification via PCR. For sequencing of *pilE*, PILRBS (Sequence at ribosome-binding site of *pilE*) and SP3A (sequence in 3′ conserved untranslated region of all pil loci) primers were used [129][130]. The amplified PCR-product was send to GATC (Konstanz, Germany) for sequencing.

4.1.2.7 Immunofluorescence

For immunofluorescence assays we followed a previously described protocol [79]. Bacteria were diluted in PBS and fixed on coverslips with 4% Para-Formaldehyde (PFA). The samples were blocked with PBS (0.5% BSA) and subsequently incubated with antibody against PilE (1:100) in PBS (0.5% BSA). They were then incubated with TexasRed secondary antibody (1:500) in PBS (0.5% BSA) while being kept covered in the dark. In between the incubation steps the coverslips were washed carefully with PBS (0.5% BSA) and MiliQ. The samples were imaged with a 100x oil immersion objective (Nikon) on an inverted microscope (Ti-E, Nikon).

4.1.3 Bacterial strains

N. gonorrhoeae strains where supplied by co-workers. If necessary gonococcal strains were created by a spot transformation, which is described in the methods. Below a detailed description of all strains, their geno- and phenotypes and their origin will be given.

wt – equivalent toVD300 [131]. MS11 was selected for Opa- resulting in VD300 [132].

***wt* red**– *wt* with a mcherry-reporter in-between *lctP* and *aspC* loci.

***wt* green** – *wt* with a *gfpmut3*-reporter in the *igA1* locus.

ΔG4 – *wt* where the G4-motif, which is essential for pilin antigenic variation (AV) was deleted.

***ΔG4* red** – *ΔG4* with a mcherry-reporter in-between *lctP* and *aspC* loci.

***ΔG4* green** – *ΔG4* with a *gfpmut3*-reporter in the *igA1* locus.

recA$_{ind}$ – equivalent to N400 [133]. *recA$_{ind}$* is incapable of pilin AV without IPTG-induction.

***recA$_{ind}$* red** – *recA$_{ind}$* with a mcherry-reporter in-between *lctP* and *aspC* loci.

***recA$_{ind}$* green** – *recA$_{ind}$* with a gfp-reporter in the *igA1* locus.

WB1 – *ΔG4* with an additional non-functional *pilT*$_{WB}$ copy under an IPTG-inducible promoter in between the *lctP*/*aspC* loci.

WB2 – *ΔG4* with an additional non-functional *pilT*$_{WB}$ copy under a *pilE* promoter in the *igA1* locus.

pglEon – *ΔG4* where the phase variable glycosyltransferase gene *pglE* is in its on-state.

ΔpptA – *ΔG4* where the phosphotransferase gene *pptA* is deleted.

ΔpilT – *ΔG4* where the T4P-retraction ATPase gene *pilT* is deleted.

ΔpilT ΔpilT2 – *ΔG4* where the T4P-retraction ATPase gene *pilT* and its paralogue *pilT2* are deleted.

ΔpilT ΔpilU – *ΔG4* where the T4P-retraction ATPase gene *pilT* and its paralogue *pilU* are deleted.

ΔpilT ΔpilT2 ΔpilU – *ΔG4* where the T4P-retraction ATPase gene *pilT* and its paralogues *pilU* and *pilT2* are deleted.

green^{Q} ***ermC-*** – *recA*$_{ind}$ where the outer membrane pore gene *pilQ* was deleted. An erythromycin-cassette *ermC* and a *gfpmut3*-reporter were inserted into the *igA1*-locus. *ermC* is under the control of its proper promoter *PermC* resulting in weak resistance denoted by *ermC-.*

green ermC+ – *recA*$_{ind}$ where an erythromycin-cassette *ermC* and a *gfpmut3*-reporter were inserted into the *igA1*-locus. *ermC* is under the control of its proper promoter *PermC* and the *pilE*-promoter in front of *gfpmut3* resulting in strong resistance denoted by *ermC+.*

red ermC+ – *recA*$_{ind}$ where an erythromycin-cassette *ermC* and a *mcherry*-reporter were inserted into the *igA1*-locus. *ermC* is under the control of its proper promoter *PermC* and the *pilE*-promoter in front of *mcherry* resulting in strong resistance denoted by *ermC+.*

pilEind – *ΔG4* where the T4P-retraction ATPase gene *pilT* is deleted. Expression of the major pilus subunit PilE was regulated by an IPTG-inducible promoter that has lower expression levels that the native promoter *PpilE* [125].

3xpilE – *ΔG4* where the T4P-retraction ATPase gene *pilT* is deleted. Two additional copies of *pilE* were inserted into the *igA1*-locus leading to high levels of PilE-expression [13].

Data base reference	Name / Strain	Back-ground	Genotype / Description	Refer-ence
Ng002	*wt*	-	VD300 Opa- selected	[131]
Ng106	*wt red*	-	*wt lctP:PpilE mcherry aadA:aspC*	[79]
Ng165	*wt green*	-	*wt igA1::PpilE gfpmut3 ermC*	[79]
Ng150	*ΔG4*	*wt*	*wt G4::apraR*	[126]
Ng170	*ΔG4 red*	*wt*	*ΔG4 lctP:PpilE mcherry aadA:aspC*	[79]
Ng151	*ΔG4 green*	*wt*	*ΔG4 igA1::PpilE gfpmut3 ermC*	[79]
Ng003	$recA_{ind}$	*wt*	*wt recA6ind(tetM)*	[134]
Ng168	$recA_{ind}$ *red*	*wt*	*recAind lctP:PpilE mcherry aadA:aspC*	[79]
Ng167	$recA_{ind}$ *green*	*wt*	*recAind igA1::PpilE gfpmut3 ermC*	[79]
Ng171	*WB1*	*ΔG4*	*ΔG4 lctp:PlacP pilTWB ermC:aspC*	[126]
Ng176	*WB2*	*ΔG4*	*ΔG4 igA1::PpilE pilTWB ermC*	[126]
Ng157	*pglEon*	*ΔG4*	*ΔG4 green pglEon kanR*	[87]
Ng142	*ΔpptA*	*ΔG4*	*ΔG4 green ppta::kanR*	[87]
Ng178	*ΔpilT*	*ΔG4*	*ΔG4 pilT::m-Tn3cm*	[126]
Ng184	*ΔpilT ΔpilT2*	*ΔG4*	*ΔG4 ΔpilT pilT2::kanR*	This study
Ng185	*ΔpilT ΔpilU*	*ΔG4*	*ΔG4 ΔpilT pilU::ermC*	This study
Ng186	*ΔpilT ΔpilT2 ΔpilU*	*ΔG4*	*ΔG4 ΔpilT ΔpilT2 ΔpilU*	This study
Ng118	$green^{Q}$ *ermC-*	$recA_{ind}$	*recAind pilQ::m-Tn3cm igA1::PpilE gfpmut3 ermC*	[13]
Ng117	*green ermC+*	$recA_{ind}$	*recAind igA1::PpilE gfpmut3 ermC*	[79][106]
Ng065	*red ermC+*	$recA_{ind}$	*recAind igA1::PpilE mcherry ermC*	[79]
Ng188	*3xpilE*	*ΔpilT*	*ΔpilT igA1::pilE pilE ermC*	This study
Ng189	*pilEind*	*ΔpilT*	*ΔpilT ptac-pilE pilE:ind (tetM)*	This study

Table 5: List of strains that were used in this study.

4.2 OPTICAL TWEEZERS

In this work, optical tweezers were the main tool for characterizing single cell interactions. To this end, two steerable laser traps were generated by means of an acousto-optic deflector (AOD). Separate trapping of single cells allowed monitoring of interactions on the single cell scale.

4.2.1 Setup

The basis of any optical tweezer setup is a microscope. For this work the optical tweezer setup was integrated in an inverted confocal microscope (Eclipse TE2000-E C1, Nikon, Japan). Previous to this work a single steerable optical trap has been designed and implemented by Dirk Opitz [135].

The optical trapping is done with a 1064 nm Nd:YVO_4 laser (J20I-BL-106C, Newport Spectra Physics, Darmstadt, Germany). A switch was used to control a shutter in front of the laser head. For control of the laser intensity a combination of a rotary $\lambda/2$-plate P1 (G362-503-247, Qioptiq Photonics, Munich, Germany) and a polarizing beam splitter was used (G335-723-000, Qioptiq Photonics, Munich, Germany). In front of the $\lambda/2$-plate P1 the laser beam was expanded by two lenses L1 and L2 (-10 mm and 80 mm) (G052-303-329 and G063-046-329, Qioptiq Photonics, Munich, Germany). Behind the polarizing beam splitter P2 the laser was directed into a controllable two axis acousto-optic deflector (AOD) (DTD-274HD6 Collinear Deflector, IntraAction Corp., Bellwood, IL, USA). Behind the AOD all diffraction orders are directed through a telescope L3 and L4 (125 mm and 125 mm) (LB1904-B, BK7 B coating, Thorlabs, Dachau, Germany) and into a second beam expansion L5 and L6 (60 mm and 175 mm) (LA1134-B, BK7 B coating and LA1229-B, BK7 B coating, Thorlabs, Dachau, Germany) via two mirrors M1 and M2. In between L5 and L6 the (1,1)-diffraction order is selected by an aperture A1. The beam is then directed to the 60x objective (Plan Apochromate VC 60× water immersion, N.A. 1.20, W.D. 0.27 mm, Nikon, Japan) via a dicroic mirror. For bright field imaging the sample was illuminated by a halogen lamp. For fluorescence imaging an Intensilight light source (Intensilight, Nikon, Japan) was used. Image acquisition was done with a CCD camera (Sensicam qe, PCO, Kelheim, Germany). The motorized stage, height of the objective and dicroic filter D1 were controlled by the computer during experiments.

The QPD (Hamamatsu S6695-01) in the back focal plane was not used primarily in this study, since it could not be synchronized with the synthesizer that controls the piezo elements in the AOD. The scanning confocal unit consisting of scan head, detector, confocal laser and transmission detector was used for control experiments in this work.

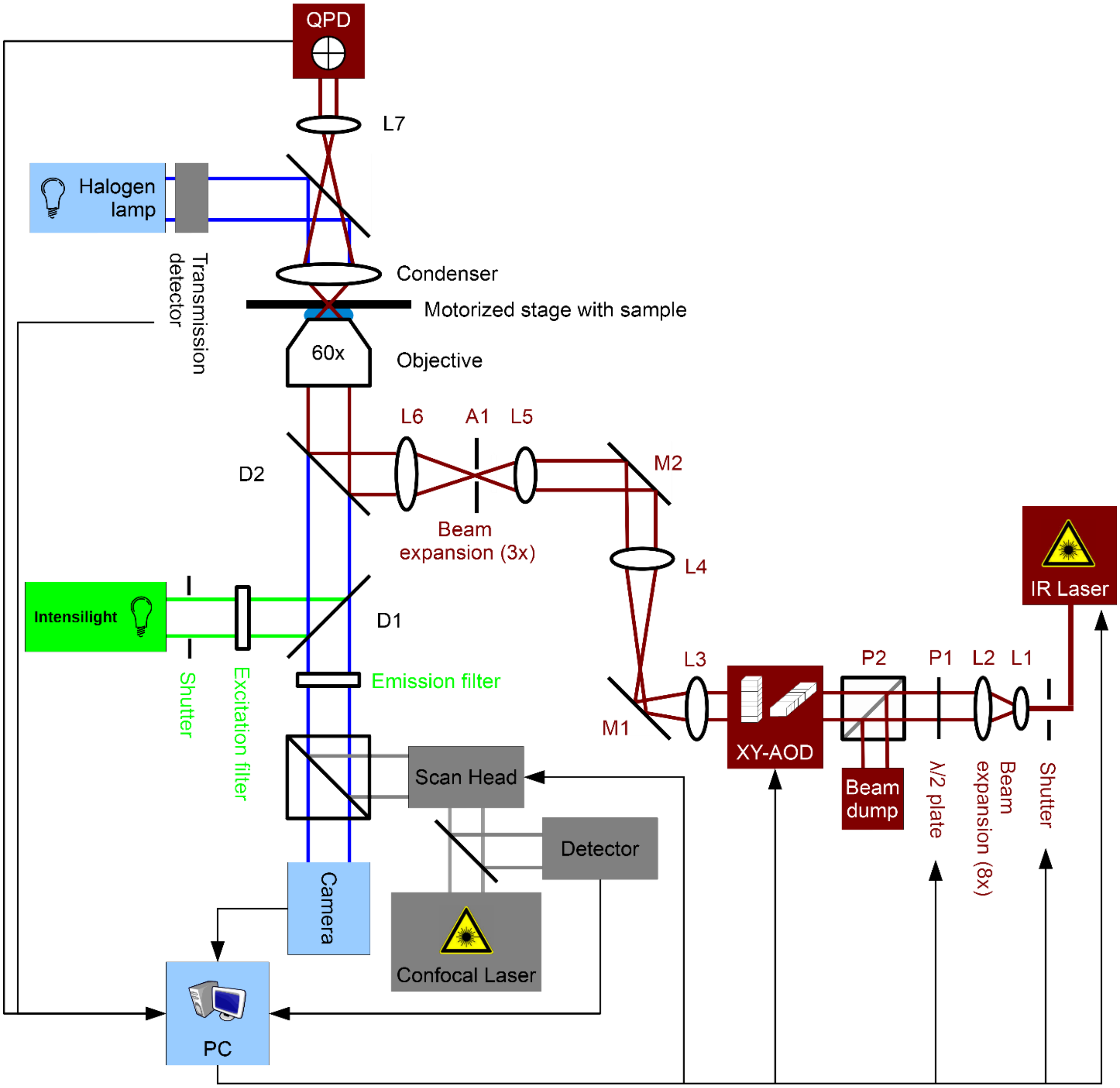

Figure 15: Setup with dual laser tweezers described in detail in section 4.2.1. Red color: Components of optical tweezers. Blue color: Brightfield microscopy components and computer. Green color: Epi-fluorescence components. Grey color: Components of fluorescence/brightfield confocal microscopy.

4.2.2 Control of the microscope and acquisition

Previously, the setup was mainly controlled by LabView programs. This was done primarily because the aim was to use several features of the setup, such as high temporal resolution (QPD), moving trap position (AOD) and brightfield acquisition (CCD-Camera) at the same time. However, it became clear that this global control had drawbacks for a dual optical tweezers setup. First, the QPD could not be used for position detection, since it was installed in the back focal plane and its high temporal resolution was not useful, because it acquired the indistinguishable information of the scattered laser of both traps. Second, the aim was to create two stable traps next to each other, therefore it was not necessary to move the position of the two traps in the x-y-plane. Third, by using LabView, frame rates of the CCD-Camera were rather slow when compared to manufacturers' instructions.

Hence, the decision was made to use micro manager (MM) [136]. This open source program is based on ImageJ [137] and offered control of microscope and camera. Also it allowed programming of sequences and shortcuts that improved image acquisition during experiments. Image acquisition could be done at maximum frame rate. Micro manager was configured with the build in plugin "configuration wizard". All important components were recognized automatically and could be merged into optical configurations or channels. Switching between optical configurations allowed to switch for example between brightfield (halogen lamp on, epi shutter closed, no dichroic D2) GFP-fluorescence (halogen lamp off, epi shutter open, gfp-dichroic D2). Scripting was done in micro managers' beanshell-script panel. All in all, 3 scripts (set_roi_doubletrap.bsh, full_image.bsh, gfp-mcherry-aquisition.bsh) were written and used. They were executed by the shortcuts F12, F11 and F5. Below a short description of the scripts is given, the full scripts can be found in the appendix of this manuscript.

The script **set_roi_doubletrap.bsh** is executed by F12 and enables the user to quickly set the smallest possible region of interest (ROI) around the x-y-position of two traps. First the live acquisition of the camera is stopped and the acquisition window is closed with the commands *gui.enableLiveMode(false)* and *gui.closeAcquisitionWindow("Snap/Live Window")*. Afterwards the ROI is set to a region that covers two laser traps and has minimal size (64 x 32 pixels) in order to obtain the maximal frame rate with the command *mmc.setROI(688, 520, 64, 32)*. The command *gui.enableLiveMode(true)* starts the live mode of the smaller acquisition window.

The script **full_image.bsh** is executed by F11 and enables the user to quickly switch back to the full field of view that is acquired by the camera. Again the live acquisition of the camera is stopped and the acquisition window is closed with the commands *gui.enableLiveMode(false)* and *gui.closeAcquisitionWindow("Snap/Live Window")*. Then the ROI is set to the full field of view by the command *mmc.setROI(1, 1, 1376, 1040)*. The command *gui.enableLiveMode(true)* starts again the live mode of the full field acquisition window. In the end, the commands *IJ.setTool("multipoint")* and *IJ.makePoint(703, 525)* mark the spot of the two laser traps.

The script **gfp-mcherry-acquisition.bsh** is executed by F5 and enables the user to acquire a fluorescence image and then automatically start acquisition of images at maximum frame rate. The time in the acquisition window has to be set to 0 in order to acquire at maximum framerates. For fluorescence imaging the exposure time is changed to 100ms by *preExposure=100.0.* Optical settings are defined by the commands, *preChannel="gfp"* and *burstChannel="bf"*. Again live acquisition is stopped by *gui.enableLiveMode(false)* and *gui.closeAcquisitionWindow("Snap/Live Window")*. The fluorescence image is acquired by the command sequence *mmc.setExposure(preExposure)*, *mmc.setConfig("channel", preChannel)* and *mmc.snapImage()*. It is then saved by the command *fs.saveAsTiff(prePath)*, where *prePath* is an arbitrary path on the hard drive. For burst acquisition the channel is switched and started by *mmc.setConfig("channel", burstChannel)* and started by *gui.runAcquisition()*.

4.2.3 Control of the AOD

The acousto-optic deflector consists of two orthogonally aligned tellurium dioxide crystals. Each crystal is excited by a piezo element. The elements are controlled by a synthesizer (DVE 120 Dual Frequency Source, IntraAction Corp., Bellwood, IL, USA). A power amplifier amplifies the synthesizers' radiofrequency signal before it reaches the AOD (DPA 502D Dual RF Power Amplifier, IntraAction Corp., Bellwood, IL, USA). The synthesizer is controlled by the LabView program '*DVE control.vi*', which allows to set frequencies, parameters and operation mode (Figure 17). The synthesizer has two channels, each corresponding to one crystal and x-y-position in the focal plane, respectively. By applying a square wave signal to one of the channels (typically channel 1 which controls the x-position) the laser beam could be switched between to angles. Different angles translate to different positions in the sample plane. By switching between two angles at high frequencies, two stable optical traps could be created (Figure 16).

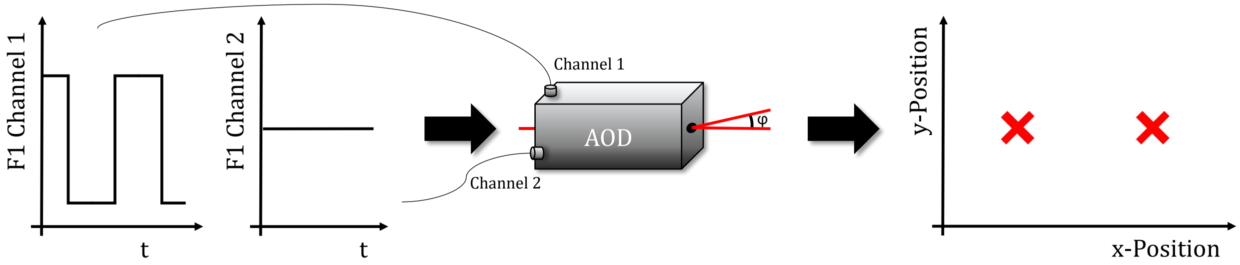

Figure 16: Illustration of AOD control. Signals of a two-channel frequency generator card are amplified and transferred to the AOD. By keeping one channel constant and one changing in a square-wave fashion the first order of the scattered beam is split resulting in two distinct trap position in the sample plane.

4.2.3.1 Synthesizer controls

Channels 1 and 2 have the same adjustable parameters and frequencies (Figure 17). Parameters, functionalities and operation modes that were necessary to create a square wave in one direction will be explained below.

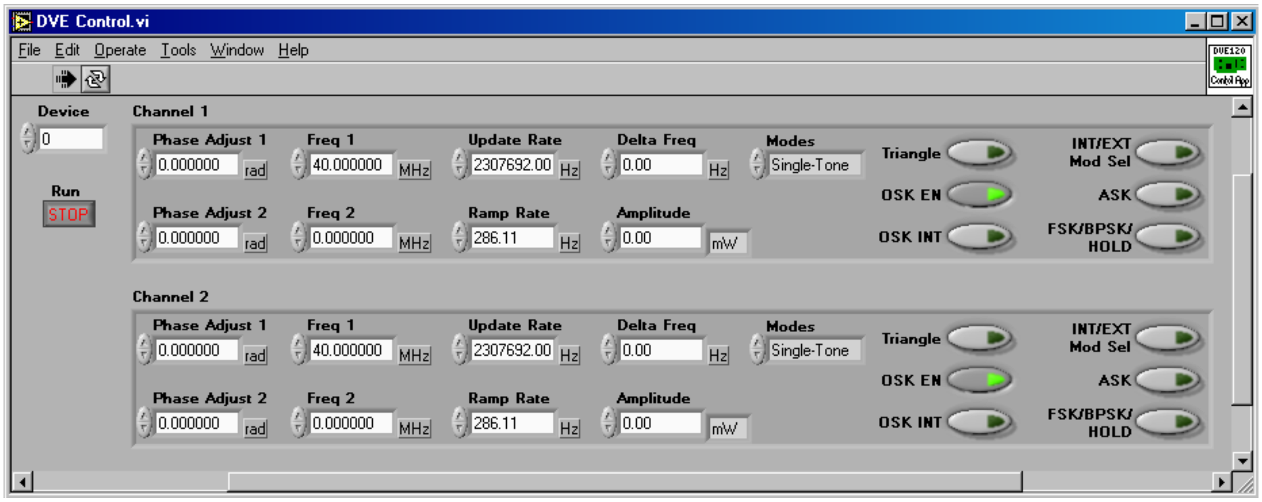

Device 0

Channel 1

Phase Adjust 1 0.000000 rad
Freq 1 40.000000 MHz
Update Rate 2307692.00 Hz
Delta Freq 0.00 Hz
Modes Single-Tone
Phase Adjust 2 0.000000 rad
Freq 2 0.000000 MHz
Ramp Rate 286.11 Hz
Amplitude 0.00 mW

Channel 2

Phase Adjust 1 0.000000 rad
Freq 1 40.000000 MHz
Update Rate 2307692.00 Hz
Delta Freq 0.00 Hz
Modes Single-Tone
Phase Adjust 2 0.000000 rad
Freq 2 0.000000 MHz
Ramp Rate 286.11 Hz
Amplitude 0.00 mW

Figure 17: LabView control panel of the frequency generator card with default settings.

The controls **Freq 1** and **Freq 2** set the Frequency Tuning Words (FTW1 and FTW2). These words set then the output frequency in units of Hz.

The **Update Rate** controls the Update Clock (UDCLK) of the synthesizer and sets the rate at which control parameters are loaded into the core of the synthesizer. Update Rates are in units of Hz.

The **Ramp Rate** controls the Ramp Rate Clock (RRCLK) and is active when the synthesizer is set to Chirp Mode. Essentially, it defines how long the synthesizer stays at a specific frequency. Ramp Rates are in units of Hz.

The control **Delta Freq** sets the Delta Tuning Word (DTW) and is active in Chirp Mode. DTW sets the frequency step size in Chirp Mode in Hz.

Amplitute controls the Output Shape Key Multipier (OSKM). This control sets the output amplitude of a channel in mW.

4.2.3.2 Operation modes

The mode **Single Tone** is the default mode. In this mode Update Rate and Delta Frequency are ignored. By defining Frequency 1 and Amplitude the user is able to apply a single frequency to the specific crystal. Typically, this mode is selected for channel 2, so that frequency and y-position of the trap stay constant.

Usually the **Chirp Mode** is designed to sweep through frequency space and is used for example in radar applications [138]. When this mode is selected Ramp Rate and Delta Frequency become relevant. By defining Frequency 1 $F1$, Delta Frequency δ and manipulating Update Rate U and Ramp Rate R the user is able to apply a frequency sweep to the specific channel (Figure 18).

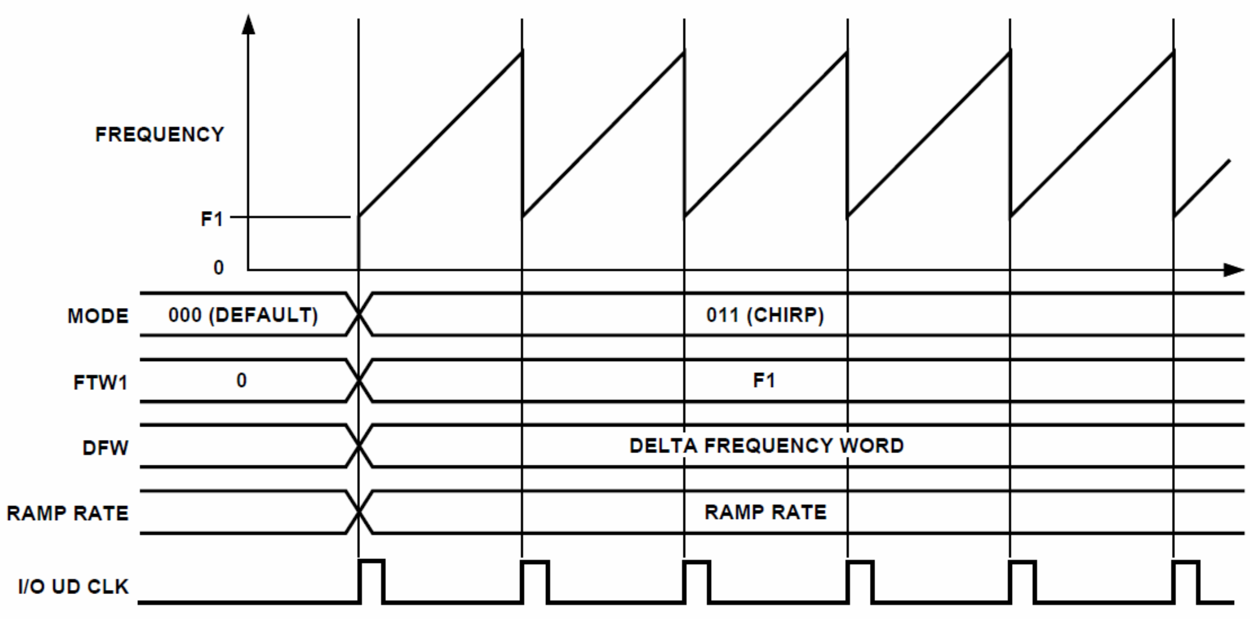

Figure 18: Classic chirp signal generated by the frequency generator card. FTW1 is set to F1. DFW and RAMP RATE define the slope of the frequency sweep. At every UDCLK signal bit the frequency sweep restarts. Adapted from [139].

4.2.3.3 *Generation of two optical traps with optional force spectroscopy*

As mentioned above, the Chirp Mode can be used to scan frequency space. In order to generate two time-shared optical tweezers, it is necessary to switch between two frequencies. In other words, it is necessary to apply a square wave signal to one channel of the AOD. It is important that the switching rate of the square wave is as fast as possible, in order to create a stable trapping potential for interacting cells. If the switching rate is too slow (~ Hz) trapped objects jump from one position to the other. In order of several kHz separate trapping of two objects is already possible, but as soon as binding events occur the two objects move synchronously between the two trap positions with frequency of the square wave. Switching rates that can be reached by manipulation of $F1$ in the Single Tone mode via LabView was in the order of kHz and therefore to slow. Furthermore, LabView is inferior to the operation system of the computer. This can cause stumbling of the LabView driver program if the operation system decides to use resources elsewhere. Problems with the operation system, LabView and slow switching rates could be avoided by using the Chirp mode of the synthesizer. The idea is that the Chirp mode is not used to sweep through frequency space by increasing $F1$ discretely in small steps of size δ but to sweep only one step up from $F1$ to $F1 + \delta$ and then start over again. This is realized by setting U and R such that $U = 2 \times R$. The synthesizer then jumps between $F1$ and $F1 + \delta$ at rate U (Figure 19).

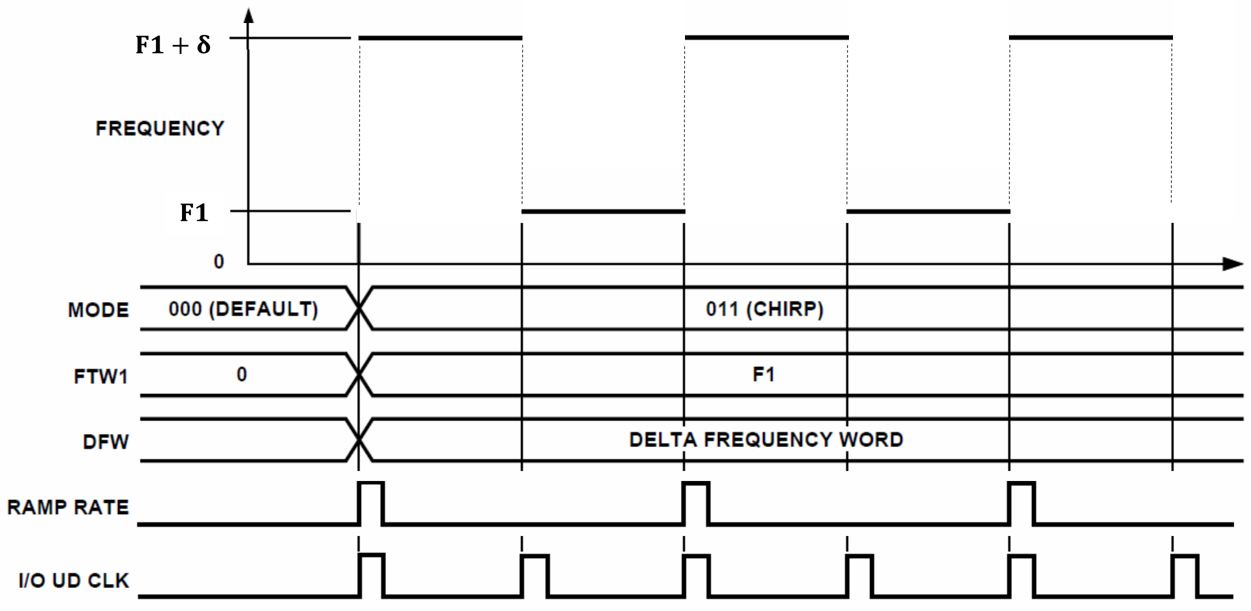

Figure 19: Modified chirp signal that creates a square wave signal. FTW1 is set to F1. DFW controls the amplitude of the wave and consequentially the trap distance in the sample plane. At every UDCLK signal bit the frequency jumps to its starting position F1. The RAMP RATE controls the jump to F1+δ and is set to half of the Update rate ensuring periodicity of the square wave.

In the course of this study it became interesting to use two optical tweezers to perform force spectroscopy measurements on bacteria that show strongly reduced pilus activity. For this it was necessary to move one of the traps in a periodic fashion to induce and rupture bonds between cells. We decided to use a triangle signal so that the loading rate that is applied to a bond is constant. The triangle signal did not necessarily have to have a high frequency in order to mimic rupture events. It is known that normal rupture events are based on gonococcal retraction speeds, which are in the order of 2 µm/s. Following up on this, movement of one optical trap over a range of 2 µm in one second should be sufficient to induce rupture events. In other words, the frequency of the triangle signal that is applied to one of the traps needed to be in the order of Hz. This was achieved by manipulation of δ via LabView: A triangle signal with adjustable amplitude and frequency was created and applied to δ. This way $F1$ (or the fixed trap position), and the speed of switching between $F1$ and $F1 + \delta$ remained constant whereas the second trap moves in a periodic fashion towards and away from the fixed trap.

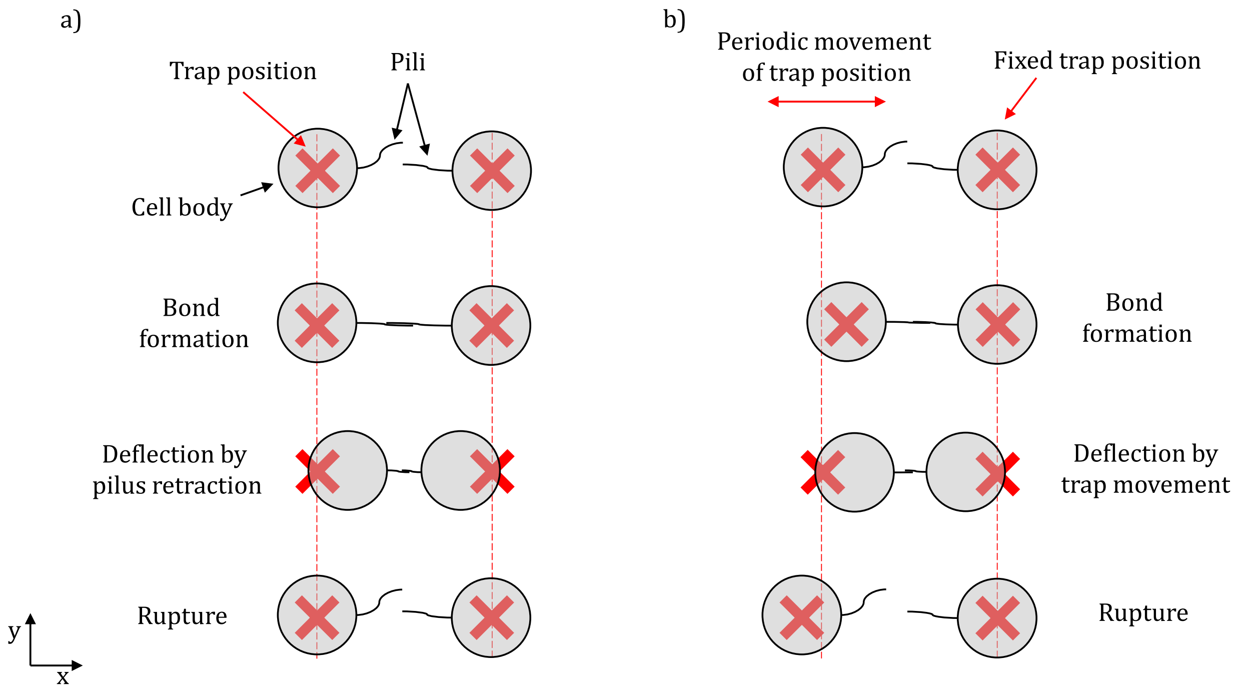

Figure 20: Demonstration of two operation modes of dual laser tweezers. a) The tweezer setup is operated in static mode. Trap positions are fixed. Deflections of cells are the result of bond formation and subsequent pilus retraction followed by a rupture event. b) The tweezer setup is operated in spectroscopy mode. One trap position is fixed, the other moves periodically in x-direction. Deflections of cells are the result of bond formation and subsequent movement of one trap position until the occurrence of a rupture event.

4.2.4 Tracking and image processing

In this study, single cell interactions were characterized by trapping monococci with spherical shape. Positions of individual trapped cells were extracted by applying the circular Hough transformation algorithm to filtered images [140]. Noise in raw images was filtered by masking with a Gaussian function in Fourier space. Subsequently a 2D digital filter was applied. Prior to the circular Hough transformation algorithm, a 2D gradient was calculated to amplify contours of the cells.

The circular Hough transformation is based on 'votes' in an accumulation matrix [141]. Every pixel characterized by coordinates (x, y) is considered and all parameters that are defined by a circle equation $(x - x_0)^2 + (y - y_0)^2 = r^2$ are scanned in arbitrary intervals. To be more specific this process is similar to a voting process. The parameters (x_0, y_0, r) describe a circle with radius r and center (x_0, y_0). All parameter combinations (each within a given range that is defined by the user) are associated to all image elements. Each element then votes for all scanned parameter combinations. These votes are added up in the accumulation matrix. The matrix has three dimensions each representing one parameter of the space (x_0, y_0, r). After the voting procedure is executed for the entire image, a 3D peak detection algorithm finds peaks in the accumulation matrix. The peaks then correspond to the most likely parameters x_p, y_p and r_p defining circles with radius r_p and center (x_p, y_p).

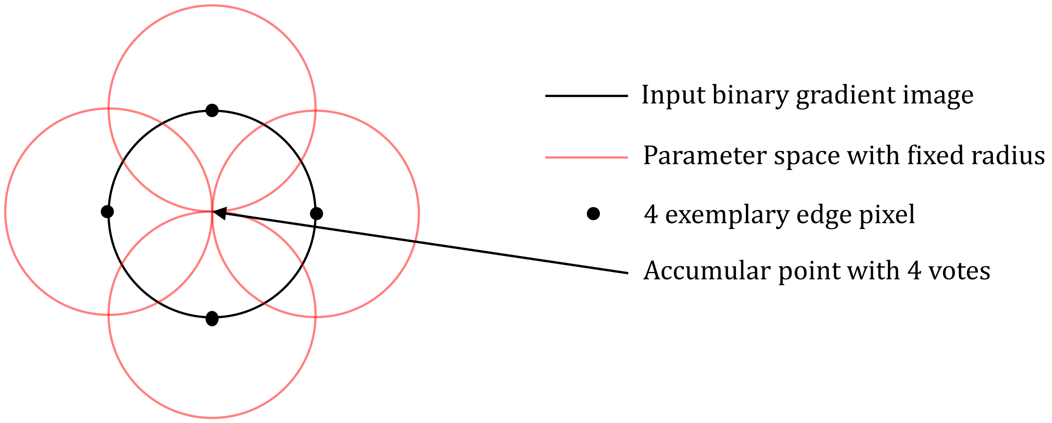

Figure 21: Demonstration of the circle detection by Hough transformation. A gradient image is loaded. For convenience it is displayed as a binary image. Parameter space (in this case position) is scanned and added up in the accumulation matrix for every edge pixel. A peak in the accumulation matrix gives the center of the circle within the loaded image.

4.2.5 Data evaluation

Raw data of bacterial interaction was acquired with a CCD camera as image stack file. In general, the images displayed two bacteria that were deflected from their equilibrium position in case of binding and retraction events. The images were analyzed with Matlab. In order to speed up the evaluation of many data sets a graphical user interface (*tracking_gui_dual_trap.m*) was written and used. In the following a sequential description of the program will be given.

1. The data path is entered and raw data consisting of an image stack file (.tif), the meta data file (.txt) and a fluorescence image file (.tif) were imported into Matlab.

Automatically, the fluorescence image was displayed and the average frame rate was calculated from the meta data.

2. Image stack files were then filtered by a band pass and a two dimensional digital filter. Subsequently a Circular Hough transformation was performed on the filtered images and the central positions of the two interacting bacteria were calculated with subpixel accuracy for every image (all time points).
3. The deflections from the equilibrium position were translated into the corresponding force and averaged over the two trapped cells. The averaging was performed at this point because the trapping potential and therefore bacterial deflections and velocities were dependent on shape and size of the cells. If two cells were not equally shaped deflections were not equal. This ‘biological noise’ was averaged out.
4. Finally, the force in pN was plotted as a function of time and examined by the user manually. All events, including rupture force [pN], reversal force [pN], retraction velocity [nm/s], elongation velocity [nm/s], retraction time [s], elongation time [s], pausing time [s] and bundling time [s] were stored in one array and saved as text file into the corresponding folder.

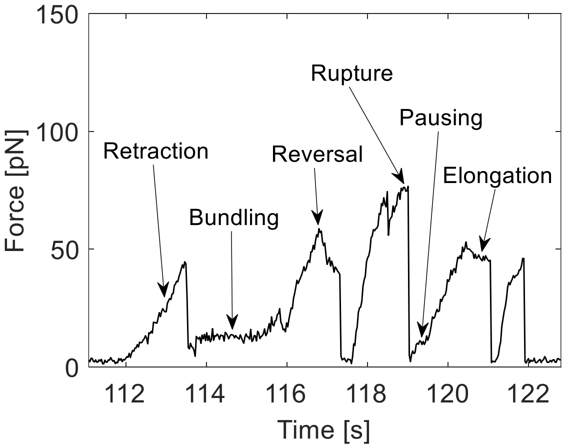

Figure 22: Manual event detection from raw data. Events include rupture force [pN], reversal force [pN], retraction velocity [nm/s], elongation velocity [nm/s], retraction time [s], elongation time [s], pausing time [s] and bundling time [s].

4.2.6 Equipartition theorem

The stiffness of optical tweezers can be calibrated by means of the equipartition theorem [68]. For this it is assumed, that the trapping potential is a harmonic potential $U(x) = kx^2/2$ with a spring constant or trap stiffness k. This potential is a function of the deflection x and leads to a linear relationship between force and deflection $F = -\nabla U = -kx$. This assumption allows to write the partition function for the optical trap as

$$Z = \frac{1}{l}\int_{-\infty}^{\infty} \exp\left(-\frac{kx^2}{2k_B T}\right) dx = \frac{1}{l}\sqrt{2\pi k_B T/k}\,, \tag{12}$$

where $1/l$ is the density of states and $k_B T$ the thermic energy. Using this, the measurable mean squared displacement

$$\langle x^2 \rangle = \frac{\frac{1}{l}\int_{-\infty}^{\infty} x^2 \exp\left(-\frac{kx^2}{2k_B T}\right) dx}{Z} = \frac{k_B T}{k} \tag{13}$$

becomes a simple expression, that depends only on k and T. This implies, that $\langle x^2 \rangle$ can be measured in order to calculate the trap stiffness

$$k = \frac{k_B T}{\langle x^2 \rangle}. \tag{14}$$

4.2.7 Drag force method

The drag force calibration method uses the force balance between hydrodynamic friction force F_R and laser induced restoring force F of a trapped micro particle moving in liquid. In general, the flow velocity around moving particle in a fluid is described by the Navier-Stokes equations [142]. The Navier-Stokes equations can be written in a non-dimensional way by introducing the Reynolds number $Re = \rho u L/\mu$ [5]. ρ is the density and L the characteristic length of the moving micro particle. μ and u are the dynamic viscosity and the velocity of the fluid. For small objects such as bacteria or beads the Reynolds number is small $Re \ll 1$, indicating laminar flow and no turbulence [143]. Assuming that $Re \ll 1$, the Navier-Stokes equations can be simplified to the Stokes equation $\nabla p = \nabla^2 u$, where p is the pressure [144]. By introducing the Stokes stream function the equation can be solved [144]. Based on the solution, it can be shown that the drag force of a moving solid micro particle with radius R is

$F_R = 6\pi\mu R u$ [37]. In practice, the fluid around the trapped cells was moved with the controllable stage of the microscope. At a constant velocity the force balance between friction force F_R and laser induced restoring force F reads

$$-F = kx = 6\pi\mu R u = F_R \,. \tag{15}$$

This equation allows to calibrate the optical trap as well as to check the linear regime of the optical trap by measuring the deflection x as a function of velocity u.

4.2.8 Linearity of the optical tweezers

The motorized stage was controlled by the program “PriorActiveX”. This program allowed to control velocity and acceleration of the stage. Since the stage is driven by electric motors and not by piezo elements the movement is abrupt and imprecise. At lower velocities (~100 µm/s) stage driving was more accurate than at higher velocities (~1000 µm/s). Therefore, this method was only used at small laser powers to check the linear regime of the trap. We observed, that the linear regime extended up to deflections of $x \approx 370$nm for monococcal cells.

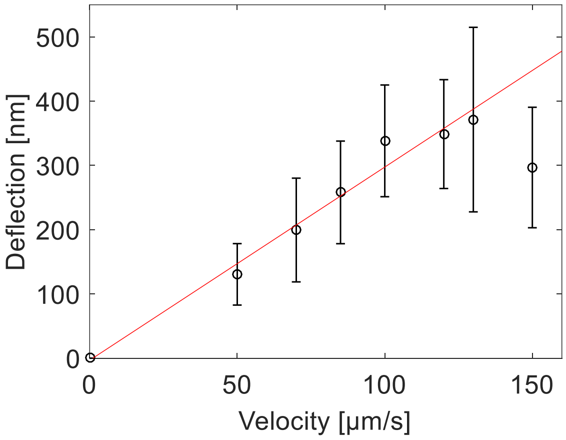

Figure 23: Characterization of the linear regime of dual laser tweezers. Deflection was measured as a function of stage velocity. A linear fit indicates linearity up to 370 nm deflection.

4.2.9 Trap stiffness

The dual laser tweezers setup used in this study was primarily calibrated by means of the equipartition theorem. This was done due to practical reasons: A power spectrum calibration was impossible, because the QPD in the back focal plane could not be triggered by the synthesizer. Therefore, the signal that was recorded on the diodes contained the superposition of the scattered laser beam of both traps and could not be decomposed into single trap signals. The drag force method was considered to be inaccurate because the movement of the stage is abrupt and imprecise. In order to calibrate the trap stiffness non piliated cells where used. A minimum of 10 bacterial pairs was recorded for at least 500 frames. Each pair was recorded at maximum laser current (18A) and 2%, 5%, 7%, 10% and 15% power. After calculation of $\langle x^2 \rangle$ the trap stiffness at 100% power was extrapolated and averaged over all calibration measurements in order to take into account the large variability of size and shape of trapped cells. Mean stiffness values of each trap were consistently in the order of k ≈ 0.1 pN/nm.

4.2.10 Spatial calibration

In order to calculate a calibration factor that links the frequency distance δ to the spatial distance of the two optical traps, two beads with a diameter of 2 µm were trapped and tracked at various values of δ. The spatial distance between the two beads was calculated and plotted as a function of δ. Trivially the spatial distance has a minimal value of 2 µm for 2 µm-sized beads. A linear fit gave a calibration factor of 1.894 ± 0.007 µm/MHz (Figure 24).

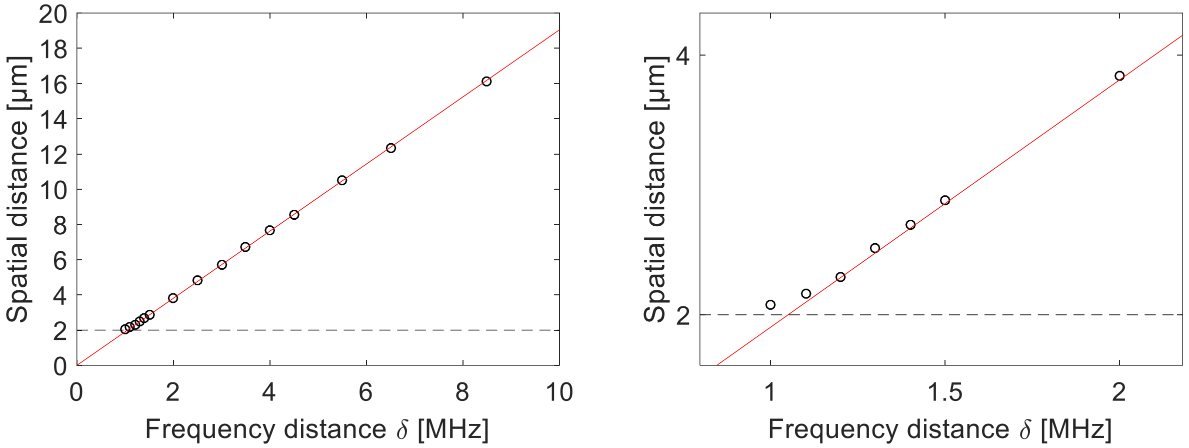

Figure 24: Spatial calibration of the dual optical tweezers. Spatial distance between two traps was measured as a function of the frequency distance delta that is applied to the frequency generator card. The right diagram displays a close up view of small distances. The dashed line indicates the sum of radii of two 2 µm-sized beads as minimal possible distance. A linear fit is shown in red.

4.2.11 Elastic effects dominate velocity distributions in the position clamp mode of the dual laser tweezers

To address the question whether the retraction velocities of interacting cells are comparable to the velocities of single T4P retraction [47][124], T4P retraction velocities were measured with the wild-type *ΔG4* in dual optical tweezers. First, a single cell (monococcus) was trapped in each trap. Binding of T4P to the opposite cell followed by a retraction event led to the deflection of both cells from their equilibrium position. The retraction velocity was calculated from the averaged tracks of both monococci. The average velocity of single T4P retraction is approximately 2000 nm/s in oxygen enriched conditions at constant feedback forces of 30 pN [52]. We calculated the force-averaged retraction velocity, which is lower by a factor of four compared to the retraction velocity under oxygen enriched conditions (Figure 25). A median retraction velocities of $v_{\Delta G4} = (541 \pm 212)$ nm/s was found. The stated error represents the median absolute deviation.

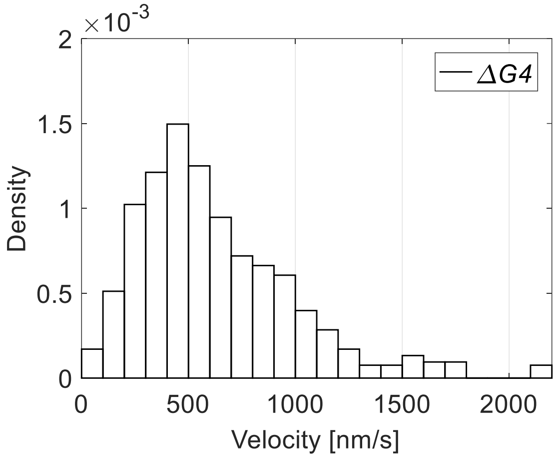

Figure 25: Retraction velocities of *ΔG4* (Ng150). Probability density of *ΔG4* force-averaged retraction velocities is shown (N=551).

There are two possible explanations for this bias. First, the data is acquired without the ability to control the forces that are applied to the cells while interacting. This means that the measurement is done at various positions in force-velocity parameter space resulting in a superposition of several velocity-regimes. Second, pili and cells themselves are to some extend elastic materials that deform under applied forces [64][145]. Hence, a portion of the force that is generated translates into elastic deformations that result in the observation of slower retraction and deformation. Notably, shape deformations of cells that were deflected from their equilibrium position could be monitored (Results: Figure 28).

4.3 EVOLUTION / WHOLE GENOME SEQUENCING (WGS)

4.3.1 Design of the evolution experiment

The major focus of this study is the investigation of intercellular interaction dynamics and their specific impact on cell aggregates and biofilms. A lot of progress has been made recently. Generally speaking, advances have been made where structure, dynamics, protection and mechanics have been investigated [126][12][101][99]. However, these advances focus primarily on shorter timescales that are in the order of a few generations. Larger timescales, where evolutionary processes become relevant for cell mechanics and their significance in multicellular systems have not been the main focus. On account of this we wanted to design an evolution experiment that fills this gap. The primary idea was to create an experimental procedure, where interacting and biofilm-forming cells grow over many generations, followed by a systematic investigation of genomic, mechanical and macroscopic parameters. For this, and specifically for *N. gonorrhoeae*, it was necessary to implement a selection step in order to avoid mutations that prevent biofilm formation and cell-cell-interactions. We decided to follow the approach of Poltak and Cooper [121], where only cells that adhere to a bead were transferred into fresh medium.

4.3.2 Experimental procedure

The evolution experiment was done in 6-well plates (Sarstedt). Prior to inoculation wells were filled with 10 ml GC-medium and Isovitalex. 3 large or small glass beads were added. After inoculation (or bead transfer) the well plates were incubated at 37 °C and 5% CO_2 for 24 h. The wells were not shaken during incubation. All in all, 6 parallel lines of *wt green* were cultivated of 17 days. 3 of these lines were treated 2 mM H_2O_2 throughout the experiment in order to apply stress that was considered to have an impact on biofilm formation [146]. Bead transfer was done with sterile polymethylpentene (PMP) tweezers (Thermo). Exclusively 1 of the 3 beads that had contact to cells for only 24 h was transferred to the next well (Figure 26). The remaining 2 beads of the same size were stored in cryo-stocks.

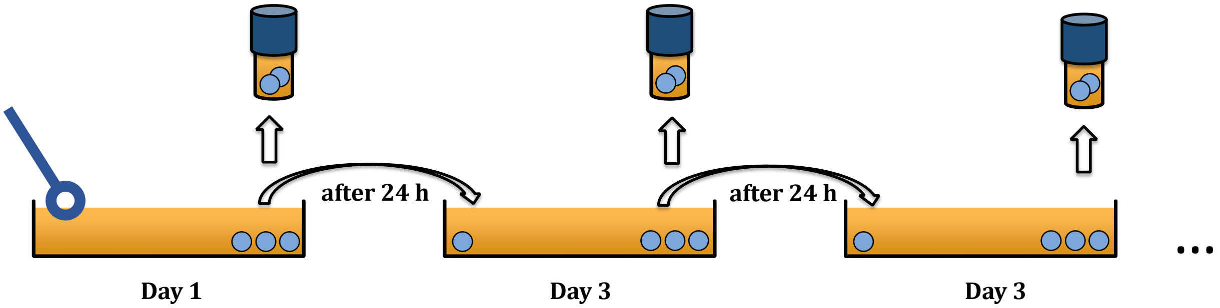

Figure 26: Experimental procedure of the evolution experiment. Inoculation is indicated by a blue inoculation loop. After 24 h of growth two beads ant attached cells were stored in cryo-tubes. Large and small beads were used to distinguish between inoculation and growth.

4.4 DETERMINATION OF GENERATION TIMES

A previously published protocol that was established by Dr. Enno Oldewurtel was used for determination of generation times [13]. Cells were cultivated overnight and 2 single colonies were re-suspended in 2 ml GC-medium. The suspension was vortexed rigorously in order to disintegrate cell aggregates. 5 µl of the suspension were placed on agar plates. The low density of single cells on agar allowed monitoring exponential growth of single colonies via time lapse fluorescence microscopy. The rate of fluorescence intensity increase was used calculate the growth rate of numerous colonies.

4.5 RANGE EXPANSIONS

A protocol to generate range expansions as model system for macroscopic biofilms, was developed by following the approach of Hallatschek et al. [112] [79]. Bacteria from overnight plates of each strain were re-suspended in GC medium to an optical density of 2.0. Suspensions of strains labelled by different fluorescent proteins were mixed and droplets of with a volume of 0.25 µl were applied to agar plates. Subsequently, the plates where incubated at 37 °C and 5% CO2. Generally, all colonies were inoculated from suspensions of 1:1 ratios. If necessary, the suspensions were mixed in ratios 1:1, 1:10, and 1:100, respectively. For selective growth, the agar contained erythromycin concentrations of 0, 2, 3, and 4 µg/ml.

5 RESULTS

The results of this study are combined in five sections.

The first section investigates bacterial cell-cell interactions by means of dual laser tweezers.

In section two, the impact of T4P motor activity and of pilin post-translational modifications on rupture forces and detachment rates was quantified and linked to mesoscopic properties of early biofilms.

Section three examines pilus retraction without active motor ATPase. Unexpectedly, we found that T4P retract in the absence of the T4P retraction ATPase PilT. Observations indicate that retraction proceeds at a speed orders of magnitudes slower than native pilus retraction and that it is independent of *pilT*-homologues. Our data suggests, that periplasmatic PilE concentrations affect the speed of retraction.

In the fourth section, single-cell interactions are linked to biofilm architecture and bacterial fitness. We investigated mutational loss of pilus-mediated interactions and connected this mechanism to bacterial positioning and population dynamics of macroscopic biofilms. Our findings indicate that on/off-switching of attractive forces is a powerful mechanism for governing population dynamics in bacterial biofilms.

The last section extends the scope of this study to the evolution of interacting, biofilm-forming bacteria. Results demonstrate that gonococci are able to create macroscopic structures and pellicles.

5.1 DUAL LASER TWEEZERS ENABLE CHARACTERIZATION OF CELL-CELL INTERACTION FORCES AND DYNAMICS

Previous studies used single optical tweezers to characterize T4P-mediated interactions [47][13]. In this study we employed dual laser tweezers to characterize cell-cell interactions of *N. gonorrhoeae*. We worked with *ΔG4* cells as background strain, because of its inability to perform pilin antigenic variation (AV) [147]. Pilin AV is able to vary the sequence of *pilE* at high rates [129][80]. It is likely that altered *pilE* sequences affect binding characteristics of type 4 pili (T4P). Consequently, we used *ΔG4* cells to prevent sequence based biases in the data.

5.1.1 Intermittent pilus-mediated interactions are inconsistent with a stochastic Poisson process

Single-cell interactions are affected by thermal noise and the stochastic nature of molecular machines. Recently, it was demonstrated that waiting times between cell-bead interaction events are not consistent to a Poisson-process [53]. In this paragraph we investigate stochastic pilus-mediated cell-cell interactions. To this end we used the dual laser tweezers setup to monitor interacting cells. Single gonococci (monococci) where trapped in two separate laser traps. By means of T4P, the cells bind to each other and deflect themselves from the central positions of the traps when the pili retract. Since the measured deflection is proportional to the restoring force, interaction forces could be measured. The monitored interactions are mediated by repeated binding, T4P retraction and detachment events [53]. For purely random events, waiting times between consecutive events are distributed exponentially. The exponential distribution is a direct consequence of a stochastic Poisson process that assumes no memory in the system [148]. In order to test whether repeated interaction is memoryless, the waiting time between rupture events that were followed predominantly by single retraction events was investigated (Figure 27). Rupture events as measure were chosen, because they appear as unambiguous signals in the data. It is important to note that the waiting time distribution between rupture events misses only very rare interactions that are combinations of retraction and elongation without rupture. These combinations occur at a vanishingly small rate. Therefore, the waiting time distribution between rupture events is representative for all measured repetitive interaction patterns.

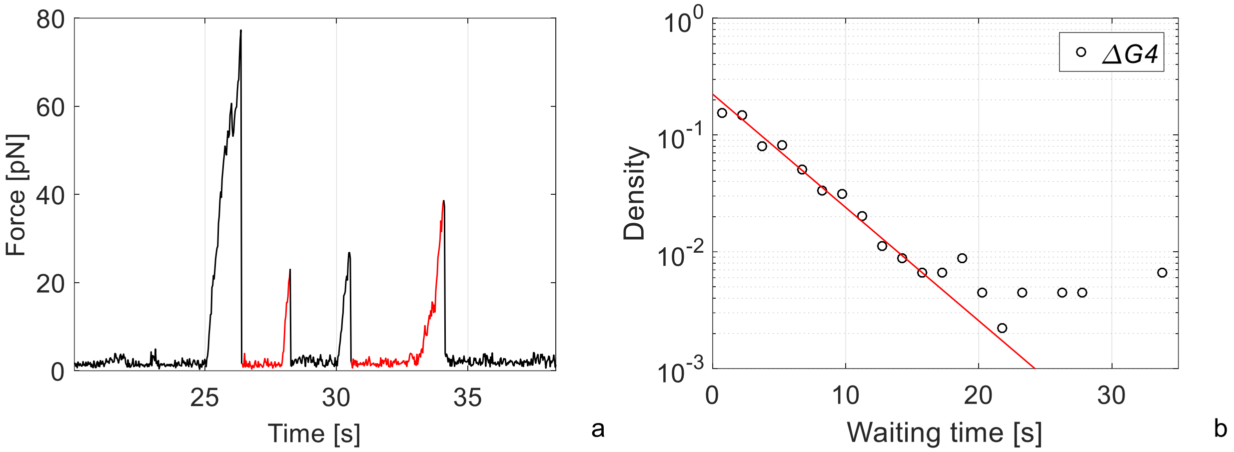

Figure 27: Repetitive single cell interaction of *ΔG4* (Ng150) measured with dual laser tweezers is characterized by waiting times. a) Force proportional to deflection is displayed as a function of time for *ΔG4* cells. Individual interaction events are visible. Red color indicates two exemplary waiting times between events. b) The probability density of waiting times measured with *ΔG4*. An exponential fit is shown as a red line. (N=490)

Data was acquired with *ΔG4* cells. The exponential distribution has the probability distribution $f(t|\mu) = e^{-t/\mu}/\mu$ with mean μ and describes the time between occurrence of events in a Poisson process [148]. If the interaction pattern was a Poisson process, the waiting times between events should be distributed exponentially. The probability density distribution shows a pronounced tail at long waiting times. This result is inconsistent with a Poisson process. The distribution is reminiscent of the waiting time distribution of T4P retracting silica beads (Figure 27) [53].

In conclusion, dual laser tweezer measurements reveal dynamics of intermittent cell-cell interaction is reminiscent of cell-bead interaction, suggesting that the presence of a neighboring cell does not affect T4P dynamics.

5.1.2 Intercellular forces mechanically deform cells

In the previous paragraph we investigated waiting times between repetitive intercellular interactions. Interestingly we observed shape deformations of deflected cells while monitoring cell-cell interactions in dual laser tweezers. In order to characterize this effect, deformations were quantified following the approach of Otto et al. [149]. To this end, the contour of deflected $\Delta G4$ cells was determined for $N = 79$ cells by applying a threshold to gradient images. The contour was fitted by an ellipse in order to gain sub-pixel accuracy. The circularity $c = 2\sqrt{\pi A}/l$ was calculated at equilibrium position $(F_0 = 0\text{ pN})$ and at forces $F_{[30,40]} = F \in [30\text{ pN}, 40\text{ pN}]$, where A and l are area and perimeter. The deformation was then calculated as difference in circularities: $D = \left|c\left(F_{[30,40]}\right) - c(F_0)\right|$. To quantify the background detection level of deformations the deformation based on two equilibrium positions was calculated as well: $D = |c(F_0(t_0)) - c(F_0(t_1))|$. As expected, the cells show a significant increase in deformation under applied force (Figure 28). This has two implications: First, our finding indicates that optical tweezers can be used to systematically investigate contour deformation and cell mechanics on small prokaryotic systems. Second and importantly, cells show contour deformations up to force-levels of 40 pN. It has been shown that these force levels can easily be exceeded by the T4P-machinery, indicating cell deformations in gonococcal aggregates are common and contribute to the elastic properties of biofilms.

In summary, intercellular forces mediated by the T4P retraction machinery mechanically deform cells.

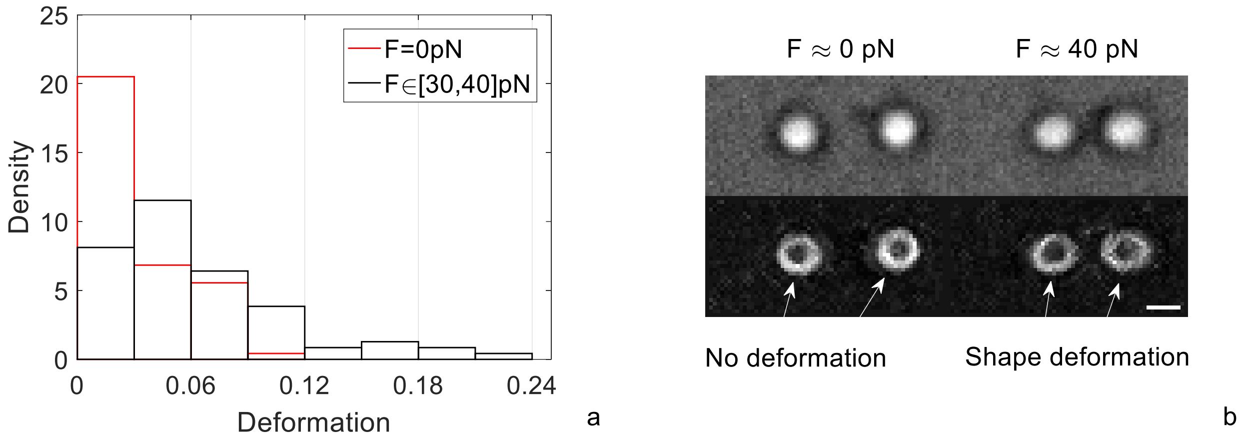

Figure 28: a) Probability densities of detected deformations of *ΔG4* (Ng150). Deformations were detected as difference of circularity values. Cells within their equilibrium position (F=0) showed a background level of detected deformations (red). Under force (F ∈ [30 pN, 40 pN]) cells show increasing values of deformation (black). Probability densities are significantly different (two-dimensional KS-test: $p = 2.6 \cdot 10^{-5}$). N = 79 cells. b) Cells deflect themselves from their equilibrium position (left side) by means of T4P and reach high restoring force levels (right side). x-y-gradient images (bottom) accentuate the cell contour and show cell deformation at large forces. Scale bar: 1 µm.

5.1.3 Interacting gonococci show cell-cell rupture forces around 50 pN

A primary observable to investigate bacterial interaction forces is the rupture force. The dual laser trap setup enabled us to monitor cell-cell interactions and measure the deflections and the force at which the bond between two cells ruptures. First, single cells were trapped in each trap. Binding of T4P to the opposite cell followed by a retraction event led to the deflection of both cells from their equilibrium position. The restoring force is proportional to the increasing deflection of retracting cells and can be calculated by using the trap stiffness. At some point, the restoring force is sufficiently large to break the bond between two interacting cells. Subsequent to bond breakage, the cells are pulled back to the equilibrium position with a velocity that is significantly faster than the fastest velocities that could be resolved by the camera (Figure 29). Notably, these restoring velocities can barely be resolved by 20 kHz detectors [53]. Rupture forces were defined as the maximum force prior to bond breakage. The events appeared as clear signals in the raw data and were summed up into a histogram. As reference strain (wild type) rupture force distributions were measured for cell-pairs of *ΔG4.*

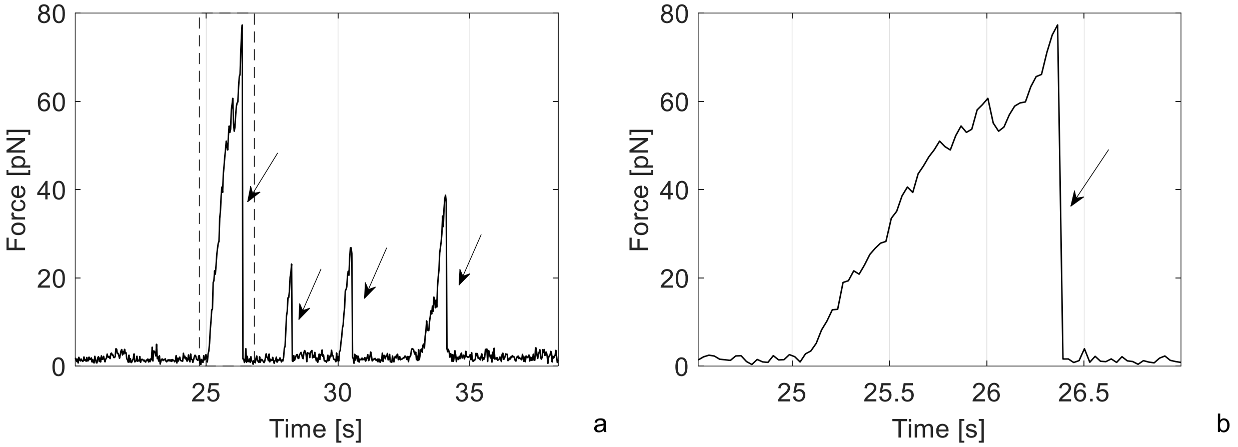

Figure 29: Rupture events of *ΔG4* (Ng150) are marked by arrows. a) Rupture events reappear as clear signals in the raw data. Rupture forces were defined as the maximum force prior to bond breakage. Zoom interval is marked by a dashed line. b) Zoom: Subsequent to bond-rupture, cells are pulled back to the equilibrium position with a velocity that is faster than the camera's resolution (arrow).

ΔG4 cells show rupture forces that occur within a broad range. Interestingly, the distribution does not follow the peak-shaped rupture force distributions that were theoretically predicted for single molecular bonds [150]. The distribution of rupture forces shows a maximum around 50 pN and a tail for forces higher than 80 pN (Figure 30). At 80 pN the linear regime of the dual optical tweezers setup ends (Figure 23). The broad shape at lower forces may be explained by the fact that the force distributions measured with dual laser tweezers are susceptible to generic biological noise. This noise is a consequence of the variability of trapped cells with respect to size, composition, optical properties and stiffness. These factors have the ability to change the actual trapping potential and thereby the restoring force, leading to fluctuations in the measurement of rupture forces. Moreover, the overlap length between the T4P of both cells is likely to vary.

In conclusion, rupture forces between gonococci are distributed around $\sim$ 50 pN.

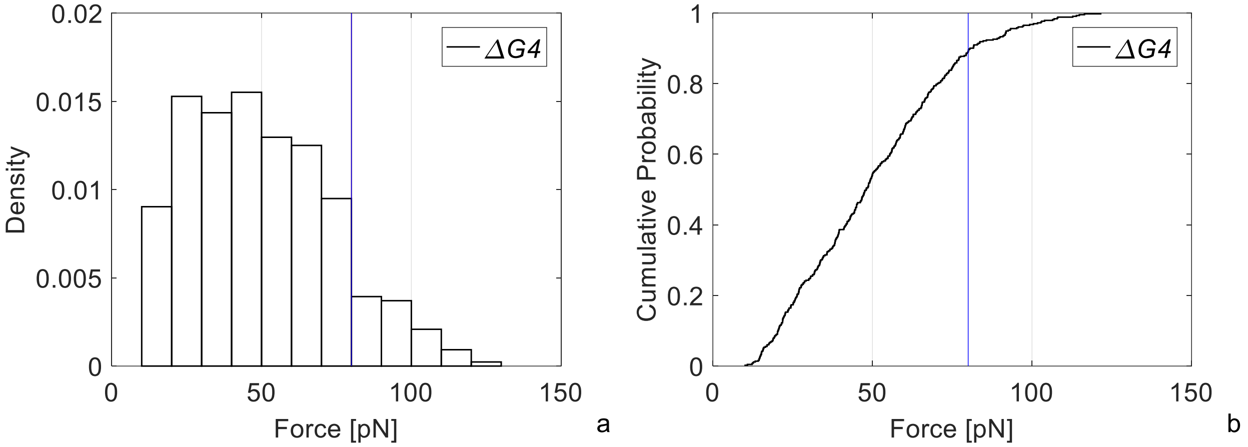

Figure 30: Rupture forces of *ΔG4* (Ng150). Since the linear regime ends at ~ 80 pN (blue line), forces exceeding 80 pN are systematically overestimated. a) Probability density of *ΔG4* rupture forces. b) Cumulative probability of *ΔG4* rupture forces. N = 491 rupture events.

5.1.4 Cell-pairs show varying interaction states during force generation

In addition to rupture forces, that were investigated in the previous paragraph, we characterized the kinetics of T4P-mediated cell-cell interactions. To this end, cell-pairs of *ΔG4* strains were monitored in dual optical tweezers. In addition to rupture events we observed different states of cellular interactions (Figure 31).

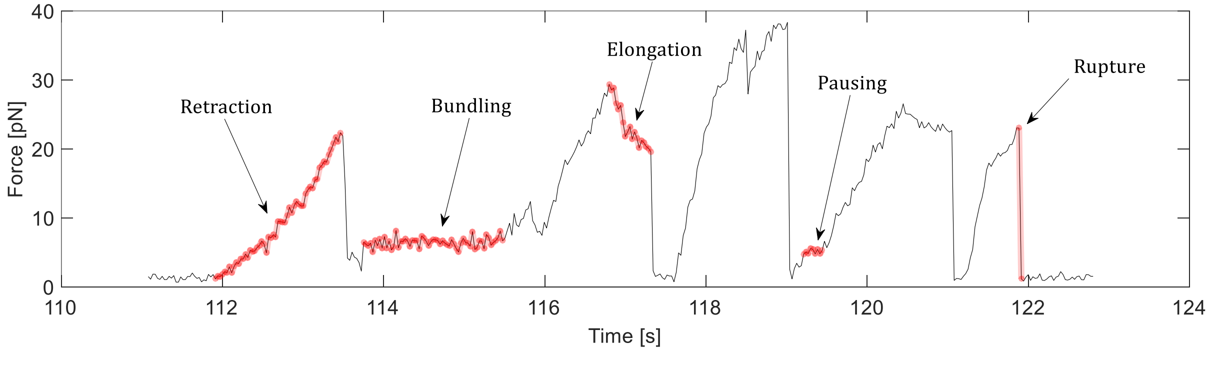

Figure 31: Track of *ΔG4*-cells (Ng150). Raw data of interacting cells was categorized into different states (red). During force generation we observed retraction, bundling, elongation, pausing and rupture events.

Cell pairs showed T4P retraction where both bacteria were pulled towards each other, elongation, where the bacteria moved away from each other, and pausing, where the deflection was constant but nonzero. Sometimes, the cell did not return to the center of the laser trap after a rupture event. In this case was denoted as bundling, where we assume that more than one pilus was bound and while the shortest bond had ruptured, the second shortest bond kept the bacteria deflected from the center of the trap (Figure 31). For the reference strain $\Delta G4$ we found frequencies of elongation-, pausing- and bundling-events in the range of ~ 0.1 Hz (Figure 32). Retraction and rupture frequencies were in the range of ~ 0.8 Hz (Figure 32). We note that elongation, pausing, bundling and rupture events can only be detected after a retraction event. Notably, the determined frequencies allowed us to calculate the probability for two cells to be bound to each other via their T4P. For $\Delta G4$ we found that the probability to be bound is $\rho_{\Delta G4} = (0.15 \pm 0.02)$.

We conclude that gonococci switch between different interaction states during force generation which allow for determination of kinetic parameters like frequencies of elongation, pausing, bundling, retraction and rupture. Furthermore, dual laser tweezers allowed for calculation of the probability for cells to be bound.

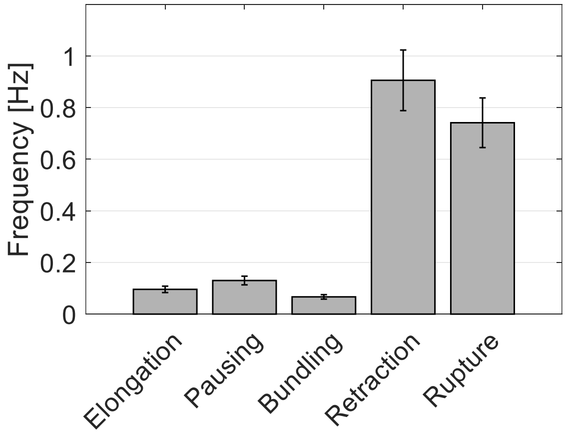

Figure 32: Frequencies of elongation, pausing, bundling, retraction and rupture for *ΔG4*-cells (Ng150). N = (39-529) events.

5.2 PILUS-MEDIATED SINGLE CELL INTERACTIONS DEPEND ON POST TRANSLATIONAL MODIFICATIONS AND VARIATIONS OF MOTOR ACTIVITY

Previous studies revealed, that the T4P machinery and post-translational modifications affect the spatio-temporal dynamics of gonococcal colonies [13][12]. Here, we investigated the role of T4P motor activity and pilin post-translational modifications for cell-cell interactions. To this end, we employed a toolbox of strains. As demonstrated in the previous section, dual laser tweezers are a valuable tool for characterizing cellular interactions. In this section, we used the dual tweezers to characterize cellular interaction forces and dynamics of all strains within our toolbox.

The data presented in the following section is my contribution to the following publications.

A. Welker*, T. Cronenberg*, R. Zöllner* *et al.*, "Molecular Motors Govern Liquidlike Ordering and Fusion Dynamics of Bacterial Colonies," *Phys. Rev. Lett.*, vol. 121, no. 11, p. 118102, Sep. 2018.

R. Zöllner*, T. Cronenberg*, N. Kouzel, A. Welker, M. Koomey, and B. Maier, "Type IV pilin post-translational modifications modulate materials properties of bacterial colonies," *bioRxiv*, p. 389882, Aug. 2018.

* Equal contributions

5.2.1 A toolbox of bacterial strains

In order to investigate the effect of pilin post translational modifications (PTM) and T4P motor activity on intercellular interactions, we used a toolbox of bacterial strains. Specifically, we used strains that have either altered pilin post translational modifications (PTM strains *pglEon* and *ΔpptA)* or modified motor activity (WB strains *WB1* and *WB2*) and compared them to the reference (wild type) strain *ΔG4.*

The strains *pglEon* and *ΔpptA* bear the following modifications. In wild type cells the phase-variable glycosyltransferase gene *pglE* is in the OFF-state. In the strain *pglEon, pglE* is in the ON-state. As a consequence, the corresponding protein PglE adds an additional hexose to the pilins as part of the pilin glycosylation pathway. In the deletion strain *ΔpptA*, the phosphotransferase gene *pptA* is deleted, inhibiting phosphoform modifications of the pilins (Figure 33).

The WB strains express non-functional PilT (PilT_{WB}), in addition to the functional PilT retraction ATPase [151]. PilT_{WB} carries a mutation in the Walker B box that inhibits ATP hydrolysis. Bacterial-two-hybrid assays strongly suggest that functional PilT and non-functional PilTWB proteins form heterohexamers [126]. In *WB1* and *WB2* cells PilTWB is expressed under the control of a weak and a strong promoter, respectively. Hence, *WB1* cells express less non-functional PilTWB and show less strongly impaired T4P motor activity when compared to *WB2* cells [126] (Figure 33). Here, we define motor activity to be the interplay of retraction velocities and the frequencies of T4P retraction, pausing and elongation.

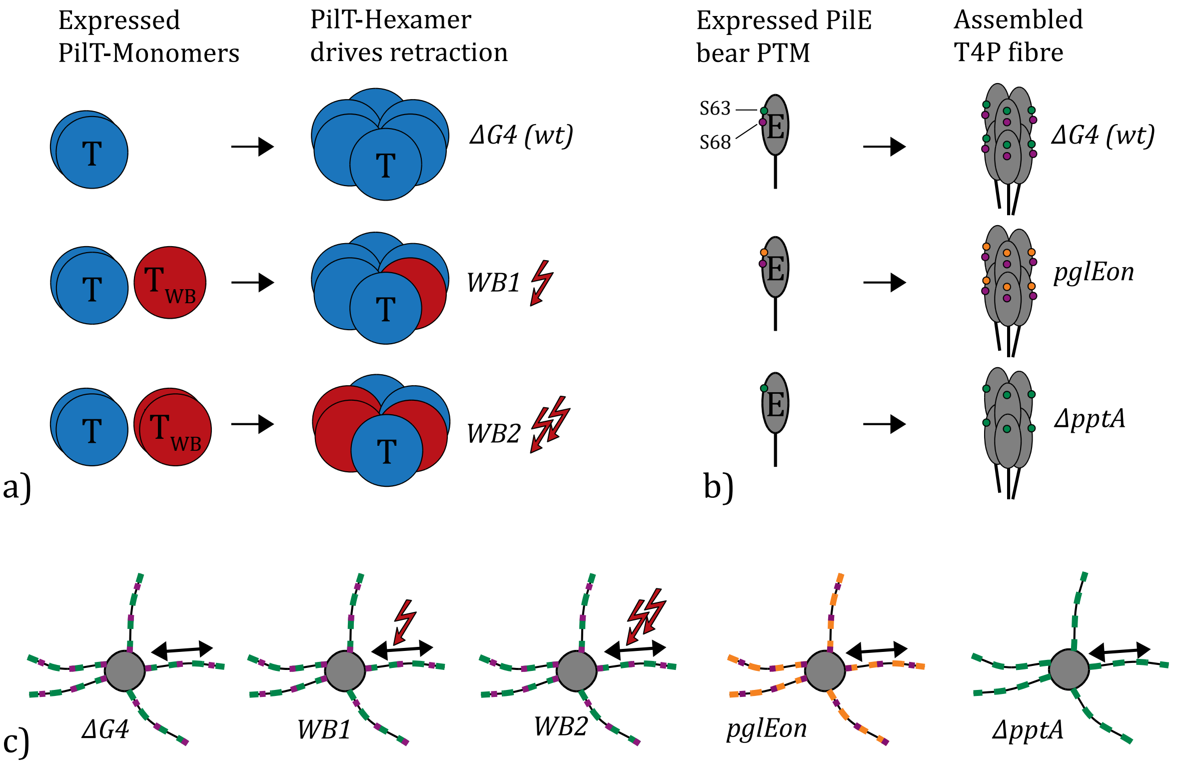

Figure 33: Toolbox of strains. a) In contrast to wild type cells (*ΔG4*), the strains *WB1* and *WB2* express nonfunctional *PilTWB.* As a consequence, the PilT-hexamers that drive T4P retraction show impaired T4P-motor activity (red lightning). *WB2* expresses more PilTWB than *WB1* and shows more strongly impaired motor activity [126]. b) PilE in *ΔG4* cells carrie a phosphoform modification at S68 (purple) and a glycoform modification (green) at S63. In contrast to wild type cells (*ΔG4*), the strains *pglEon* and *ΔpptA* have different pilin post translational modifications. *pglEon* carries an additional hexose at S63 (orange). *ΔpptA* lacks the ability to attach phosphofrom modifications at S68. c) The toolbox consists of the reference (wild type) strain *ΔG4,* the WB strains *WB1* and *WB2* showing impaired T4P-motor activity and the PTM strains *pglEon* and Δ*pptA* bearing variations of pilin post-translational modifications.

5.2.2 Rupture forces are tuned by post translational modifications

In the previous paragraph we have introduced a bacterial toolbox. We utilized this box in order to address the question whether PTM and variations of T4P motor activity affect the physical interaction forces between gonococci. To this end cell-pairs of all toolbox-strains were monitored in dual optical tweezers and rupture forces were measured.

The WB-strains *WB1* and *WB2* show interesting rupture force distributions. The strain *WB2* (showing strongly impaired motor activity [126]) shows rupture forces that are similar to the *ΔG4* strain without significant difference. Unexpectedly, we found a significant difference between *WB1* and *ΔG4* (two-dimensional KS-test: $p = 4.2 \cdot 10^{-4}$). However, this is not a systematic difference that can be explained by the expression of non-functional PilT_{WB}. If this would be the case, we would expect an even stronger effect for the strain *WB2*.

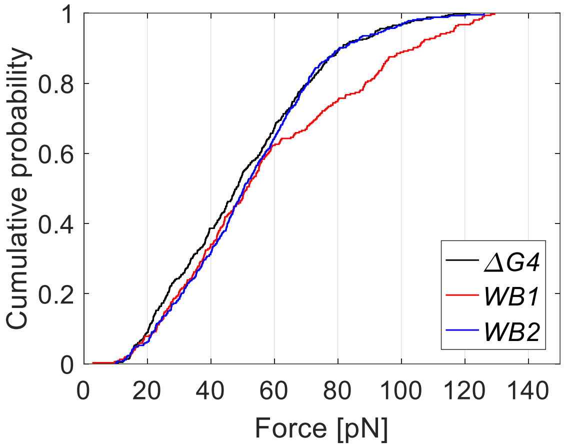

Figure 34: Cumulative probabilities of rupture forces of *ΔG4* (Ng150) and the WB strains *WB1* (Ng171) and *WB2* (Ng176). The linear regime is up to ~80pN. N = (305-491) rupture events.

In order to investigate the impact of PTM on intercellular forces, rupture force distributions were measured for cell-pairs of *ΔG4* and the PTM-strains *pglEon* and *ΔpptA*. Additionally, cross interaction rupture force distributions were measured for the combinations *ΔG4-pglEon* and *ΔG4-ΔpptA*. Interestingly, PTM-strains do show higher rupture forces than *ΔG4* cells (Figure 35). Clearly the distributions show a shift to higher rupture forces that is very distinct for the *ΔpptA* -strain. Even though the majority of *pglEon* rupture forces is close to *ΔG4*, one can clearly see that the distribution is slightly asymmetric and has a heavy tail towards higher forces (Figure 35). Strong differences could be observed: $F_{\Delta G4-\Delta G4} < F_{\Delta pptA-\Delta pptA}$ (two-dimensional KS-test: $p = 1 \cdot 10^{-8}$) $F_{\Delta G4-\Delta G4} < F_{pglEon-pglEon}$ (two-dimensional KS-test: $p = 0.1$). For the cross interactions $F_{pglEon-\Delta G4}$ and $F_{\Delta pptA-\Delta G4}$

asymmetric distributions with slight tendencies towards higher forces without significant difference to $F_{\Delta G4-\Delta G4}$, $F_{\Delta pptA-\Delta pptA}$ and $F_{pglEon-pglEon}$ were found.

In summary, rupture forces between single cells are fine-tuned by pilin post-translational modifications. Rupture force distributions of strains that show impaired T4P-motor activity show no systematic difference in rupture forces.

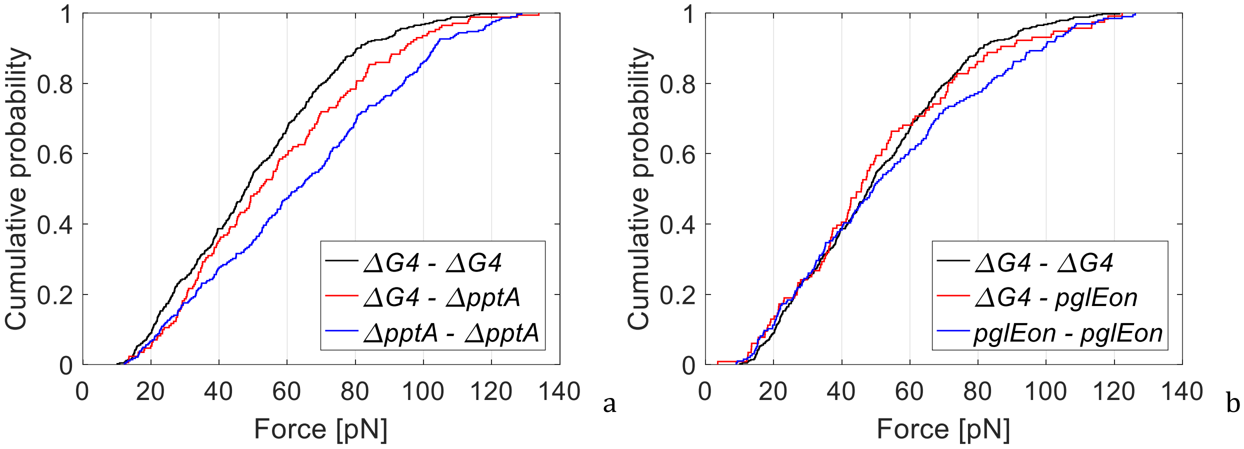

Figure 35: Cumulative probabilities of rupture forces of *ΔG4* (Ng150), the PTM strains *ΔpptA* (Ng142) and *pglEon* (Ng157) and cross interactions. a) Cumulative probabilities of *ΔG4* - *ΔG4*, *ΔG4* - *ΔpptA* and *ΔpptA* - *ΔpptA* rupture forces. b) Cumulative probabilities of *ΔG4* - *ΔG4*, *ΔG4* - *pglEon* and *pglEon* - *pglEon* rupture forces. The linear regime is up to ~80pN. N = (196-491) rupture events.

5.2.3 Interaction kinetics are regulated T4P motor-activity and pilin PTM

We addressed the question whether PTM and variations of T4P motor activity affect the physical interaction kinetics between gonococci. To this end cell-pairs of all toolbox-strains were monitored in dual optical tweezers and the interaction states retraction, bundling, elongation and pausing were analyzed.

Bundling and pausing frequencies were found to be in the order of ~ 0.1 Hz. No striking characteristics for *ΔG4*-, PTM- and WB-cells were observed (Figure 36), except for an increased bundling frequency for the *ΔpptA* -strain and an increased pausing frequency for the *WB1*-strain. The high level of rupture forces of the *ΔpptA* -strain and the high expression level of non-functional PilT_{WB} of the *WB2*-strain may explain these tendencies.

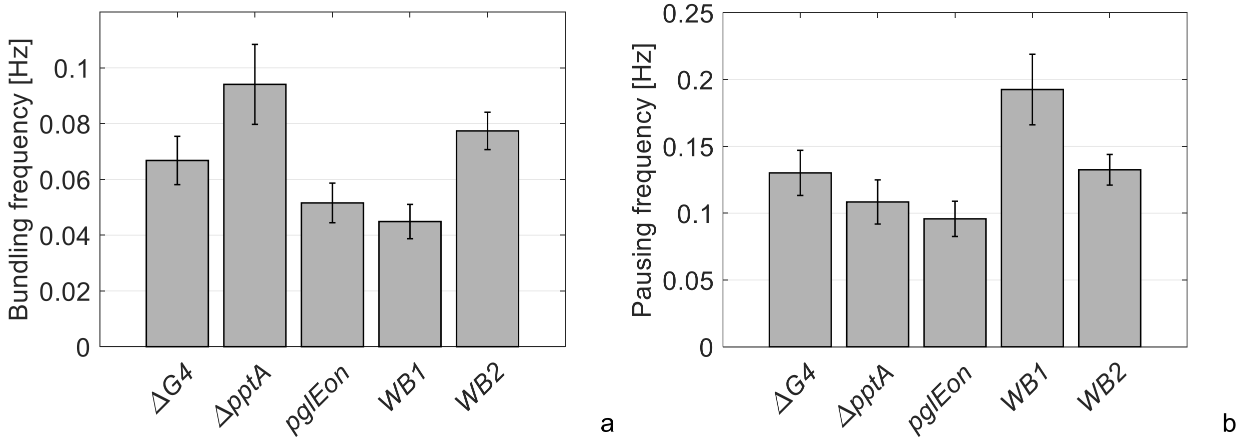

Figure 36: Average bundling and pausing frequencies of *ΔG4*- (Ng150), PTM strains *ΔpptA* (Ng142), *pglEon* (Ng157) and WB strains *WB1* (Ng171), *WB2* (Ng176). a) Bundling frequencies and (b) pausing frequencies were determined by dual trap measurements. Error bars: Bootstrapping with N=100. N = (21-118) bundling events. N = (39-202) pausing events.

The elongation frequencies display clearly that modifications of *pilT* lead to higher rates of elongation. This is consistent to previous results obtained by force-feedback measurements [126]. PTM-strains have an unmodified T4P-motor and show elongation frequencies in the range of *ΔG4*-cells (Figure 37).

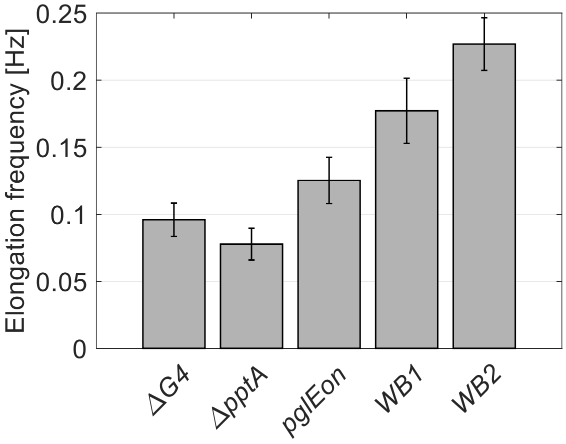

Figure 37: Average elongation frequencies of *ΔG4*- (Ng150), PTM strains *ΔpptA* (Ng142), *pglEon* (Ng157) and WB strains *WB1* (Ng171), *WB2* (Ng176). Elongation frequencies for PTM- and WB-cells were determined by dual trap measurements. Error bars: Bootstrapping with N=100. N = (38-346) elongation events.

For the WB-mutants the frequency of retraction f_{ret} decreases: $f_{ret}^{\Delta G4} > f_{ret}^{WB1} > f_{ret}^{WB2}$ (Figure

38). A similar tendency was found for the frequency of rupture events: $f_{rup}^{\Delta G4} > f_{rup}^{WB1} > f_{rup}^{WB2}$ (Figure 39). The decreasing rate of retraction is consistent with the reduced ability to hydrolyze ATP for T4P-retraction of the WB strains. Additionally, we expected for the WB strains, that the reduced ability to use chemical energy by ATP-hydrolyzation leads to a reduced ability to overcome binding energies and rupture intercellular bonds. This is also confirmed by the decreasing frequency of rupture events.

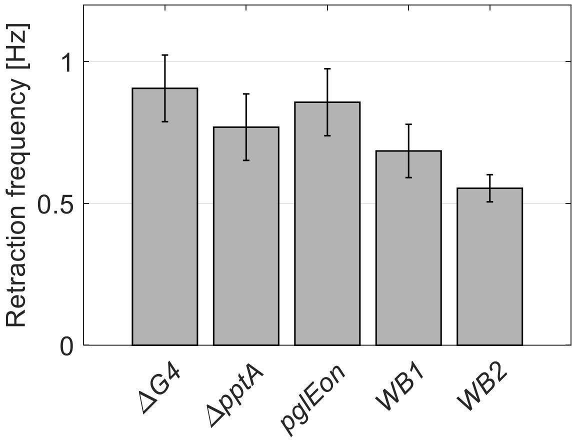

Figure 38: Average retraction frequencies of *ΔG4*- (Ng150), PTM strains *ΔpptA* (Ng142), *pglEon* (Ng157) and WB strains *WB1* (Ng171), *WB2* (Ng176). Retraction frequencies were determined by dual trap measurements. Error bars: Bootstrapping with N=100. N = (376-844) retraction events.

The PTM-strains show a similar tendency for rupture frequencies: $f_{rup}^{\Delta G4} > f_{rup}^{pglEon} > f_{rup}^{\Delta pptA}$ (Figure 39). Notably, PTM-retraction rates characterized by f_{ret} were roughly on *ΔG4*-level: $f_{ret}^{\Delta G4} \approx f_{ret}^{pglEon} \approx f_{ret}^{\Delta pptA}$ (Figure 39). The decreasing frequency of rupture is consistent to increased intercellular rupture forces, that lead to fewer rupture events between PTM-cells. The constant rates of retraction for the PTM-cells can be explained by the fact that the T4P-machinery is unmodified and the *ΔG4*-amount of ATP is used per unit time to generate retractions.

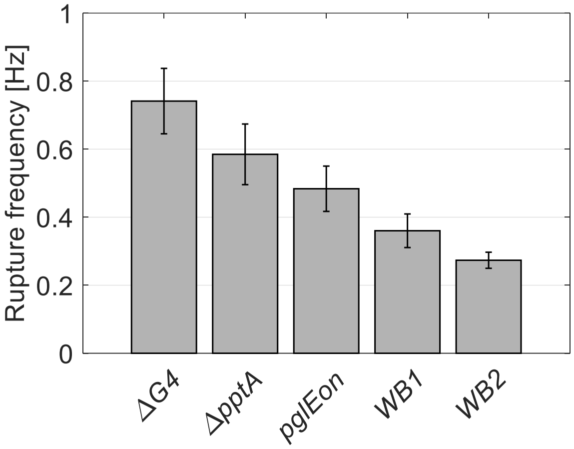

Figure 39: Average rupture frequencies of *ΔG4*- (Ng150), PTM strains *ΔpptA* (Ng142), *pglEon* (Ng157) and WB strains *WB1* (Ng171), *WB2* (Ng176). Rupture frequencies were determined by dual trap measurements. Error bars: Bootstrapping with N=100. N = (197-433) rupture events.

As mentioned above, dynamical parameters characterize intercellular interaction kinetics. A global parameter, that combines the rates of retraction, rupture, elongation, pausing and bundling is the probability, ρ, that two cells are bound to each other.

The probability, ρ, that two cells are bound to each other was calculated from single cell interaction measurements. ρ was calculated for *ΔG4*-, PTM- and WB-cells. Values of $\rho_{\Delta G4} = (0.15 \pm 0.02)$, $\rho_{\Delta pptA} = (0.24 \pm 0.04)$, $\rho_{pglEon} = (0.22 \pm 0.03)$, $\rho_{WB1} = (0.24 \pm 0.03)$ and $\rho_{WB2} = (0.37 \pm 0.03)$ were determined (Figure 42). Interestingly, both WB- and PTM-strains show a significant increase in probability to be bound to adjacent cells.

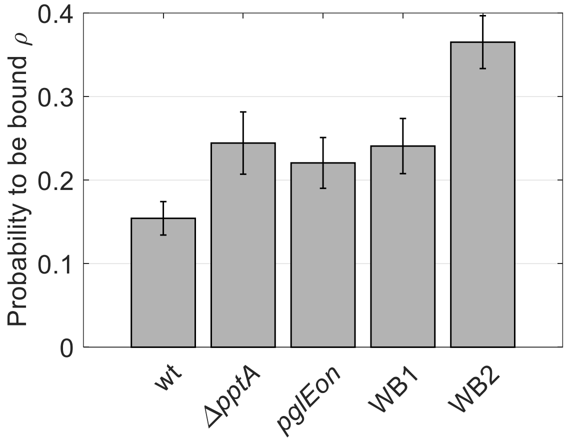

Figure 40: Probability for two gonococci to be bound for *ΔG4*- (Ng150), PTM strains *ΔpptA* (Ng142), *pglEon* (Ng157) and WB strains *WB1* (Ng171), *WB2* (Ng176). Probabilities for PTM and WB-cells were determined by dual trap measurements. Error bars: Bootstrapping with N = 100.

In summary, frequencies of retraction, rupture and elongation are tunable by modifications of the T4P-motor and PTM. PTM do not affect retraction and elongation frequencies but decrease the number of rupture events per time. Motor deficient WB strains show increased elongation rates and decreased rupture and retraction rates. With respect to *ΔG4*-cells, PTM- and WB-strains show increased probabilities to be bound to adjacent cells.

5.2.4 Cellular interactions govern material properties and sorting dynamics of colonies

As demonstrated, T4P motor-activity and pilin post translational modifications (PTM) regulate interaction kinetics and probabilities to be bound. Based on the discovered kinetics, the impact of single cell interactions on multicellular collective systems was investigated. To this end observations of cell sorting in early biofilms studied by Dr. Nadzeya Kouzel and colony fusions studied by Tom Cronenberg were connected to above-described single cell interaction kinetics.

Early biofilms observed in flow chambers show cell sorting between *ΔG4* and strains carrying different pilin PTM, specifically glycosylation-inhibited *ΔpglF* cells [13][87]. On the basis of the differential strength of adhesion hypothesis (DSAH), sorting can be explained by differential rupture forces [107]. The findings described in the previous chapters, namely

$F_{\Delta G4-\Delta G4} < F_{\Delta pptA-\Delta pptA}$ and $F_{\Delta G4-\Delta G4} < F_{pglEon-pglEon}$, thus predict that PTM-cells segregate to the center of an early biofilm whereas the *ΔG4*-cells spread around the core homogeneously [109]. Notably, a significantly increased probability of being bound was observed for cells with pilin PTMs that differed from the wt (Figure 40). Cells with high binding probabilities will tend to form clusters. Hence, differences in binding probabilities support phase separation. In combination with differences in rupture forces, these contributions to cell sorting are likely to be sufficient to induce phase separation between wild-type *ΔG4*-cells and PTM-cells. To test these predictions, *ΔG4*- and strains carrying different pilin PTM were mixed in flow chambers and sorting behavior was monitored. Strikingly, both *pglEon* and *ΔpptA* cells were encased by *ΔG4*-cells when mixed with the latter, strongly supporting our predictions based on rupture force measurements (Figure 41).

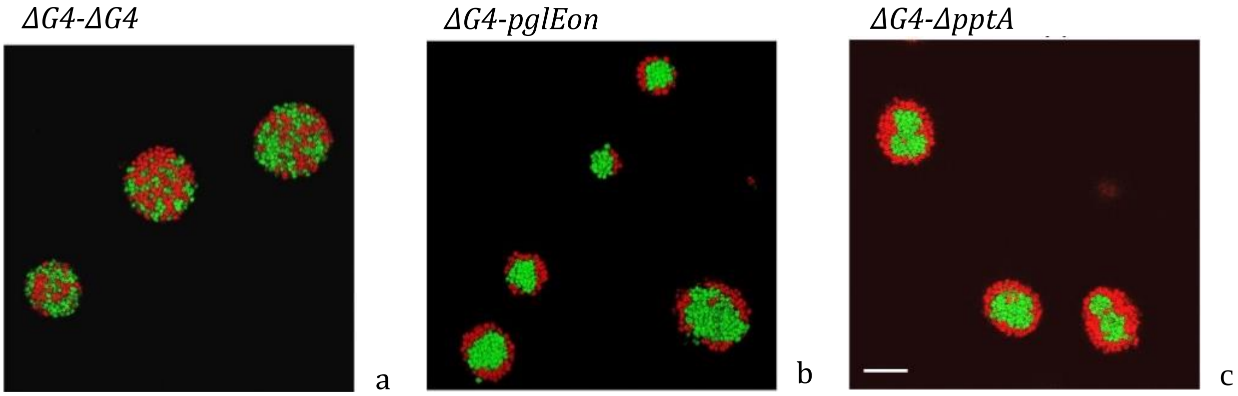
ΔG4-ΔG4 *ΔG4-pglEon* *ΔG4-ΔpptA*

Figure 41: Cross-interaction of *ΔG4*- (Ng150, red), PTM strains *ΔpptA* (Ng142, green), *pglEon* (Ng157, green) and triggered cell sorting in gonococcal microcolonies. Display of 1:1 inoculations of a) *ΔG4-ΔG4*, b) *ΔG4-ΔpptA* and c) *ΔG4-pglEon.* After 5h of growth (done by Dr. Nadzeya Kouzel), colonies were prepared imaged by confocal microscopy (done by Anton Welker). Adapted from [87].

In the previous paragraph it was demonstrated that positioning within biofilms and sorting are linked to intercellular interactions. Next, we aimed at linking interactions to dynamical behavior of biofilms, which can be quantified by shape relaxation and fusion dynamics [152][153]. Aggregates composed of cells with high probability to be bound should show a more viscous behavior, whereas low probabilities should lead to less viscous material properties. Hence, we investigated whether the dynamical behavior of biofilms is governed by interactions at the single cell level.

Multicellular collective dynamics of early biofilms were characterized by means of colony fusion assays providing the parameter σ/η (Figure 42) [126][12]. σ denotes the surface tension and η the viscosity of the biofilm. It was found σ/η is strongly decreased for PTM- and WB-strains when compared to wt-cells: $(\sigma/\eta)_{\Delta G4} = (148 \pm 11)$ nm/s, $(\sigma/\eta)_{pglEon} = (22 \pm 5)$ nm/s and $(\sigma/\eta)_{WB1} = (37 \pm 6)$ nm/s. Notably, colonies of *ΔpptA* -cells fused even more slowly, so that σ/η could not be determined using the colony fusion assay. However, qualitatively the data shows clearly that σ/η of *WB2*- and *ΔpptA* -cells is even smaller than for *WB1*- and *pglEon*-cells, suggesting glass-like behaviour (Figure 42). Strikingly, this mesoscopic evaluation of early biofilm dynamics is consistent to the binding probabilities found in this study (Figure 40). High binding probabilities translate into viscous behavior and slow fusion dynamics characterized by low values of σ/η.

We used the rupture force $F_{rupture}$ and the probability for adjacent cells to be bound, ρ, to estimate the surface tension $\sigma = F\Delta x \ /\Delta A$ where $F\Delta x$ is the work required to increase the surface area by ΔA. The work required for moving one bacterium from the bulk to the surface by the distance D is estimated as follows. The diameter of a bacterium is $D \approx 0.7$ µm, the average number of T4P per cell is $N \approx 7$, and the increase in surface area is $\Delta A \approx \pi(D/2)^2 \approx 0.4$ µm^2. We assume that half of the pili are not bound when the bacterium resides at the surface. Together, we estimate the surface tension to be given by

$$\sigma = \frac{1}{2} N\rho \frac{F_{rupture}\, D}{\pi\, (D/2)^2}\,. \tag{16}$$

Surface tensions were estimated to be $\sigma_{wt} \approx 5 \cdot 10^{-5}$ N/m and $\sigma_{WB1} \approx 8 \cdot 10^{-5}$ N/m resulting in viscosity values of $\eta_{wt} \approx 350$ Nsm^{-2} and $\eta_{WB1} \approx 2000$ Nsm^{-2} [126]. These diverse viscosity values hint that ρ is directly coupled to σ/η.

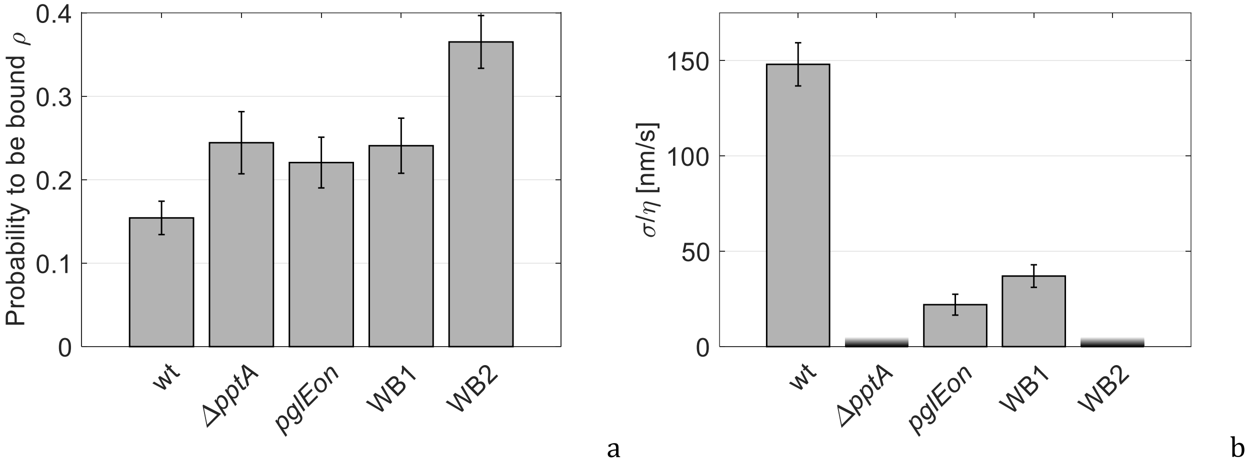

Figure 42: a) Probabilities to be bound for *ΔG4*- (Ng150), PTM strains *ΔpptA* (Ng142), *pglEon* (Ng157) and WB strains *WB1* (Ng171), *WB2* (Ng176). Probabilities to be bound for PTM and WB-cells were determined by dual trap measurements. Error bars: Bootstrapping with N = 100. b) σ/η of *ΔG4*-, PTM- and WB-cells was determined by colony fusions in flow chambers by Tom Cronenberg [126]. Fading bars of *ΔpptA* and *WB2* mark no quantitative results but qualitative observations that indicate low values of σ/η. Error bars: Standard deviation. N > 30 fusion events.

In summary, changes of rupture forces and probabilities to be bound induce collective cell sorting in early biofilms. Furthermore, the probability ρ that gonococci are bound via T4P is directly linked to surface tension and viscosity of gonococcal microcolonies. Interestingly, the probabilities ρ may be tuned either by varying T4P motor activity or by modifying the rupture forces.

5.2.5 Pilin post-translational modification does not affect the generation time

As demonstrated, collective sorting behavior within model biofilms can be explained by rupture forces and probabilities to be bound. In order to verify that the soring behavior is not biased by altered generation times the generation times of all PTM-strains were measured. Generation times $t_{\Delta G4} = (46{,}5 \pm 3{,}9)$ min, $t_{pglEon} = (44.2 \pm 2.7)$ min and $t_{\Delta pptA} = (43.9 \pm 2.7)$ min, were found. These values indicate that PTM do not affect the division time (Figure 43). Hence, sorting behavior is not biased by altered generation times.

In summary, generation times are not affected by PTM. Hence, collective sorting behavior of

PTM-mutants in early biofilms is not biased by selection.

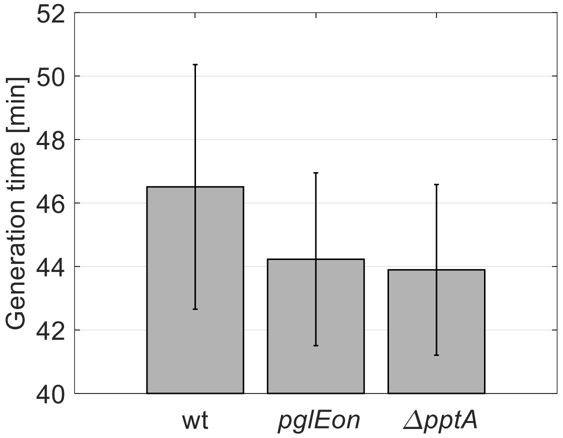

Figure 43: Pilin post-translational modification does not affect the generation time. The generation times of strains of *ΔG4*- (Ng150), *ΔpptA* (Ng142) and *pglEon* (Ng157) were determined during exponential growth on agar plates. Error bars: standard deviations form ≥ 90 colonies for each strain.

5.3 T4P-MOTOR DEFICIENT *PILT*-DELETION STRAINS ARE ABLE TO GENERATE FORCES BY MEANS OF T4P

pilT deletion strains have been shown to lack competence and motility [154]. For a long time, this effect was thought to be linked to the absence of T4P retraction in *pilT* deletion strains. However, recent studies found evidence for generic *pilT*-independent T4P retraction in various species [155][156].

The data presented in the following section is my contribution to the following publications.

R. Zöllner*, T. Cronenberg* and B. Maier, "Motor properties of PilT-independent type 4 pilus retraction in gonococci," *in preparation*

*Equal contributions

5.3.1 Gonococci retract T4P in the absence of the T4P retraction ATPase PilT

To investigate whether N. gonorrhoeae shows T4P retraction in the absence of the retraction ATPase PilT, the dual laser tweezers setup was utilized to characterize binding between retraction deficient cells. Strikingly, force generation of retraction ATPase deficient cells could be observed at low trap stiffness (Figure 44). The trapping laser was adjusted to low powers to trap piliated but retraction ATPase-deficient *ΔpilT*-cells. At 2% of the maximum laser power a trap stiffness value of $k \approx 0.002$ pN/nm was obtained.

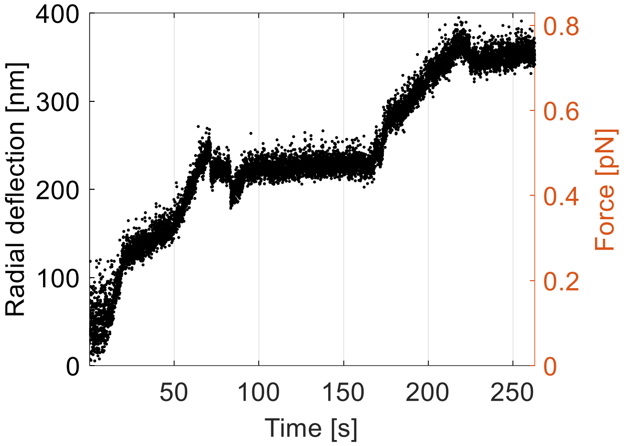

Figure 44: Force generation of *ΔpilT*-cells (Ng178) in dual laser tweezers at low trap stiffness values ($k_{2\%}$~2fN/nm). Two *ΔpilT*-cells bind, generate forces and deflect themselves from the equilibrium position. The resulting mean radial deflection of one binding event is exemplarily displayed as a function of time.

First, we tested whether the composition of the medium affects the force generation qualitatively. GC- and RA-medium and PBS buffer were used as media, respectively. All three media have been shown to allow characterization of active processes, such as DNA-uptake, T4P-retraction and twitching motility [157][158]. GC medium is an undefined rich medium with numerous undefined ingredients. RAM is a well-defined cell culture medium and PBS is a buffer solution without any metabolic ingredients. Force generation of the strain *ΔpilT* was observed in all three media. Subsequent experiments were performed in RAM.

It was conceivable that force generation between two piliated cells was a generic effect of increasing overlap of two pili. To distinguish between this generic effect and *pilT* independent retraction, we trapped a *ΔpilT*-cell in one trap and a glass bead in the other trap at 2% laser power. A glass bead and one cell were trapped at 2% laser power. Interestingly, deflections from the equilibrium position were found, indicating that the second cell was not required for force generation by *ΔpilT*-cells (Figure 45). The attractive cell-bead interaction is likely to have the same origin as cell-cell interaction.

This observation shows that the attractive interaction between two *ΔpilT*-cells is not based on increasing overlap of two pili. If this basic model would hold, we would expect no force generation between a piliated cell and a clean glass surface. The similar logic applies to a model that suggests an increasing overlap between the neighboring cell body and a pilus. Hence, attractive interaction shows no indication of a generically increasing overlap of T4P and is likely to have a different origin.

Moreover, the glass bead was not coated with DNA. To detect gonococcal DNA-uptake, DNA-coated beads are essential [159]. As a consequence, cell-bead interactions cannot be caused by DNA uptake events. Hence, cell-cell interaction is highly unlikely to be caused by the DNA-uptake machinery of gonococci. Notably, gonococci have no further extracellular structures other than the T4P- and the DNA-uptake-machinery to actively generate forces [160]. Since DNA is unlikely to be involved, a plausible explanation for the attractive interaction between two *ΔpilT*-cells is pilus retraction that is not driven by ATP-hydrolysis of PilT.

In summary, force generation of *ΔpilT*-cells is independent of the chemical composition of the medium. More importantly, attractive cell-cell and cell-bead interactions were observed, indicating no generically increasing overlap of pili and no involvement of the gonococcal DNA-uptake machinery. We conclude therefore, that gonococcal T4P retract even in the absence of the retraction ATPase PilT.

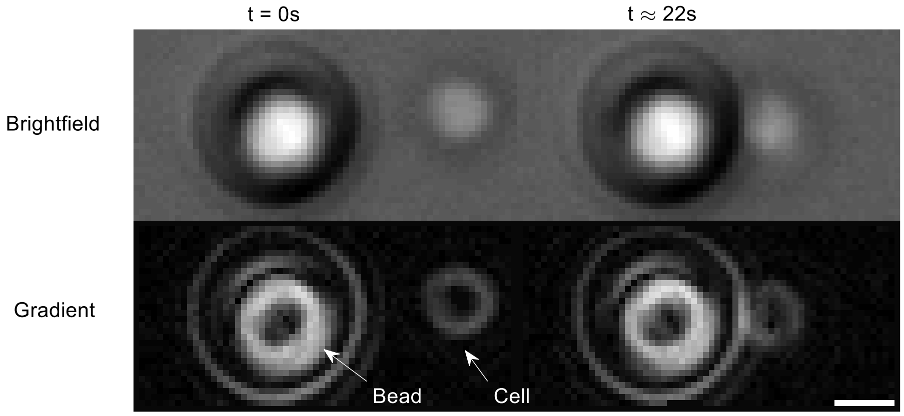

Figure 45: Force generation of *ΔpilT*-cells (Ng178) in dual laser tweezers at low trap stiffness values ($k_{2\%}$~2 fN/nm). A motor deficient cell binds to an uncoated glass bead, generates small forces and deflects itself from the equilibrium position (left side). The cell reaches large deflections after ~22 s (right side). x-y-gradient images (bottom) accentuate bead and cell contour. Scale bar: 1 µm.

5.3.2 *pilT* independent retraction is two orders of magnitude slower than *pilT* driven retraction

In the previous section, it was shown that force generation without functional *pilT* is likely to be caused by *pilT*-independent pilus retraction. Compared to *pilT*-driven pilus retraction of wt-cells the time scale of retraction events is very long (Figure 45). Typically, wt-pilus retraction of a full pilus occurs on a timescale of ~1 s [161], whereas *pilT* independent retraction has a timescale that is ~1min (Figure 44). We quantified these qualitative differences in time scales by measuring the retraction velocities in the dual laser tweezer setup. Pairs of *ΔpilT* were trapped in two optical traps at 2% of the maximum trapping laser power. Slow retractions were monitored and retraction velocities were calculated from the tracks of the bacteria. A median retraction velocity of $v_{2\%} = (6.2 \pm 3.2)$ nm/s was found for *ΔpilT* at 2% laser power, which is equivalent to a trap stiffness of $k_{2\%}$~2 fN/nm (Figure 78). This value is much slower when compared to speeds of PilT-driven retractions [162].

Elastic effects introduce a systematic error in dual-trap velocity-measurements. Therefore, in collaboration with Tom Cronenberg, it was tested tested whether *pilT* independent retraction is observable in single laser trap force feedback measurements. To this end a previously established protocol was used [126]. Consistent to previous findings, velocities acquired at forces clamped at 8 pN were lower when compared to velocities that were measured at forces clamped at 4 pN. Significantly different median values of $v_{\text{4pN}} = (41.4 \pm 18.0)$ nm/s and $v_{\text{8pN}} = (18.1 \pm 11.2)$ nm/s were found (two-dimensional KS-test: p = $3.7 \cdot 10^{-17}$). Most importantly, feedback data confirms that *pilT*-independent retraction velocities differs by two orders of magnitude when compared to *pilT*-driven retraction (Figure 46).

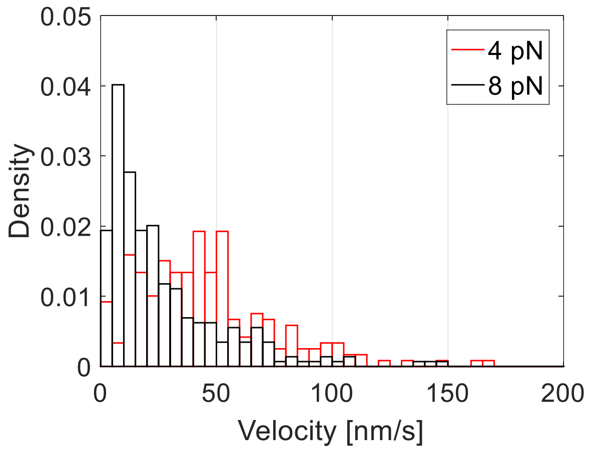

Figure 46: Retraction velocities of *ΔpilT*-cells (Ng178). In collaboration with Tom Cronenberg velocities were measured at 4 pN and 8 pN feedback force with laser tweezers following a previously established protocol [126]. N = (239-289).

Stalling events could be observed in single laser trap measurements. These events indicate that the PilT-independent retraction machinery stalls on average at forces lower than 10 pN: $F_s = (6.3 \pm 2.0)$ pN (Figure 47).

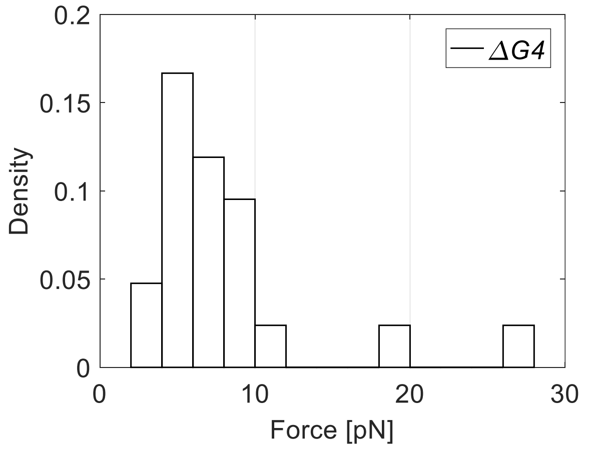

Figure 47: Stalling forces of *ΔpilT*-cells (Ng178). In collaboration with Tom Cronenberg forces were measured with laser tweezers following a previously established protocol [126]. N = 21 stalling events.

In summary, PilT-independent retraction velocities are lower by two orders of magnitude when compared to wild type retractions. The observed retraction is significantly slower for increasing opposing force levels. Average stalling forces were lower than 10 pN.

5.3.3 *pilT* independent retraction is not driven by *pilT2* or *pilU*

pilT2 and *pilU* have a high sequence similarity to *pilT* [124][163][164]. They are considered to be *pilT* paralogues. In order to test whether attractive cell-cell interaction of *pilT*-mutants is based on pilus retraction driven by *pilT2* or *pilU* three knockout strains were generated: *ΔpilT ΔpilT2, ΔpilT ΔpilU* and *ΔpilT ΔpilT2 ΔpilU.* All three knockout strains were trapped separately in the dual laser tweezers and monitored at $k_{2\%}$~2 fN/nm.
Interestingly, all three strains showed the attractive cell-cell interactions similar to Figure 45 found for the *ΔpilT*-strain. This shows that the force generation of *ΔpilT* is not linked to *pilT2* or *pilU.*

Strain	Genotype	Force Generation
ΔpilT	*G4::aprR pilT::cmR*	yes
ΔpilT ΔpilT2	*G4::aprR pilT::cmR pilT2::kanR*	yes
ΔpilT ΔpilU	*G4::aprR pilT::cmR pilU::ermC*	yes
ΔpilT ΔpilT2 ΔpilU	*G4::aprR pilT::cmR pilT2::kanR pilU::ermC*	yes

Table 6: Force generation of *pilU* and *pilT2* depletion strains.

In summary, the triple knockout strain *ΔpilT ΔpilT2 ΔpilU* shows T4P-retraction. We conclude that neither *pilT2* nor *pilU* are the cause of force generation in the absence functional *pilT*.

5.3.4 *pilT* independent retraction is not driven by proton motive force

The observed *pilT*-independent force generation is not possible without an internal energy source. All theoretical explanations that lack an energy source are incompatible with the second law of thermodynamics. The proton motive force (PMF) is related to a proton-based chemical potential across a membrane and the driving force of several transport machineries and molecular motors [165][166][167]. Consequently, we hypothesized that PMF may be the energy source behind *pilT*-independent force generation by T4P. To test this hypothesis, *ΔpilT* cells were treated with the uncoupler carbonyl cyanidem-chlorophenyl hydrazone

(CCCP). CCCP shuttles protons across the membrane, in the direction of the proton gradient and deplete PMF [168]. Cells were incubated with 50 µM CCCP for 15 min prior to usage in dual laser tweezers. Notably, *ΔpilT* cells are able to generate forces after 15min and up to 50min of CCCP-treatment. To check that 15min are sufficient to affect cells, twitching motility of *ΔG4* was checked. Consistent to previous results, cells showed low twitching motility after 15 min of treatment with 50 µM CCCP and high twitching motility without CCCP [169]. We conclude that *pilT*-independent retraction is not driven by proton motive force.

5.3.5 *pilE* expression levels affect *pilT* independent retraction

Finally, we addressed the question whether the concentration of pilin subunits PilE affects the dynamics of *pilT*-independent T4P retraction. The PilE-concentration in the periplasm was manipulated. Strain expressing higher (*3xpilE*) and lower (*pilE$_{ind}$*) levels of *pilE* compared to the wild type were generated. We expected that high levels of periplasmatic PilE stops or slows the energetically favored retraction. In contrast to that, lowered periplasmatic PilE-concentrations should induce faster retractions. We tuned the periplasmatic PilE-concentration with two genetic constructs. The construct for high concentrations is added to the chromosome in the *iga*-locus. In this non-essential locus, two copies of *pilE* were inserted, leading to three separately expressed *pilE*-genes (*3xpilE*) [13]. For low concentrations we replaced the native *pilE*-sequence with an inducible *pilE* sequence (*pilE$_{ind}$*) [84]. The induced promoter has a significantly lowered expression-level [126].

Strain	Genotype	Force Generation
ΔpilT	*G4::aprR pilT::cmR*	yes
pilE$_{ind}$	*G4::aprR pilT::cmR pilT2::kanR*	yes
3xpilE	*G4::aprR pilT::cmR pilU::ermC*	yes

Table 7: Force generation of modified PilE expression strains *pilE$_{ind}$* and *3xpilE.*

Since velocities could not be measured with dual optical tweezers, we characterized velocities of *3xpilE* and *pilE$_{ind}$* with single trap force feedback measurements. Unfortunately, the strain *pilE_{ind}* could not be characterized due to its low probability to bind to trapped glass beads. Significantly different median values of $v_{4\mathrm{pN}-\Delta pilT} = (41.4 \pm 18.0)\ \mathrm{nm/s}$ and $v_{4\mathrm{pN}-3xpilE} = (11.4 \pm 6.8)\ \mathrm{nm/s}$ were found (two-dimensional KS-test: $p = 1 \cdot 10^{-27}$). Most importantly, feedback data demonstrates that *pilT*-independent retraction is significantly slowed by increasing PilE concentrations (Figure 48).

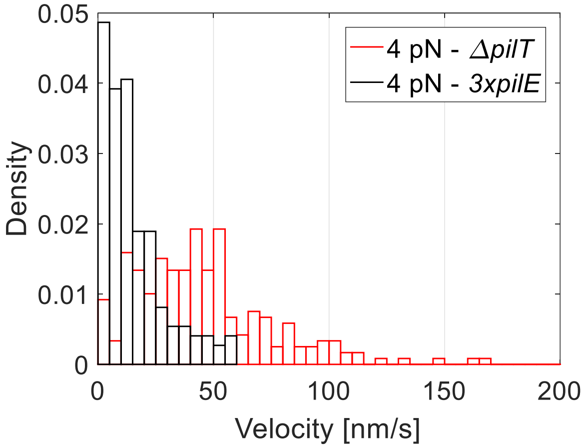

Figure 48: Retraction velocities of *ΔpilT* and *3xpilE* -cells. In collaboration with Tom Cronenberg, velocities were measured at 4 pN feedback force with single trap laser tweezers following a previously established protocol [126]. N = (148-239).

In summary, *pilT*-independent retraction is observed for the strains *3xpilE* and *pilE$_{ind}$*. At increased PilE concentrations, the velocities become lower.

5.4 CELLULAR INTERACTION FORCES GOVERN BACTERIAL POSITIONING AND POPULATION DYNAMICS OF MACROSCOPIC BIOFILMS

In the previous sections, single cell interactions were characterized and linked to macroscopic parameters. In this section the scope is enlarged and macroscopic biofilms are characterized. Specifically, it was investigated, whether single cell interactions directly affect positioning in biofilms and resulting fitness-dependent population dynamics. To this end macroscopic expanding populations were grown on solid agar surfaces following the experimental approach of Hallatschek et al. [112]. The expanding populations, show pattern formation during growth and are named range expansions. These expansions served as biofilm model allowing for investigation of mutational loss of pilus-mediated interaction, positioning and resulting population dynamics.

The results shown in this section were performed in close collaboration with Dr. Enno Oldewurtel and were published under

R. Zöllner*, E. R. Oldewurtel*, N. Kouzel, and B. Maier, “Phase and antigenic variation govern competition dynamics through positioning in bacterial colonies,” *Sci. Rep.*, vol. 7, no. 1, p. 12151, 2017.

*Equal contributions

5.4.1 Unpiliated cells are subject to segregation and surf on the front of growing colonies

It has been shown that loss of piliation reduces intercellular interactions to an undetectable level [13]. These weakly interacting cells are characterized by a flat colony morphology on agar [170][171]. Unpiliated (weakly interacting, P-) cells segregate to the front of growing colonies, whereas piliated (strongly interacting, P+) cells stay in the center of the colony [13]. We hypothesized that weakly interacting cells are able to maintain their frontal position during colony growth even if their growth rate is reduced.

To test this hypothesis, two strains that allowed us to independently tune the growth rate and the state of piliation/interaction were created [79] (Section 4.1.2.5). *red ermC*+, expresses a red fluorescent reporter and is resistant against erythromycin. The second strain *green*^{Q} *ermC*- expresses a green fluorescent reporter, is also resistant against erythromycin but shows a weaker resistance level compared to *red ermC*+. Hence, the notation *ermC*± was used. Additionally, the strain *green*^{Q} *ermC*- lacks the outer membrane pore *pilQ*. As a consequence, *green*^{Q} *ermC*- is unpiliated and weakly interacting. For both strains the generation times were measured in the exponential phase (Figure 49). Importantly, it has been shown that the deletion of *pilQ* changes the generation time by a negligible factor [13].

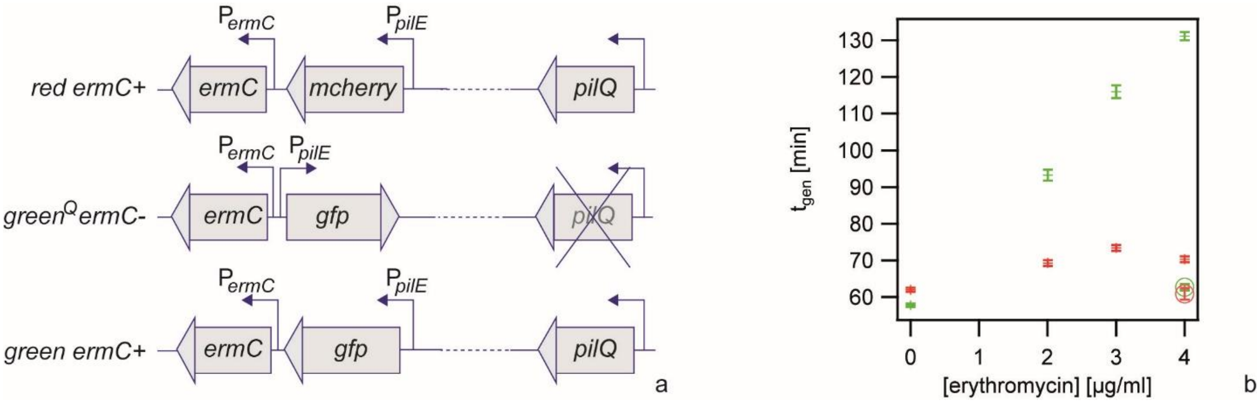

Figure 49: Tuning exponential growth rates and bacterial interaction force independently. a) Different constructs used. b) Generation times of the strains shown in a) as a function of the concentration of erythromycin. Red cross: *red ermC+* (Ng065), green cross: *green^Q ermC-* (Ng118), red circle: *red ermC+* (control), green circle: *green ermC+* (Ng117) (control). The generation times varied slightly between days (red cross and red circle) and thus different strains were always grown on the same plate for comparison. Error bars: standard errors of the mean, N = (166 – 1206) colonies. Adapted from [79].

Typically, strains with higher growth rates are fitter and tend to fix within populations [110]. It was tested whether weakly interacting *green^Q ermC-* cells are able to maintain their frontal position during colony growth despite a strongly decreased growth rate. To this end *green^Q ermC-* and *red ermC+* were inoculated on agar containing [erm] = 4 µg/ml. As a consequence of the presence of 4 µg/ml erythromycin, the growth rates of *green^Q ermC-* and *red ermC+* differ by a factor of $r_t = t_{gen}(green^Q\ ermC-)/t_{gen}(red\ ermC+) = 1.9$. Under these conditions a mix of the inoculated *green^Q ermC-* and *red ermC+* cells were monitored over 10 hours.

Data shows that fast growing and strongly interacting *red ermC+* cells were able to push slowly growing and weakly interacting *green^Q ermC-* over the agar surface (Figure 50). This observation is similar to previously described gene surfing in expanding populations [172][117] and has two implications: First, frontal position of weakly interacting cells is not disturbed by an increased growth rate. Second, weakly interacting cells are able to maintain their position throughout the exponential growth phase.

In conclusion, weakly interacting cells are able to surf on the front of expanding strongly interacting cells despite a decreased growth rate.

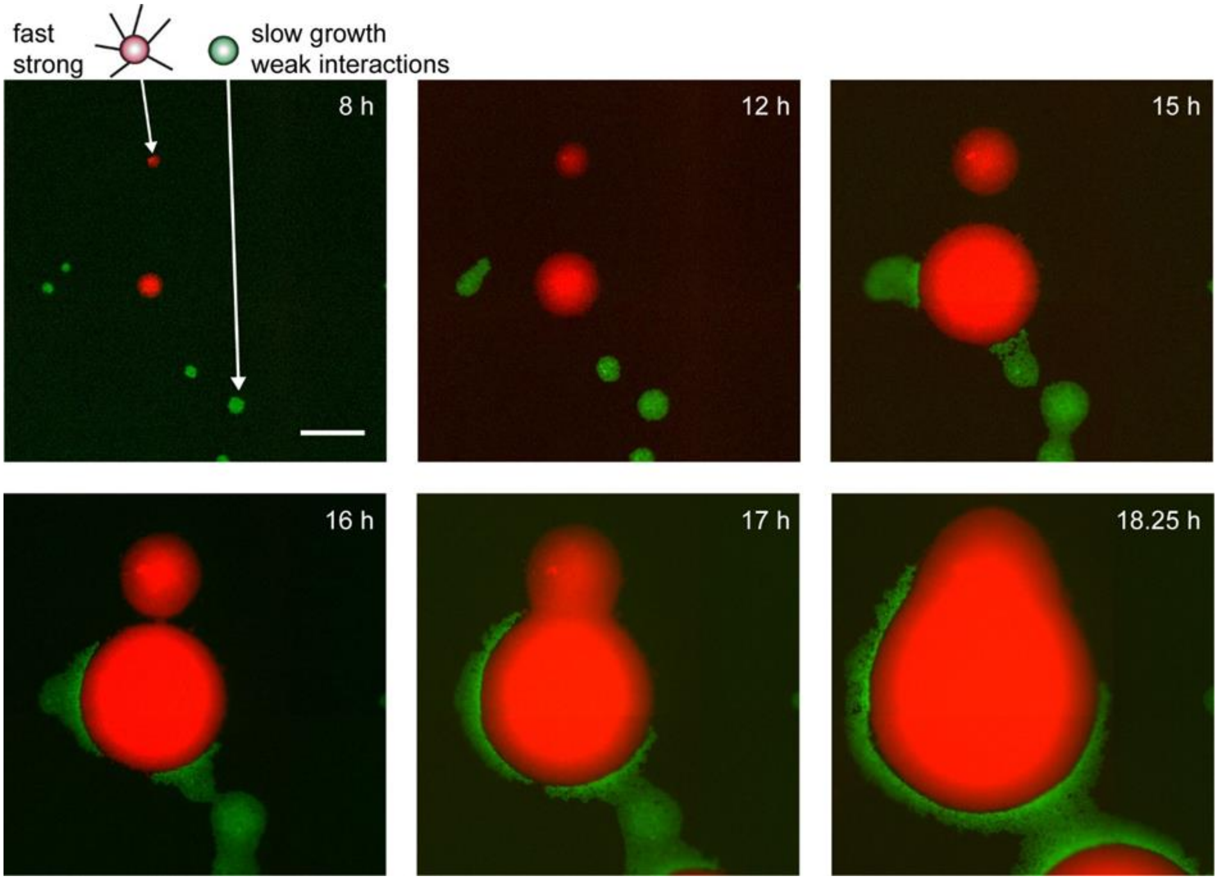

Figure 50: During exponential phase, slowly growing non-piliated bacteria surf on the front of a fast growing piliated colony. Time lapse of expanding colonies formed by slowly growing/weakly interacting $green^Q$ *ermC*– (Ng118) and fast growing/strongly interacting *red ermC*+ (Ng065) grown on 4 µg/ml erythromycin. $r_t = t_{gen}(green^Q\ ermC-)/t_{gen}(red\ ermC+) = 1.9$. Brightness and contrast were adjusted differently for each image. Scale bar: 100 µm. Adapted from [79].

5.4.2 Unpiliated cells dominate the front of expanding colonies even if their growth rate is decreased

It was demonstrated that weakly interacting cells are able to surf on the front of expanding colonies that consist of strongly interacting cells. This pattern is independent of different exponential growth rates. As a consequence of this result, we hypothesized that weakly interacting cells, that are able to maintain their outermost position should gain a fitness advantage because of access to fresh nutrients and unlimited space for growth.

To investigate this hypothesis, $green^Q$ *ermC*- and *red ermC*+ were inoculated at different ratios $r_i = [green^Q\ ermC-]/[red\ ermC+]$ and various concentrations of erythromycin leading to various $r_t = t_{gen}(green^Q\ ermC-)/t_{gen}(red\ ermC+)$ (Figure 54). For convenience, the results will be presented on the basis of the representative condition $r_i = 10$.

Similar to the observed surfing pattern, strongly interacting red cells form round patches that are encapsulated by weakly interacting green cells within the inoculation zone (Figure 51). After ~3 d the outgrowth is dominated by weakly interacting green cells. To test whether the domination of the outgrowth confers a fitness advantage for weakly interacting cells, green and red fluorescent cells within dilutions of entire colonies at $t = 0$ d, 1 d, 2d, 3 d, $r_i = 10$ and $r_t = 1.9$ were counted via fluorescence microscopy. Subsequently the fraction of red cells was calculated. Notably, the fraction of red cells decreased over the first 3 days of growth. This demonstrates that the fitness of green and weakly interacting cells is increased and confirms the hypothesis.

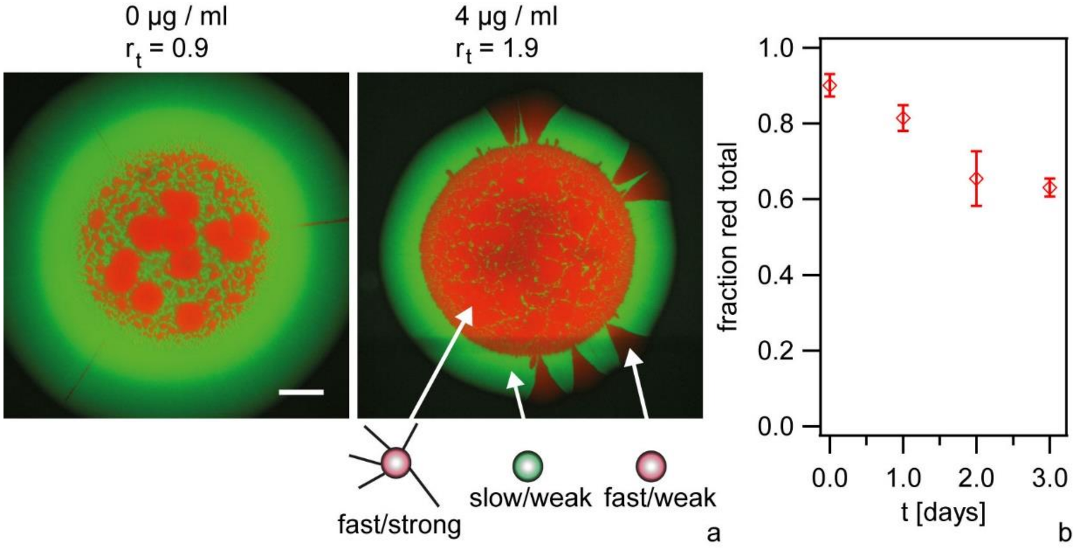

Figure 51: Competition between initially strongly interacting *red ermC*+ (Ng065) and weakly interacting *green*^{Q} *ermC*− (Ng118) cells at varying exponential growth rates. a) Examples of mixed colonies (inoculation ratio r_{in} = [*red ermC*+]/[*green* ^{Q} *ermC*−] = 10) after 68–70 h at varying concentrations of antibiotics. $r_t = t_{gen}$ (*green* ^{Q} *ermC*−)/t_{gen} (*red ermC*+). Scale bar: 500 µm. b) Fraction of *red ermC*+ within entire colony as a function of time obtained from single cell counts of red and green fluorescing cells. $r_{in} = 10$, $r_t = 1.9$. Error bars: Standard deviations obtained from three independent experiments, N > 100 cells for each time point and independent experiment. Adapted from [79].

Surprisingly, red sectors occur within the outgrowth. We suspected that these sectors consist of weakly interacting red cells, that had switched from the piliated/strongly interacting to the unpiliated/weakly interacting state via mutations. The number of sectors was independent of growth rate differences, which are characterized by r_t (Figure 53).

Furthermore, the number of sectors is dependent on the inoculation ratio r_i. This is consistent to the expectation of a mutational transition between piliated and unpiliated state. Immunofluorescence against pili confirmed that the observed red sectors were in deed unpiliated and weakly interacting (Figure 52).

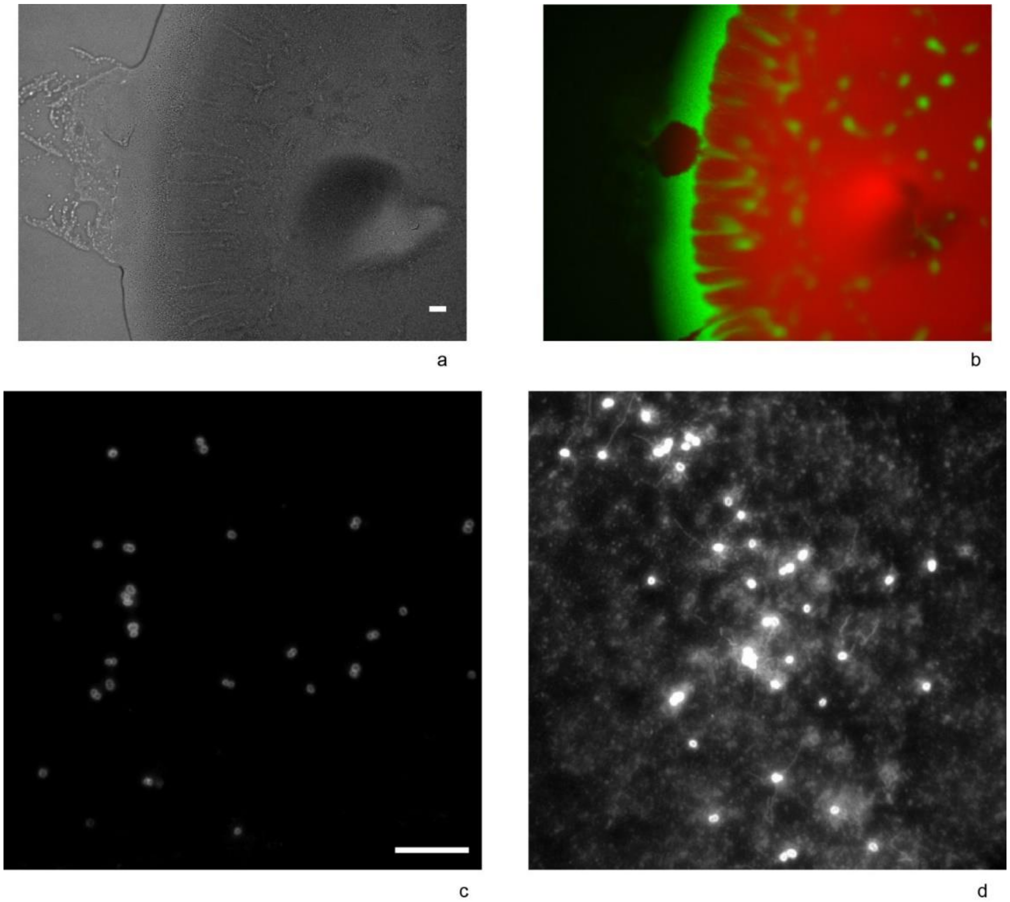

Figure 52: Status of piliation in inoculation zone and in the area of outgrowth in the presence of erythromycin. Piliated *red ermC+* (Ng065) and *green^Q ermC-* (Ng118) were inoculated at a ratio of 1 to 10 on 4 µg/ml erythromycin. Bacteria were picked from the area of outgrowth (a, b) or from the inoculation zone, grown overnight and selected for red fluorescence. Subsequently, bacteria were immobilized on glass cover slide and stained using immunofluorescence with a primary antibody against PilE. c) Area of outgrowth, d) inoculation zone. Scale bars: 50 µm. Adapted from [79].

As a control for stable growth rate differences, the area fractions of the weakly interacting red cells within the green outgrowth were quantified. The area fractions of the red sectors increase as a function of distance to the inoculation zone, which is a measure of time in this case (Figure 54). This is consistent to the expected fitness advantage of weakly interacting red cells (*ermC+*) against weakly interacting green cells (*ermC-*) at $r_t > 0$. Notably, colonies that were inoculated at $r_i = 1$ and $r_i = 10$ were still dominated by weakly interacting green cells after three days of competition despite a severe reduction in growth rate (Figure 54).

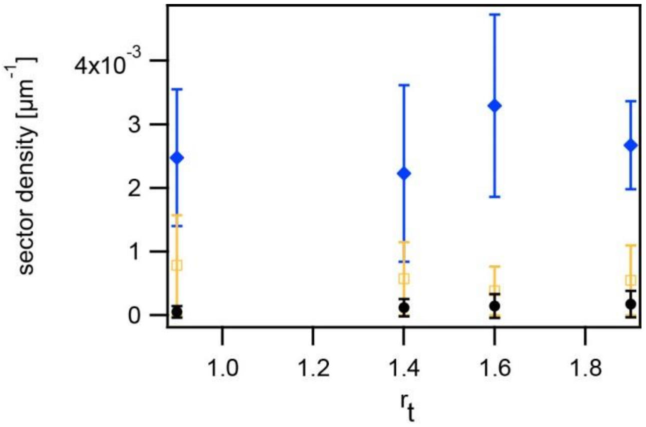

Figure 53: Sector density for competition between initially strongly interacting *red ermC+ recA*$_{ind}$ (Ng065) and weakly interacting *green*^{Q} *ermC- recA*$_{ind}$ (Ng118) cells at varying exponential growth rates. The number of sectors formed by *red ermC+* that reached the expanding front after (68 - 70) h was normalized to the circumference of the front. Ratio of generation times $r_t = t_{gen}(green^Q\ ermC-)/t_{gen}(red\ ermC+)$. Inoculation ratios between *red ermC+* and *green*^{Q} *ermC-* were black circles: r_{in}= 1, orange squares: r_{in}= 10, blue diamonds: r_{in}= 100. The error bars are the standard deviations obtained from 16 macrocolonies for each condition. Adapted from [79].

In summary, weakly interacting cells dominate the outgrowth of expanding colonies. This positional effect is based the state of piliation/interaction and strong enough to compensate severely reduced growth rates. Mutational transitions from piliated to the unpiliated state cause sector formation in expanding biofilms and confer genotypic heterogeneity cells in the outgrowth.

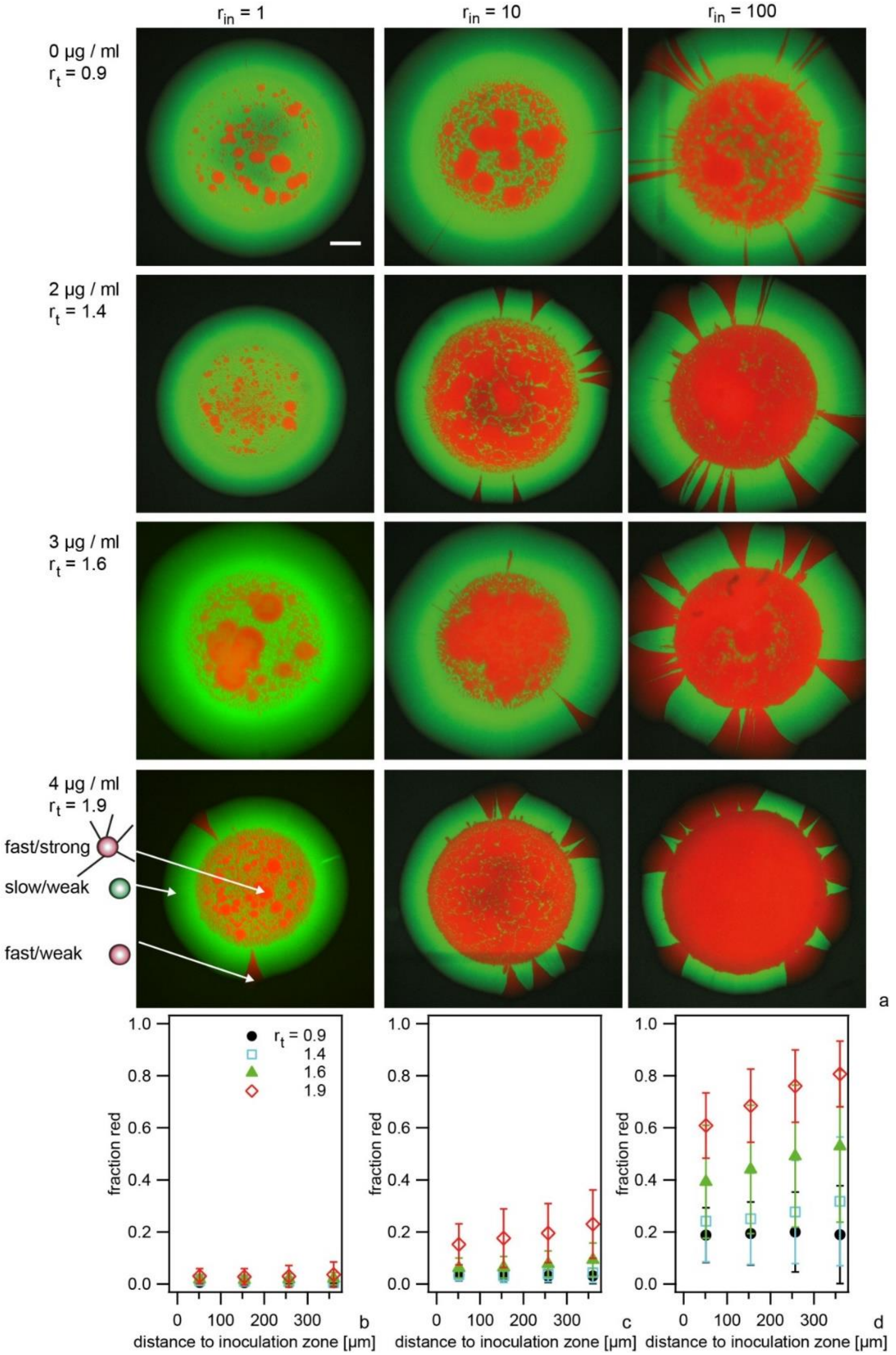

Figure 54: Competition between initially strongly interacting and weakly interacting cells at varying exponential growth rates. a) Examples of mixed macrocolonies after 68 - 70h at varying concentrations of antibiotics. The ratio r_{in} on top indicates the ratio between *red ermC+* (Ng065) and *green^Q ermC-* (Ng118) inoculated onto the agar plate. $r_t = t_{gen}(green^Q\ ermC-)/t_{gen}(red\ ermC+)$. Scale bar: 500 µm. Fraction of *red ermC+* cells within expanding front as a function of distance from the inoculum for [*red ermC+*] *:* [*green^Q ermC-*] of b) r_{in}= 1, c) r_{in}= 10, d) r_{in}= 100. The error bars are the standard deviations obtained from 16 macrocolonies for each condition. Adapted from [79].

5.4.3 Naturally occurring unpiliated mutants accumulate in the expanding outgrowth of biofilms and dominate the population

So far, it was demonstrated that unpiliated cells surf on aggregates of strongly interacting piliated cells. In macroscopic biofilms the unpiliated and weakly interacting cells maintain their position in the outgrowth and gain a fitness advantage that excels severely reduced growth rates. Furthermore, mutational transitions from the piliated to the unpiliated state cause sector formation in the unpiliated outgrowth of macroscopic biofilms on agar.

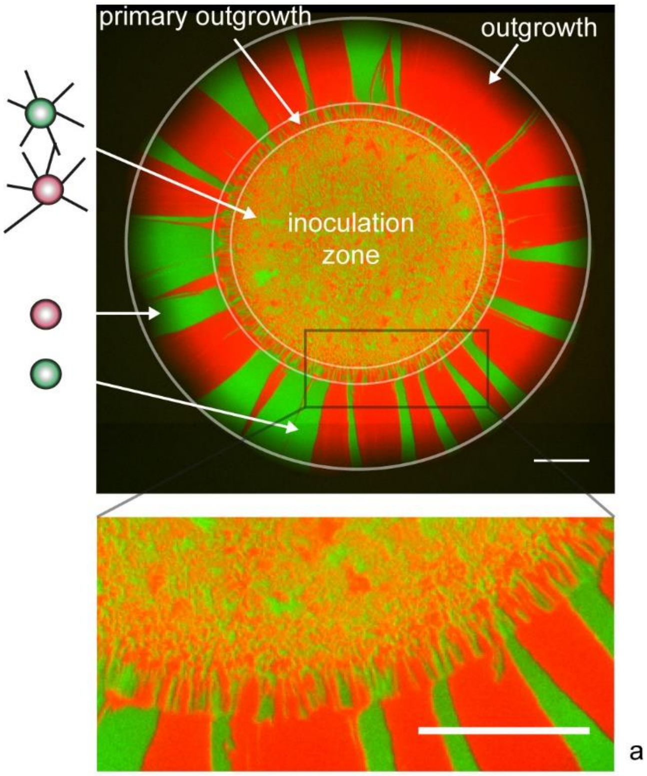

Figure 55: Pattern of *wt* colony. A droplet containing a mix of *wt green* (Ng165) and *wt red* (Ng106) bacteria was applied to an agar plate. a) The colony was imaged using fluorescence microscopy (here after 48 h). Scale bar: 500 µm. b) Cells were picked from the outgrowth and inoculation zone, respectively, diluted in medium and subsequently inoculated onto an agar plate. From the colony morphologies grown on the plate, the fraction of non-piliated cells was determined. N > 150 colonies for each condition. Error bars: standard error from three independent experiments. Adapted from [79].

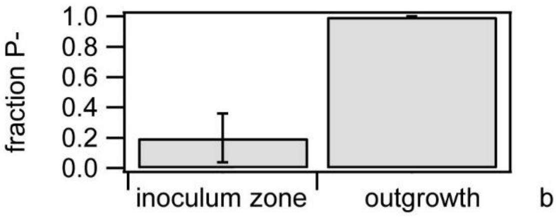

We tested if these findings are consistent to naturally occurring patterns in biofilms. To this end, two piliated wild-type strains (*wt red* and *wt green*) that have red and green fluorescent reporters in non-essential loci were inoculated in a ratio of 1:1 on agar. Both reporters do not affect the growth rate [13]. The resulting macroscopic biofilms were imaged after ~2 days. The biofilm shows specific growth-patterns in sectors that are reminiscent of sector formation in other species [112]. Sectors grow in three specific areas: In the inoculation zone cells show heterogeneous, dense and well mixed structure. In the primary outgrowth cells generated initial sectors. In the (main) outgrowth a sudden change of sector patterning, which is characterized by fewer and larger sectors was observed.

To further investigate the sudden pattern change, time-lapse microscopy was utilized. Growth of macroscopic biofilms including sector formation over ~24 h was imaged. In the first 5 h initial growth in the zone of inoculation could be observed. After ~7 h the zone of inoculation is covered with cells and the primary outgrowth starts to form. After ~7 h growth of the primary outgrowth slows down. Notably, formation of the (main) outgrowth is initiated by segregated, unpiliated and weakly interacting cells after ~7.5 h. These cells appeared to be diffusing in a putative liquid film along the contour of the growing biofilm and dominate the front after ~11 h (Figure 58) [173].

To verify that the outgrowth indeed consists of unpiliated cells two control experiments were performed: First, cells from the outgrowth and the inoculation zone were picked and plated low cell-densities on agar. The resulting colonies were examined and their morphology was categorized into piliated P+ and unpiliated P- [170]. Subsequently, colony forming units (CFU) of each category were counted. Approximately ~20% of the CFU from the inoculation zone and nearly 100% of the CFU from the outgrowth had a unpiliated morphology (Figure 55). Secondly, cells from the outgrowth were picked and categorized into piliated P+ and unpiliated P- colonies. To confirm that this visual categorization is correct, immunofluorescence against the major pilin PilE was done for the selected piliated P+ and unpiliated P- colonies. Pili were distributed around cells that were selected for P+ colony morphology, whereas the number of pili was severely reduced within the P− colonies. The control experiments clearly show that the majority of cells in the outgrowth had lost their pili (Figure 56).

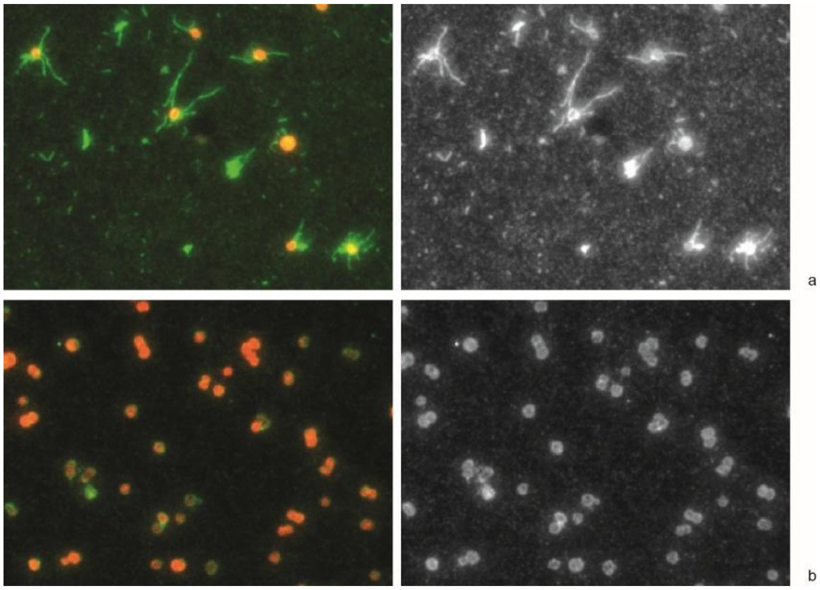

Figure 56: Status of piliation in inoculation zone and in the area of outgrowth. Aggregation of piliated gonococci leads to three-dimensional spherical colonies whereas non-interacting non-piliated gonococci form more flat colonies of larger diameter. To confirm our ability to clearly distinguish between colonies on agar plates of piliated and unpiliated gonococci by visual inspection of colonies on agar plates, we selected individual a) piliated and b) non-piliated colonies (Ng165), immobilized them on a cover slide and stained using immunofluorescence with a primary antibody against PilE. Red: signal from cytoplasmic YFP, green, immunofluorescence detecting PilE. The imaging parameters and the contrast are equal for a) and b). One typical example from three independent experiments is shown. Adapted from [79].

As above-mentioned, unpiliated cells generated by site-directed mutagenesis gain a fitness advantage due to their generic positioning in the outgrowth. To investigate whether this effect is generic for our biofilm model unmodified piliated wild-type cells were inoculated on agar. Over five days the macroscopic biofilms were picked and low cell densities were applied to agar plates. The growing colonies were categorized into piliated P+ and unpiliated P- and CFU were counted. The fraction of piliated cells $f_{P+} = N_{P+}/(N_{P+} + N_{P-})$ was calculated, showing that f_{P+} decreases over the course of five days. The decreasing fraction of piliated cells confirms the fitness advantage of weakly interacting cells in macroscopic biofilms (Figure 57).

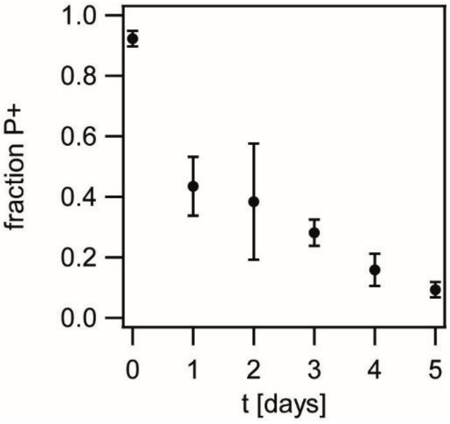

Figure 57: Loss of piliation confers selective advantage. (**a**) Droplets containing *green wt* (Ng165) bacteria were applied to an agar plate. Each day, a colony was suspended in liquid, diluted, and plated. The fraction between CFU with piliated (P+) morphology was determined. Error bars: standard deviation from three independent experiments. Adapted from [79].

In summary, gonococcal biofilms naturally contain a fraction of unpiliated cells. These weakly interacting cells accumulate in the outgrowth of growing biofilms and gain selective advantage.

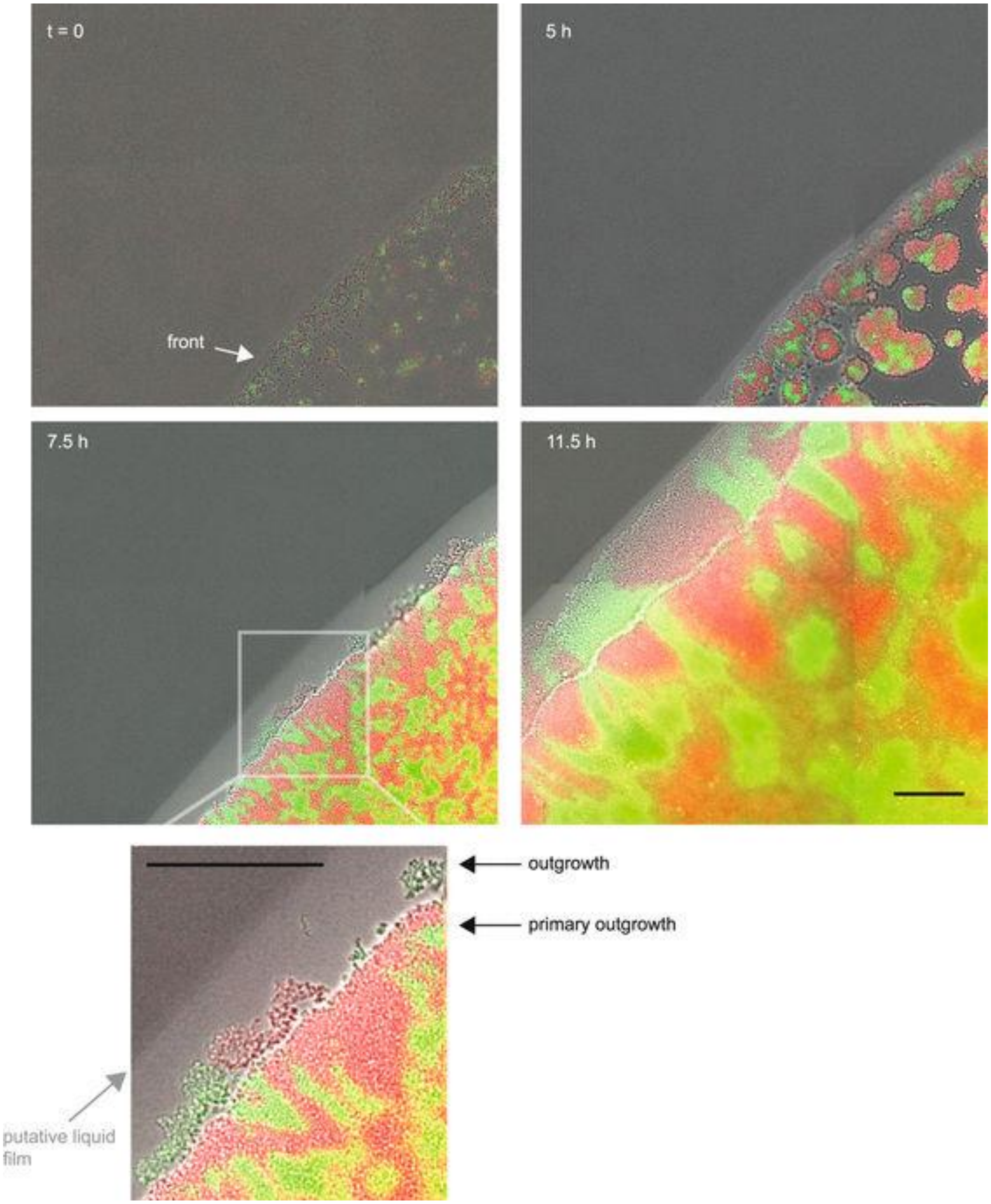

Figure 58: Dynamics of an expanding colony front. Time lapse of growing colony. A droplet of piliated *red wt* (Ng106) and *green wt* (Ng165) was inoculated. Overlay between brightfield image and fluorescence images. Scale bar: 50 µm. Adapted from [79].

5.4.4 Antigenic and phase variation of *pilE* govern the spatial dynamics at the front of macroscopic gonococcal biofilms

Pilus-related genes are subject to antigenic and phase variation in *N. gonorrhoeae* [174]. Both mechanisms can cause transitions from the piliated to the unpiliated state (Figure 9). Following up on the above-mentioned load of unpiliated cells in gonococcal biofilms, we tested whether antigenic and/or phase variation of *pilE* triggered spatial dynamics at the front of macroscopic gonococcal biofilms. To this end unmodified piliated wild-type cells were inoculated on agar. After 48 h of growth cell from the inoculation zone and from the outgrowth were picked and frozen. Subsequently, the major pilin gene *pilE* of clones originating from inoculum (t=0 h), zone of inoculation (t = 48 h) and outgrowth (t = 48 h) was sequenced. Sequence data was aligned and compared. For the sake of convenience, the observed *pilE* sequences were categorized into four the categories 'full length', 'full length, av','truncated, pv' and 'no PCR'. The data was normalized by the total number of sequences from each picking site (Figure 59). 'Full length' covers all sequences that are identical with the most frequent sequence of the inoculum. 'Full length, av' contains all sequences that were similar to the full length sequence, contain mutations that could be mapped to *pilS*-sequences and show no early stop-codon. *pilS* denotes all silent *pilE* sequences in the chromosome that have no proper promoter. 'Truncated, pv' includes all sequences that have a slipped strand mispairing (SSM) mutation in a poly-C-strech that contains eight cytosines. In this case, SSM-mutations denote seven or nine cytosines in the poly-C-strech that result in false codon encryption and premature stop codons. 'No PCR' contains residual data, where the *pilE*-specific primer pair used for amplification and sequencing was unable to produce a PCR product. A likely cause for no PCR product is the deletion of the *pilE* locus [174].

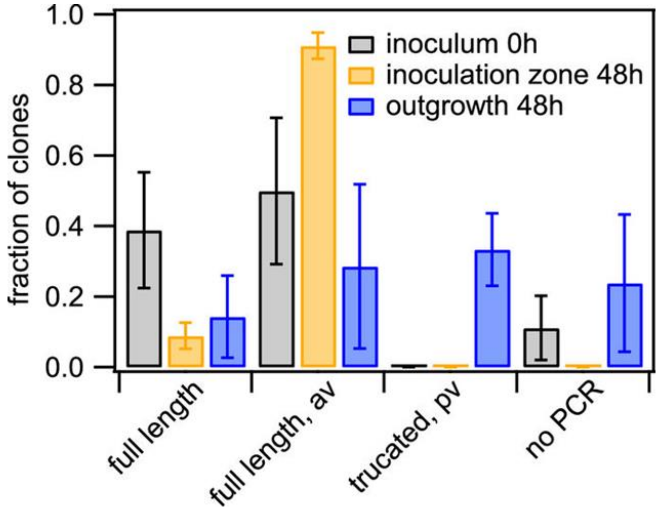

Figure 59: Pilin antigenic and phase variation. *red wt* (Ng106) and *green wt* (Ng165) were picked from the initial inoculum, the inoculation zone (48 h), and the outgrowth (48 h), respectively. After dilution and growth on agar plates, individual colonies (clones) were picked and *pilE* was sequenced. Sequences were categorised and the fraction shown is the number of sequences per category normalised by the total number of sequences of inoculum, inoculation zone and outgrowth, respectively. Full length: most abundant sequence in inoculum; full length, av: sequence change mappable to *pilS* sequence; truncated, pv: length change in poly-C sequence causing premature stop-codon; no PCR: PCR amplification did not result in a product. Mean and standard error of three independent experiments. Adapted from [79].

In *wt*-inoculations that contain *wt red* and *wt green,* two dominating *pilE* sequences were observed that are most likely caused by inoculation of two strains. The inoculation zone after 48h showed several distinct *pilE* sequences. They could be mapped onto *pilS1c1*, *pilS1c4*, *pilS1c5*, *pilS5c1*, *pilS6c1*, and *pilS7c1*, respectively. The observed sequences in the inoculation zone have no indication of a non-functional protein and are consistent to the finding that most CFU are piliated within the inoculation zone (Figure 59). The outgrowth shows a large number of mutations in the *pilE* sequence. A fraction of (0.14 ± 0.10) of the clones showed the ‘full length’ sequence and a fraction of (0.29 ± 0.23) showed ‘full length, av’ *pilE* sequences with mutations that could be mapped onto either *pilS6c3* or *pilS1c1*. Cells that have grown for 48h show a significantly reduced fraction of clones with a ‘full length’ *pilE* sequence. The fraction of clones with a phase variation (‘truncated, pv’) was significantly larger within the outgrowth compared to the zone of inoculation (Figure 59). Altogether, the majority of cells within the outgrowth contains ‘full length, av’ and ‘truncated, pv’ sequences leading to a non-functional *pilE* sequence. Additionally, a large percentage within the outgrowth shows ‘no PCR’ product which is likely to be caused by deletion of the *pilE* locus. These findings are consistent to the finding, that unpiliated cells dominate the outgrowth.

The fact that ‘full length’ clones appear in the outgrowth indicates that *pilE* is not exclusively causing transitions from the piliated to the unpiliated state.

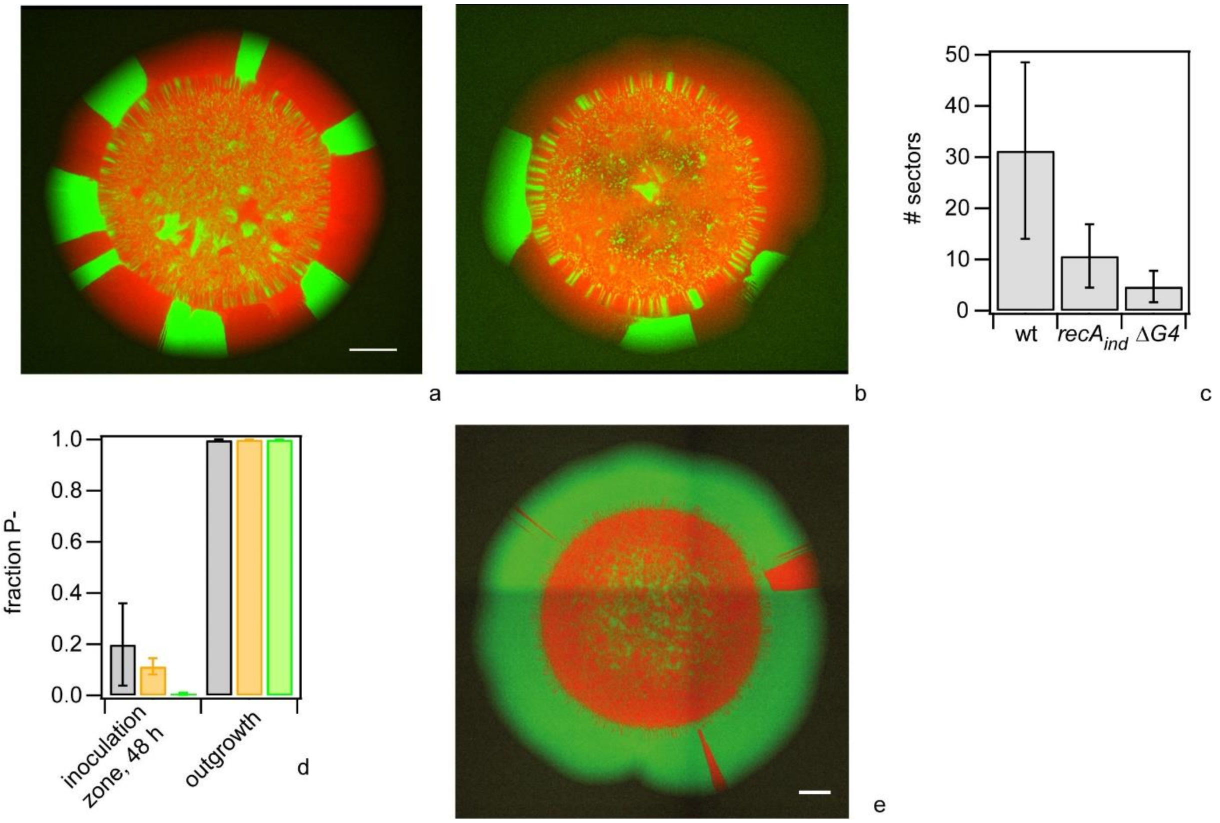

Figure 60: Pilin antigenic variation governs colony dynamics. a),b),e) A droplet of differentially labeled strains was inoculated onto an agar plate and colonies were grown for 48 h. Typical colonies of a) pilin antigenic variation deficient green recA (Ng167) and red recA (Ng168), and b) pilin antigenic variation deficient green ΔG4 (Ng169) and red ΔG4 (Ng170). c) Number of sectors in the area of outgrowth (N > 30 colonies for each condition. Error bars represent standard deviation). Distributions of numbers are significantly different for all pairs with $P < 10^{-4}$ (t-test). d) Fractions of non-piliated cells in 48 h colony determined by colony morphology. Grey: wt, orange: recA$_{ind}$, green: ΔG4. N > 150 colonies for each condition. Mean and standard error from three independent experiments. e) Effect of pilin antigenic variation on competition. A droplet containing a mix of green wt (Ng165) and antigenic variation deficient red ΔG4 (Ng170) bacteria was applied to an agar plate. The colony was imaged using fluorescence microscopy after 48 h. Scale bars: 500 µm. Adapted from [79].

To test the robustness of our findings two background strains that are incapable of antigenic variation were investigated: *recA*$_{ind}$ and *ΔG4.* Both motifs, *recA* and the *G4* motif are essential for pilin antigenic variation [175][147]. The AV-deficient strains were used and experiments that were previously performed with *wt* cells were repeated: Two combinations of piliated AV-deficient strains (*recA*$_{ind}$ *red* and *recA*$_{ind}$ *green, ΔG4*^{red} and *ΔG4*^{green}) were inoculated in a ratio of 1:1 on agar. Macroscopic biofilms were imaged after 48h. Colony morphologies were determined. The fraction of non-pilated cells from the inoculation zone after 48 h was ~11% for $recA_{ind}$ and ~0.6% for *ΔG4* (Figure 60). The inoculation zone of *ΔG4*-biofilms showed a significantly lower fraction of unpiliated cells compared to *wt* and $recA_{ind}$ outgrowths (Figure 60). No piliated cells could be observed in the outgrowth (Figure 60). Additionally, the number of sectors within the outgrowth was decreased for the AV-deficient strains $recA_{ind}$ and *ΔG4* (Figure 60). This is likely to be caused by less frequent transitions from piliated to unpiliated states. The lower density of weakly interacting unpiliated cells in the expanding front of AV-deficient strains translates then into fewer sectors in the outgrowth. This hypothesis is confirmed by our data (Figure 60).

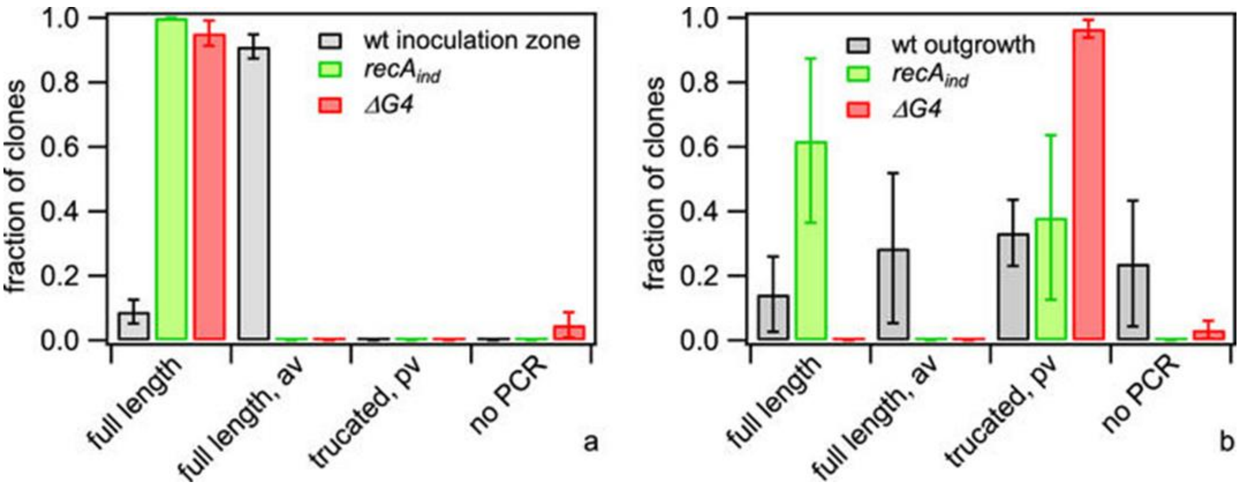

Figure 61: Pilin variation in antigenic variation deficient strains. Cells were picked from a) inoculation zone, and b) outgrowth, respectively. After dilution and growth on agar plates, individual colonies were picked and *pilE* was sequenced. Sequences were categorised and the fraction shown is the number of sequences per category normalised by the total number of sequences found for each strain. Full length: most abundant sequence in inoculum; full length, av: sequence change mappable to *pilS* sequence; truncated, pv: length change in poly-C sequence causing premature stop-codon; no PCR: PCR amplification did not result in a product. Grey: *red wt* (Ng106) and *green wt* (Ng165), green: *green recA* (Ng167) and *red recA* (Ng168), red: *green ΔG4* (Ng169) and *red ΔG4* (Ng170). Mean and standard error of three independent experiments. Adapted from [79].

To test whether variation of *pilE* is involved in generating a mutational load of unpiliated cells in gonococcal $recA_{ind}$ - and *ΔG4*-biofilms, clones that were picked from the inoculum, the inoculation zone and the outgrowth were sequenced. Subsequently the data was again categorized and normalized. Interestingly, no variations in the inocula and the inoculation zones of $recA_{ind}$ and *ΔG4* were observed (Figure 61). The outgrowth $recA_{ind}$ biofilms was dominated by clones carrying the 'full length' parental *pilE* sequence. A fraction of (0.38 ± 0.26) of the clones in the $recA_{ind}$ outgrowth showed pilin phase variation (Figure 61). The fraction of clones that show phase variation within the *ΔG4* outgrowth was (0.97 ± 0.03). This is significantly higher when compared to *wt* or *recA_{ind}* (Figure 61).

In conclusion, antigenic and phase variation of the major pilin gene *pilE* lead to loss of pili and the accumulation of unpiliated cells in the outgrowth of expanding colonies. Inhibition of antigenic variation affects spatial dynamics within the outgrowth of expanding biofilms.

5.5 EVOLUTION OF GONOCOCCI IN LIQUID ENVIRONMENT LEADS TO PELLICLE FORMATION AND INHIBITION OF COLONY FORMATION

This section covers results of an evolution experiment that was performed over 17 days. The main idea was to create an experimental procedure that allows to monitor changes in biofilm mechanics and to correlate them with genomic changes, in particular with mutations in T4P-related genes. Interacting and biofilm-forming cells grow over many generations, followed by a systematic investigation of genomic, mechanical and macroscopic parameters. The experimental procedure was inspired by Poltak et al. [121], where colonized beads were repeatedly transferred into fresh medium, in which new sterile beads could be colonized by the transferred population.

The evolution experiment was done in close collaboration with Tom Cronenberg.

5.5.1 Evolved cells form macroscopic pellicles and structures

The experiment was done with six parallel cultures over ~232 generations assuming ten hours of growth per day (Appendix 8.4). Three of these cultures were treated with H_2O_2 at half MIC (2 mM) in order to investigate whether environmental stress affects the evolution of biofilms [146]. Throughout this section, the six parallel evolved lines are denoted Line1, Line2, Line3, Line1-H_2O_2, Line2-H_2O_2 and Line3-H_2O_2. Line2-H_2O_2 died over the first few days, probably due to the treatment with H_2O_2. Subsequently, the growth chambers of Line2-H_2O_2 were not treated differently and served as contamination control.

In the first days of the experiment no turbidity could be observed. After ~8 days of evolution cells of Line1, Line2 and Line3 grew to a visible optical density. Line1-H_2O_2 and Line3-H_2O_2 showed an increased visible optical density a few days later than the samples receiving no

H_2O_2.

Strikingly, visible pellicles and structures in the growth chambers of Line1, Line2 and Line3, that covered parts of the growth chambers were observed after ~15days. Two days later, macroscopic structures became visible for Line1-H_2O_2 and Line3-H_2O_2. This behavior was known for various swimming biofilm-forming species but has not been observed for gonococci to our knowledge [176]. Importantly, the structures appeared not only at the bottom of the growth chamber but also at the center and the top of the chamber as pellicles (Figure 62). This was surprising because gonococci have no obvious mechanism for swimming or floating to prevent sedimentation to the bottom [160].

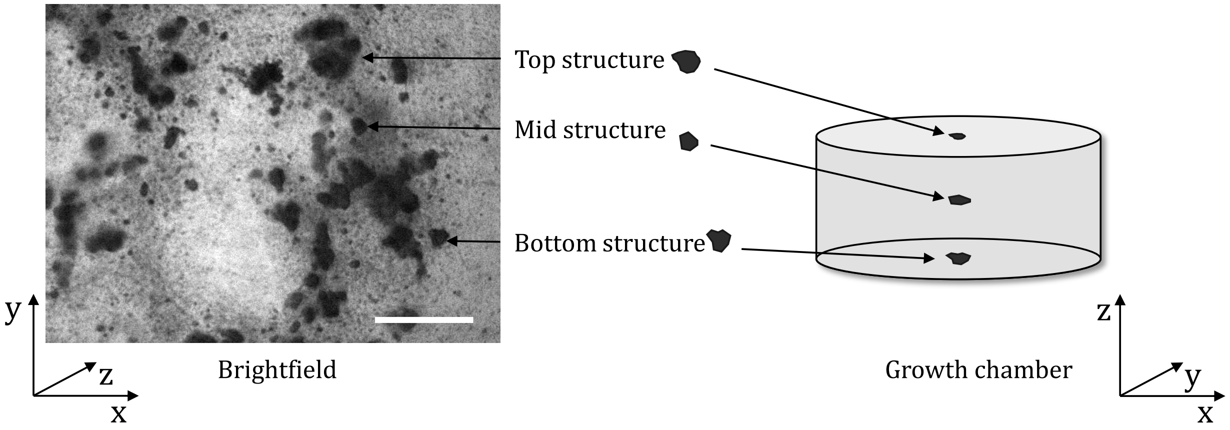

Figure 62: Pellicle and structure formation at the end of 17days of evolution. Brightfield imaging with a 2x objective displays heterogeneous growth patterns in the growth chambers. Mid and top structures were not connected to walls of the chambers. Scale bar: 1 mm.

Pellicles from the top of the growth chambers were picked for further investigation by fluorescence microscopy. The parental strain carried a green fluorescent marker (yfp). Fluorescence microscopy of the pellicles shows that the pellicles consist of cells that inherited yfp (Figure 63). This confirms that the structures were off-spring of the parental strain and not a contamination. Looking closer at the pellicles hotspots that show bright fluorescent signals were detected.

After freezing the cells, we tried to reproduce the formation of structures and pellicles. Unfortunately, the same large-scale structures could not be detected after the freezing step.

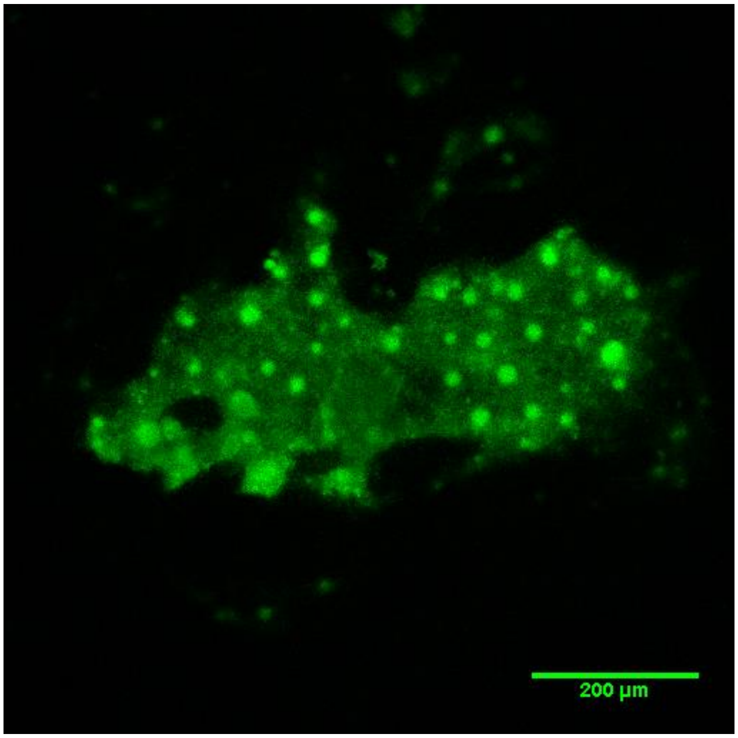

Figure 63: Pellicle formation on day 17. A pellicle was picked including surrounding liquid growth medium. Confocal fluorescence imaging with a 10x objective displays heterogeneous growth patterns within a selected pellicle. Scale bar: 200 µm.

In conclusion, gonococci are able to create structures and pellicles during 17 days of evolution in liquid environment. These structures can float freely within the growth medium. The ability to form macroscopic structures and pellicles is suppressed by the procedure of freezing and unfreezing of cells.

5.5.2 Colony morphology of evolved lines is reminiscent of non-piliated strains on agar

A standard qualitative observable is the colony morphology of cells on agar. The morphology can be used to identify the state of piliation [170]. Typically, colonies that consist of piliated cells are elevated and have a sharp contour, whereas colonies that consist of unpiliated cells show a flat morphology with a fading contour. These characteristics can be observed by eye under a stereo microscope. The evolved lines show a variety of colony morphologies. This was expected because after 17 days of evolution the lines are not clonal. However, the major portion of colonies shows a morphology that is reminiscent of non-piliated cells (Figure 64).

In summary, the morphology on agar of evolved is heterogeneous and a large population fraction is reminiscent of non-piliated cells.

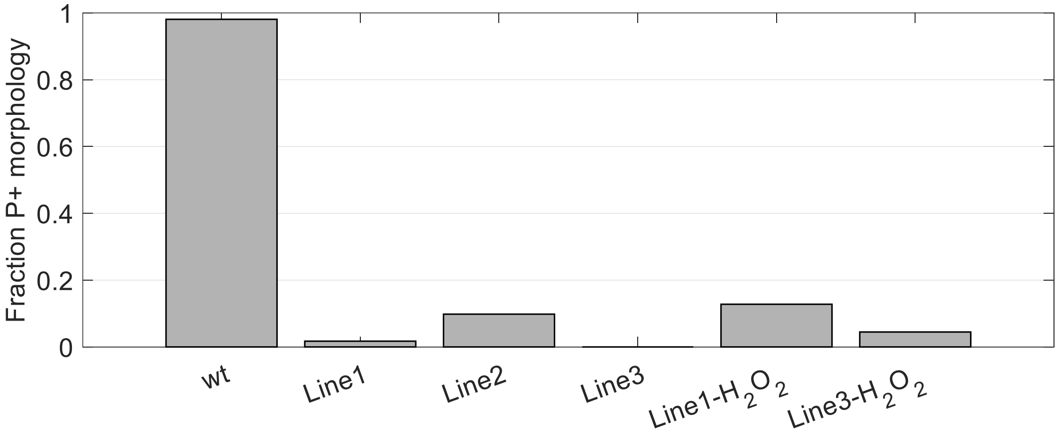

Figure 64: Colony morphology of evolved cells on agar. Single colonies were observed by eye under a stereo microscope and categorized into P+ and P- morphologies. The P+ morphology is marked by sharp contours, whereas P- morphologies are flat and lack sharp contours.

5.5.3 Colony formation is inhibited in liquid environment

A major aim of the evolution study was to characterize how the ability to form colonies evolves over time and to determine physical properties of the evolved biofilms. To this end early colony-shaped biofilms in liquid environment were characterized. These early biofilms are crucial for determination of structure and macroscopic parameters [12][126]. Interestingly, the evolved lines do not form these early colony-shaped biofilms in liquid environment, specifically in flow chambers. Instead of colony shaped clusters, which were found for the ancestor, a disperse distribution was observed (Figure 65). At small scales very small aggregates, which were formed by only a few cells were found for the H_2O_2-Lines. However, these aggregates differed considerably in size when compared to the ancestral strain.

In summary, evolved lines have adjusted intercellular interactions such that the morphology in liquid environment is disperse and not condensed in colonies.

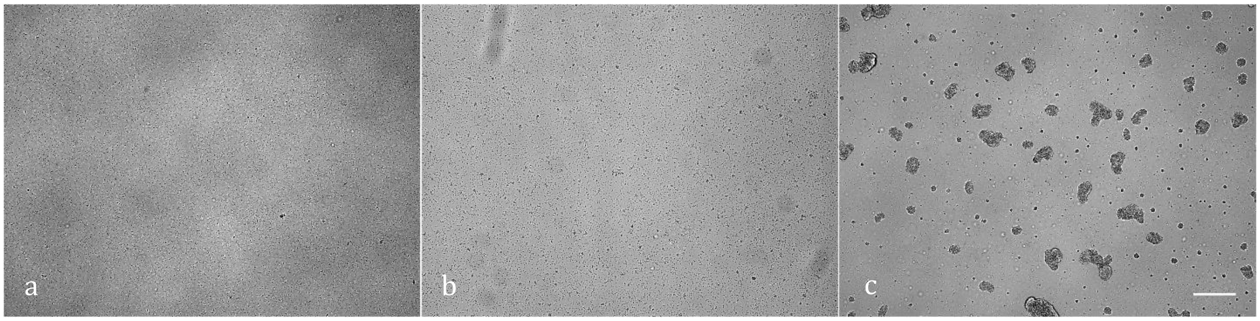

Figure 65: Lack of auto-aggregation of evolved cells within flow chambers. Cells were inoculated by Tom Cronenberg into a flow chamber filled with GC-medium at OD 0.25. No aggregation similar to ancestral cells could be observed for the evolved lines. Examples of Line1 (a) and Line 3-H_2O_2 (b) are shown. c) The ancestral cells showed colony formation. Scale bar: 100 µm.

5.5.4 Evolved lines show twitching motility and prevent sedimentation

In the previous section it was demonstrated that gonococci show a strong phenotypic change after 17 days of evolution. In order to check whether these changes are consequence of loss of piliation, the state of piliation was determined by employing a twitching motility assay. Motile cells are piliated because T4P are essential for twitching motility [125]. For this a small volume of 50 µl was taken from a central position of the evolution chambers. This volume was applied to a cover-slip and directly investigated by brightfield microscopy. Interestingly, over 90% of the cells on the coverslip performed twitching motility. In other words, over 90% of the cells were intact and piliated (Figure 66).

In summary, cells within the evolution chambers are able to dispersedly float in the medium. A large percentage of these floating cells shows T4P-mediated twitching motility. Based on this, we conclude that the inhibited ability to form colony-shaped biofilms in liquid environment is not the result of a lack of pili. Furthermore, we conclude that the colony morphology on agar of evolved not-clonal cells does not represent the state of piliation. This indicates that the evolved lines tuned intercellular interactions such that twitching motility is favored over the ability to form densely packed colonies and biofilms.

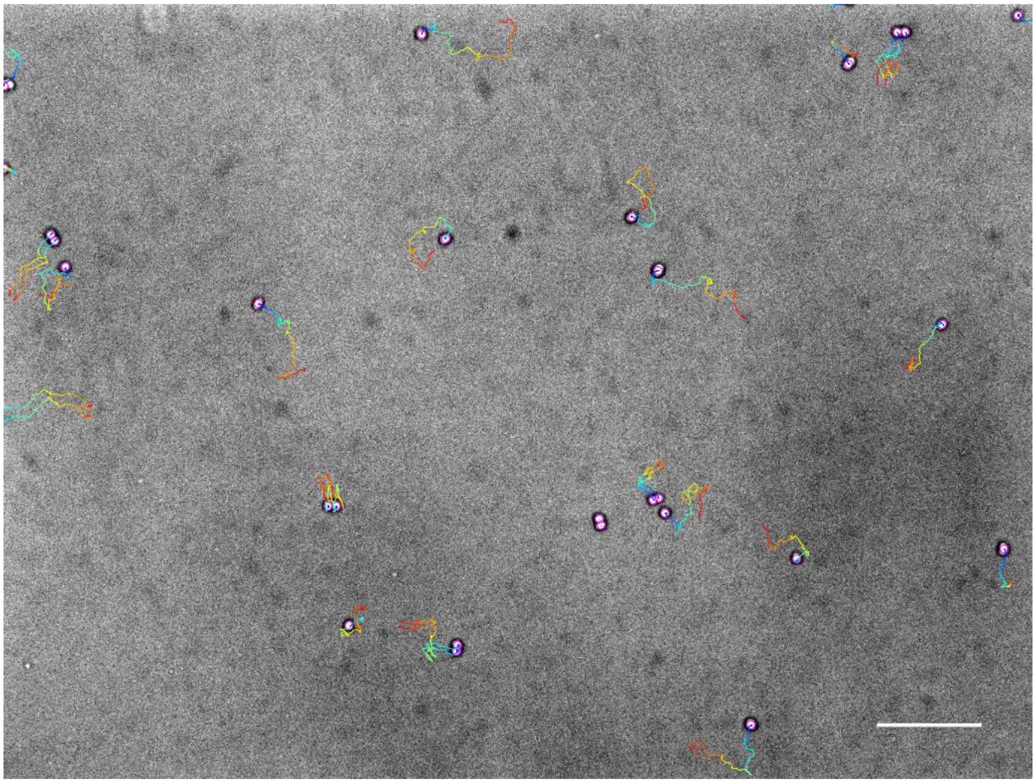

Figure 66: Twitching motility and density of evolved cells. Cells were investigated by brightfield microscopy with a 60x water immersion objective. Small volumes of 50 µl were taken from a central position of the evolution chambers. The volumes were applied to a cover-slip and directly investigated by brightfield microscopy. Cells were tracked over 10 s to visualize mobility. For convenience, tracks were superimposed and time was color coded. Scale bar: 10 µm.

5.5.5 H_2O_2 treatment does not raise the mean number of mutations

In the previous section it was shown that 17 days of evolution in liquid growth chambers with limited nutrients have several phenotypic consequences. Naturally occurring mutations throughout the genome constantly change genetic information. In most cases, mutational changes are connected to evolutionary phenotypic changes [177][178]. In order to link mutational changes of the evolved lines to the observed phenotypic changes, sequence data of the evolved strains had to be compared to the ancestral strain. To this end whole genome sequencing (WGS) was performed on the ancestral and the evolved populations. DNA of well mixed and frozen populations was isolated and sequenced. Consequently, frequencies of specific mutations that were identified in WGS-data are representative for the entire evolved population. The genomic sequence of the ancestral strain was created by aligning reads of the ancestral strain to the annotated genome sequence of FA1090 [179]. It is important to note, that the ancestral population is clonal and produces one reference sequence. Reads of the evolved lines were aligned the ancestral reference sequence. As a result, a list of mutations at specific positions in the chromosome was obtained. For each mutation the population fraction was calculated.

Contrary to our expectations, a lower number of mutations N was found within the populations of Line1-H_2O_2 and Line3-H_2O_2 (Figure 67). The lower number of mutations can be explained by the fact that total number of generations that evolved over 17 days was lower for the H_2O_2-treated lines compared to the untreated lines. The lower number of generations for both H_2O_2-Lines can be deduced by the delayed development of a visual OD and delayed structure formation in the growth chambers.

In summary, mutation rates are unlikely to be increased by application of the stress factor H_2O_2.

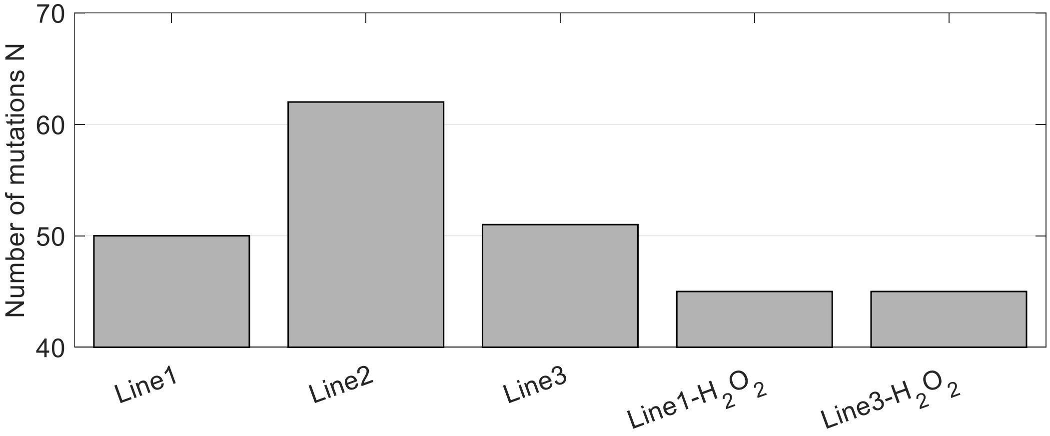

Figure 67: Number of mutations N. The total number of mutations per evolved line was determined by whole genome sequencing.

5.5.6 Genes related to surface structures show mutations

We expected that some of the observed phenotypic changes, such as the putative change of cell-cell interactions are represented as mutations in WGS-data. In order to identify putative connections between geno- and phenotype all 253 mutations appearing within the evolved lines were investigated. All in all, 152 different positions in the chromosome where subject to mutations and had to be identified (Figure 68).

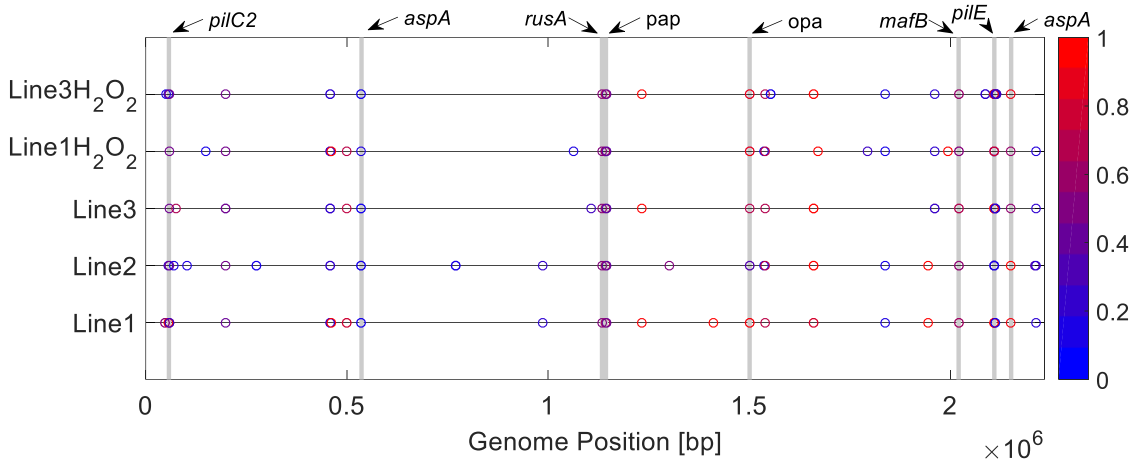

Figure 68: Evolved lines show a total number of 253 mutations. Circles mark all mutations along the chromosomes of the evolved strains. The population fraction is color coded. Eight mutations in *pilC2*, *aspA*, *rusA*, *pap, opa*, *mafB*, *pilE* and *aspA* occurred within all evolved strains and are marked by grey lines.

Overall, 14 of these mutational positions could not be connected to known genes. Importantly, none of these 14 positions show up consistently throughout all 5 evolved lines. Furthermore, no mutation occurs specific to H_2O_2- and no-stress-conditions. This indicates that H_2O_2-conditions do not select specific mutations over 17 days of evolution. The remaining mutations were oftentimes in close proximity and appeared to hit the same gene. Altogether, 20 targets that were affected by mutations could be identified. 8 of these mutational targets show up consistently throughout all 5 evolved lines (Figure 68). These targets were the primary suspects for causing consistently observed disperse phenotype changes among all evolved lines. It has been shown that slight changes of attractive cell-cell interactions have severe consequences for structure and dynamics of cell aggregates [126][87].

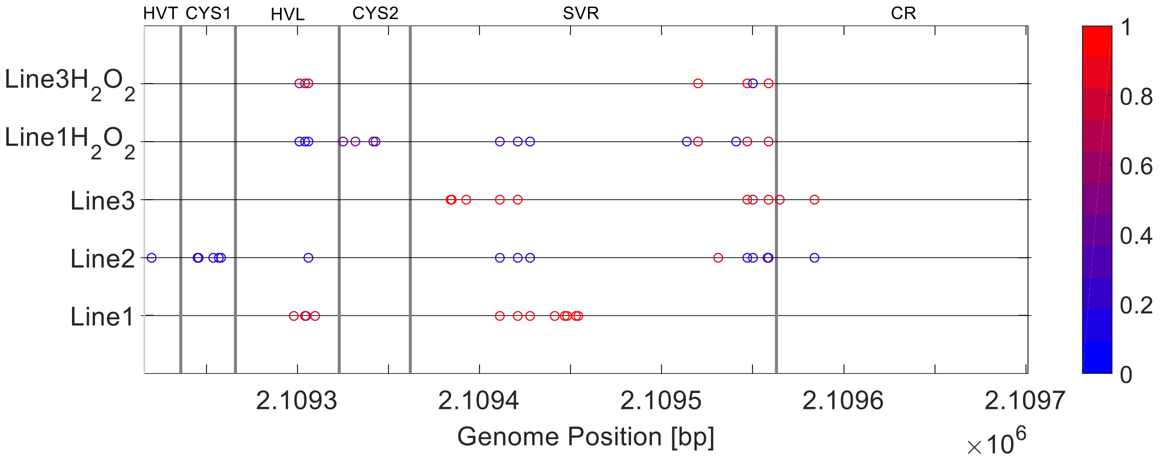

Figure 69: Mutations in *pilE*. Circles mark all *pilE* mutations of the evolved strains. The population fraction is color coded. *pilE* is devided into conserved region (CR), semi-variable region (SVR), cysteine 2 (CYS2), hyper-variable loop (HVL), cysteine 1 (CYS1) and hyper-variable tail (HVT). Boundaries are marked by a grey line. No mutation shows up consistently for all five strains. The population fraction is color coded.

Interestingly, mutations in *pilE* and *pilC2* show up in large fractions throughout all evolved populations. Both genes are directly linked to pilus mediated force generation [46][77]. *pilE* has a minimum of 7 and up to 16 mutations in the evolved populations. None of these mutations occur in consistent positions in *pilE* for all evolved population (Figure 69). The large number of mutations in *pilE* was expected, since *pilE* is a major mutational hotspot due to antigenic variation. Sequence similarities to silent *pilE*-copies *pilS1, pilS7c1* and to L-pilin *pilE1* were observed. If mutations of *pilE* are the cause of observed phenotype, we conclude that there are several mutational pathways in *pilE* that generate a disperse phenotype. Notably, a point mutation in *pilC2* occurs consistently in all evolved line with a fraction of 0.45 ± 0.04 (Table 8).

In conclusion, H_2O_2-conditions are unlikely to increase the mutation rate and do not select specific mutations over 17 days of evolution. Mutations in *pilE* and *pilC2* and other surface-related genes are observed at high fractions and are likely to be linked to the observed disperse morphologies.

Target	Description / Function / Comment	Mean fraction of mutation	NCBI-Reference	Evolved Lines				
				No stress			H_2O_2	
				1	2	3	1	2
pilC2	T4P associated protein	0.60 ± 0.30	CAB05667.1	x	x	x	x	x
pilE	Major pilin of T4P	0.58 ± 0.37	NGO1177	x	x	x	x	x
aspA	Similar to lyase *aspA* in *N. meningitidis*	0.11 ± 0.03	NMO1099	x	x	x	x	x
rusA	Similar to resolvase *rusA* in *N. meningitidis*	0.52 ± 0.01	NMAA1605	x	x	x	x	x
opa	Opacity-associated protein (opa)	0.55 ± 0.41	NGO09965	x	x	x	x	x
pap	Putative phage associated protein (pap)	0.62 ± 0.30	NGO0467	x	x	x	x	x
mafB	Adhesin, polymorphic toxin	0.59 ± 0.06	NGO1971	x	x	x	x	x
fetA	Immunogenic outer membrane protein	0.80 ± 0.20	NGO2093	x	x	x	x	x
pilC1	T4P associated protein	0.26 ± 0.17	NGO0055	-	-	x	x	x
tRNA	Gene for tRNA-Threonine	0.10 ± 0.01	A6J4403405	x	x	-	x	x
Antiporter	Similar to Na^+/H^+-antiporter in *N. meningitidis*	0.09 ± 0.00	NGFG0027	-	-	-	x	-
Transfer-ase	Glycosyl-transferase family A	0.16 ± 0.01	NGO2158	x	x	x	x	-
Ligase	Activates fatty acids by binding to coenzyme A	0.99 ± 0.01	NGO0530	x	-	-	-	x
rRNA	Gene for rRNA-23S ribosomal RNA	1.00 ± 0.00	NGO19006	x	x	-	-	-
pilS7c1	Silent *pilE*-copy	0.12 ± 0.05	X60750.1	-	-	x	-	-
pilQ	Outer membrane pore of T4P-machinery	0.12 ± 0.00	NGO0773	-	x	-	-	-
Peptidase	IgA-specific serine endo-peptidase, autotransporter	0.10 ± 0.02	NGO0275	-	x	-	-	-

Transpos-ase	Transposase IS116 /IS110/IS902 family protein	0.14 ± 0.05	NGO0773	-	x	-	-	-
Phospho-lipase	Phospholipase patatin family protein	0.99 ± 0.00	NGFG01940	-	-	-	x	-
Putative *pilE* copies	Unidentified sequences with similarity to *pilE*	-	-	-	-	x	-	x

Table 8: List of all mutations that were found and identified by WGS.

6 DISCUSSION

6.1 THE DUAL TRAP ASSAY ENABLES CORRELATIONS BETWEEN CELLULAR INTERACTION FORCES AND COLONY DYNAMICS

In this part of the work, interactions on the single cell level were studied. Using dual laser tweezers, interaction kinetics and rupture forces were characterized. The impact of T4P motor activity and pilin post translational modifications on cell-to-cell interaction was investigated. Our results have manifold implications for collective behavior of cellular communities.

6.1.1 Potentials and limitations of the dual trap for characterizing cell-cell interactions

Recently, biophysical tools were employed for characterizing cellular interactions, specifically T4P-mediated interactions. Using a single optical trap, rupture forces between motile cells and pilus-coated surfaces were measured [13]. Further studies used micro pillars or surface attached mobile cells to characterize intercellular interactions [180][12]. In a different set of experiments, atomic force microscopy was used for measuring rupture forces between pili and different abiotic surfaces [181]. However, these techniques exclusively allow for characterizing interaction with cells that were attached to surfaces making these techniques prone to biases related to surfaces. To overcome any surface related measurement errors, we created a dual laser tweezers setup by application of an acousto-optic deflector (AOD). Specifically, two traps were positioned in close proximity to monitor surface-independent interactions of gonococci. The dual trap was highly adept to characterize the kinetics of T4P-T4P attachment, retraction, elongation, and rupture. First, measurements performed with the dual laser tweezers setup revealed that the waiting time distributions between cell-cell and cell-bead interaction events are similar [53]. This finding indicates that there is no evidence for cell-induced T4P force generation and shows that it is unlikely that cells can distinguish between adjacent surfaces and cells. Second, characterizing T4P-T4P interaction kinetics is important for linking T4P-mediated cellular interactions to colony behavior as discussed in chapter 6.1.3. In contrast to simple receptor-ligand binding kinetics, T4P are molecular motors. The dual trap characterized both the motor properties (i.e. T4P retraction) and the kinetics of attachment and detachment. Third, the rupture forces between T4P generated by neighboring cells were addressable. These forces can be linked to cell sorting as discussed in 6.1.3. One drawback of our current setup was that the linear force regime did not extend throughout the entire force range necessary for full characterization of the rupture forces. Increasing the traps stiffness, e.g. by optimizing laser coupling, will be a future challenge. It is important to note that the application of an AOD to manipulate the trapping laser grants a large versatility and enables the generation of more than two trapping potentials in order to capture and align, for example, rod-shaped bacteria or multiple cells. This should allow for characterizing cell-cell interactions of different species and multicellular interactions.

However, concerning dual laser tweezers, there are crucial points that need to be addressed. Currently, the dual laser tweezers lack the ability to perform force-clamp measurements. As a first step towards dual tweezers with force-clamp, we enabled dynamic control of the trapping positions (Section 4.2.3.3). In future experiments, live-tracking of cells can be used to dynamically adjust trapping positions and run the setup in force-clamp mode. We chose trap distance of 2.84 µm. At this distance we observed enough binding events between two cells, while preventing cell-cell-contact. As a consequence, the question how intercellular interactions depends on the radial distance between single cells remains unanswered.

The dual tweezers setup is susceptible to generic biological noise that occurs due to variations in size, shape and composition of the trapped cells. In addition to that, we discovered that cells deform within the tweezers at $\sim$ 35 pN. Typically, deformation studies deal with forces in nanonewton range [145][182]. An additional effect that contributes to systematic measurement biases, is the elasticity of the T4P fiber. Even though T4P can endure forces up to hundreds of piconewtons they stretch up to three-fold [181][64]. The elastic effects affect the shape of rupture distributions, which differed from theoretical predictions [150][183]. However, such predictions generally assume single biomolecule bonds. This assumption is unlikely to be true and the T4P overlap-length and the exact number of bounds between interacting cells remains unknown. The number of bonds is likely to vary and thus contributes to the broad rupture force distributions.

Using AFM and *P. aeruginosa*, rupture forces between T4P and hydrophobic substrates were determined to be in the range of 50 pN up to 250 pN [181]. For our model system broad wild-type rupture force distributions with a maximum at roughly 40 pN were observed. Even though AFM and dual laser tweezers measurements have slightly different geometries, it is interesting to compare rupture force and motor force for *P. aeruginosa* and *N. gonorrhoeae*. *P. aeruginosa* generates motor forces around 40 pN but show rupture forces between 50 pN and 250 pN [27] [181]. This trend is reversed for *N. gonorrhoeae* where the motor force exceeds 100 pN and the rupture forces have a maximum around 40 pN. Hence, *N. gonorrhoeae* is able to perform a tug-of-war mechanism which is unlikely for *P. aeruginosa.*

We conclude that the dual laser tweezers setup is a valuable and versatile tool for characterizing cell-cell interactions.

6.1.2 Motor activity and PTM can be fine-tuned by interaction kinetics

Previously, it was found that different pilin post translational modifications (PTM) have the potential to modify rupture forces, resulting in cell sorting [13]. In this study, the role of pilin PTM and T4P-motor activity on interaction kinetics and forces was investigated by means of dual laser tweezers. Interestingly, variations in pilin PTM and in T4P motor activity affect the probability that two gonococci are bound to each other by T4P-T4P interactions. Interestingly, the kinetics of interactions are affected in different ways.

Changing the status of pilin PTM shifted the rupture force distributions to higher values. Concomitantly, the frequency of T4P-T4P rupture events decreased while the frequency at which T4P retractions occurred was unaffected. Modeling of pilus bundles showed that the average pilus-pilus interaction energy strongly depends on PTM [184]. Based on this, it was suggested that PTM could have important consequences for pilus-pilus interaction [184]. Consistent to these theoretical predictions we observed that PTM change the rupture forces. Specifically, our data indicates that an additional hexose at S63 and lack of phosphoform-modifications at S68 increase the pilus-pilus interaction energy and thus the pilus-pilus rupture forces.

Reducing T4P motor activity, increased elongation rates and decreased rupture and retraction rates consistent to force feedback measurements [126]. Furthermore, increased probabilities to be bound to adjacent cells were observed for motor deficient WB-strains in comparison to wild type-cells. It is tempting to speculate that cells react to environmental changes and dynamically tune their motor activity in order to modulate for example rupture rates. By this, dynamical responses to varying oxygen conditions could be explained [52][185].

In conclusion, both motor activity and PTM fine-tune intercellular interactions. Various species show variable motor activity and a broad range of PTM [186][52][187][188]. It is tempting to speculate that regulating of motor activity and post-translational modifications of surface related structures is a common tool for cells to change adhesion properties.

6.1.3 On the relevance of physical single cell interactions for collective behavior at mesoscopic scale

The strength of interactions on the single cell level affects multicellular arrangements and structure [12][13]. This is not specific to prokaryotic systems. For example, during embryonic development, the strength of intercellular interaction affects spatial arrangement of cells within colonies [189]. Nonliving colloidal systems with attractive interactions form liquid-or crystal-like structures. Interactions in these systems can be controlled by by DNA hybridization or electrostatics [190][191][9]. In this study the kinetics and rupture forces of single cells were characterized and their relevance for physical properties of cell aggregates and biofilms was investigated.

6.1.3.1 Fluid-like behavior in bacterial colonies

We hypothesized that aggregates composed of cells with strong interactions should show a more viscous behavior, whereas weak interactions should lead to less viscous material properties. In this study an important measure for strength of interaction is the probability that two gonococci are bound via T4P. Material properties were quantified by shape relaxation and fusion dynamics [152][153]. Strikingly, the data confirms that high probabilities for cells to be bound lead to high viscosity of even glass-like behavior, whereas low binding probabilities lead to low viscosity. The fact that changes in motor activity (WB-strains) and pilin post translational modification (PTM-strains) have a similar effect on viscosity underscores the universality of the previous statement. We note, that that the fusion assay allowed only for characterization of long-term viscous behavior. However, it is possible that visco-elastic behavior is time-dependent. To characterize this, micro-rheology would have to be applied. In addition to that we note that there are important aspects to the fluid analogy of bacterial communities. We found that the strain *ΔpptA* has increased rupture forces and probabilities for cells to be bound. Interestingly, *ΔpptA* cells showed significantly increased fusion times with colonies that showed a rather edgy, glass-like shape. Hence, it is tempting to speculate that intercellular interactions of *ΔpptA* cells lead to collective behavior close to a transition from liquid-like to glass-like behavior.

In conclusion, our data strongly suggest that changes of intercellular interaction, specifically rupture forces and binding probabilities, determine the fluidity of bacterial colonies.

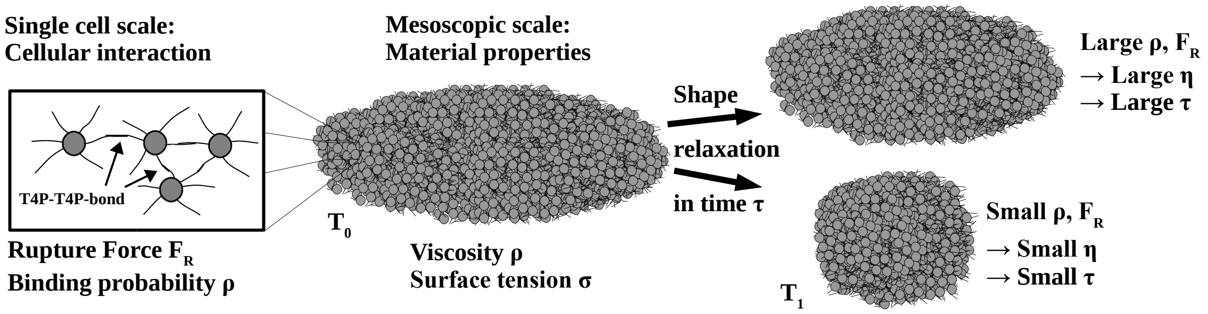

Figure 70: Model representation of how intercellular interaction affects mesoscopic material properties. Single cell interaction mediated by T4P is characterized by specific parameters, e.g. rupture force F_R and binding probability ρ. On the mesoscopic scale material properties can be characterized by viscosity η and surface tension σ. Our data indicate, that large values of F_R and ρ lead to large viscosities η and viscous behavior characterized by long characteristic shape relaxation times τ.

6.1.3.2 Cell sorting

We characterized cell-cell rupture forces for two strains that have altered post-translational modifications (*pglEon* and *ΔpptA*). We found that the rupture force distributions were shifted to higher values. The differential strength of adhesion hypothesis (DSAH) predicts cell sorting within cellular communities based on the strength of interaction and the rupture force, respectively. According to the DSAH, cells that show high rupture force levels will segregate to the center and cells with lower rupture forces will (fully or partially) encase the strongly interacting cells. Strikingly, DSAH-predictions based on measured rupture force distributions were in agreement with observed phase separation patterns for the two PTM-strains when mixed with wild-type cells [107][192]. Furthermore, the segregation patterns were consistent to previous cell sorting experiments with cells that bear PTM-modifications [13]. Still, there are additional factors that may affect the dynamics of cell sorting. In the dual laser tweezers, we detect only events where T4P are retracting and miss interactions that cause no deflection of cells. These interactions like bundling events will likely affect sorting. However, recent simulations of T4P dynamics are consistent with the assumption that T4P either elongate or retract [53] and pausing events occur at low rates. Hence, we conclude that interactions without retraction are rare and add minor contributions to sorting behavior. Interestingly, significantly increased probabilities for cells to be bound were observed for both PTM-strains when compared to wild-type cells, suggesting that differences in these probabilities contribute to phase separation. However, the probabilities were measured at a constant cell-cell distance. It is highly likely that the probabilities are distance dependent and affect the sorting behavior differently if the cell density varies. Furthermore, we have demonstrated that the probabilities for cells to be bound affect collective viscous behavior. Hence, different viscosity-levels of segregating cells may affect the segregation-time-scale.

Altogether, our data on interactions and biofilm formation of PTM-strains strongly suggests, that changing cellular interaction (e.g. by PTM) is a powerful tool to induce cell sorting and phase separation.

6.2 T4P-RETRACTION WITHOUT RETRACTION-ATPASE

In dual laser tweezers force generation of cells without retraction ATPase PilT was observed. Consequently, we undertook first steps towards characterizing the mechanism of *pilT*-independent T4P.

6.2.1 On the mechanism of *pilT*-independent T4P retraction

Force generation by cells lacking the T4P retraction ATPase PilT was observed. Or data strongly suggests that gonococcal T4P are able to retract without retraction ATPase. This is consistent to very recent findings, that report T4P retraction without retraction ATPase in

Vibrio cholerae [155][156]. In these studies, pilus retraction in the absence of retraction ATPase was detected by direct visualization and force generation on micro pillars. For direct visualization pilins were genetically modified and labeled fluorescently. Interestingly, force generation on micro pillars yielded stalling forces that are in the same range as the stalling forces measured in this study [156]. Notably it was demonstrated that *Caulobacter crescentus'* tight adherence (Tad) pili undergo dynamic cycles of retraction and elongation [193]. Interestingly, Tad pili are retractile despite the natural absence of an orthologous retraction ATPase. Thus it is tempting to speculate that pilus retraction in the absence of retraction ATPases is a generic phenomenon among different species.

To get an idea about the mechanism of *pilT*-independent T4P retraction putative other energy sources that may fuel retraction in the absence of PilT were investigated.

First, we tested whether the proteins encoded by the *pilT*-paralogues *pilU* and *pilT2* powered T4P retraction. To this end three deletion strains *ΔpilT ΔpilT2, ΔpilT ΔpilU* and *ΔpilT ΔpilT2 ΔpilU* were created*.* All three strains showed force generation, indicating that different energy sources must be involved. Secondly, we tested whether proton-motive force (PMF) drives *pilT*-independent force generation by T4P. The rationale behind this was based on the fact that PilT driven twitching motility can be slowed down (but not stopped) by depletion of proton motive force [124]. To this end, *ΔpilT* cells were treated with the uncoupler carbonyl cyanidem-chlorophenyl hydrazone (CCCP). The observation of force generation in the absence of PMF indicates that PMF is not the energy source of *pilT*-independent retraction. Third, we assessed whether the periplasmatic PilE-concentration affects *pilT*-independent retraction. Interestingly, a significantly decreased velocity could be observed for PilE-overproducing cells. This effect could be explained by an entropic effect: Consider that PilE bound to the inner membrane is energetically favored in comparison to PilE bound in the pilus fiber. As a consequence, the spontaneous (ATPase-independent) disassembly rate should be larger than the assembly rate. If we now assume for simplicity that the periplasm can only carry a discrete number of PilE proteins in discrete positions, we find that an increasing periplasmatic PilE-concentration decreases the number of unoccupied locations and thus decreases the entropy. As a consequence, the free energy of PilE binding to the membrane increases and the disassembly rate and the retraction velocity decrease. This simple entropic model implies that, energy provided by ATP-hydrolization of the assembly

ATPase PilF can be stored in elongated pili and indirectly fuels PilT-independent retraction. Furthermore, energy provided by PilF is not wasted but efficiently used to perform both elongation and retraction of T4P. Results suggest that PilF evolved prior to PilT because T4P biogenesis has not been observed in the absence of PilF. We speculate that when cells needed to generate higher forces-levels, e.g. for twitching motility or interaction with host cells, PilT has evolved.

6.2.2 Contributions of *pilT* independent retraction to biofilm structure

Structure and order within biofilms are subject to current research. Recently, various biofilm architectures were characterized by confocal microscopy with single cell resolution [126][12][10]. Using the retraction-impaired strains *WB1* and *WB2*, it was discovered that PilT is likely to accelerate ordering of early biofilms [126]. As expected, the local and the global colony structure changed when using ATPase deficient Δ*pilT*-cells (Figure 71). Compared to Δ*G4* and *WB2*, the cell density was lower and the shape of microcolonies formed by Δ*pilT* cells was nonspherical in agreement with previous studies [194][103]. The analytical expression

$$g(r > r_0) = 1 + y^{-m}[g(r_0) - 1 - \lambda] + \left(\frac{y - 1 + \lambda}{y}\right)\exp[-\alpha(y-1)]\cos[\beta(y-1)] \qquad (17)$$

for Lennard-Jones fluids was used to model the radial distribution function g(r) and characterize local liquid like ordering [195]. $r_0 = r/y$ is the contact distance between two bacteria and m, λ, α, and β are adjustable parameters. After 6 h of growth, g(r) showed no evidence for local order within Δ*pilT* cell-aggregates, indicating that PilT-driven T4P retraction accelerated the process of local liquidlike ordering. After 24h of growth, a maximum became in g(r) indicating local order Δ*pilT* cell-aggregates after 24h (Figure 71). Previously this order was related to growing Δ*pilT* cells that occupy free space within the low-density biofilms. Based on the observation of PilT independent retraction in this study we suggest that local ordering of 24h Δ*pilT*-biofilms is not driven exclusively by cell division but may have contributions of PilT-independent T4P-retraction.

In conclusion, early Δ*pilT* -biofilms show local order after 24h of growth and low densities without order after 6h. PilT-independent T4P-retraction is likely to contribute to this dynamical behavior.

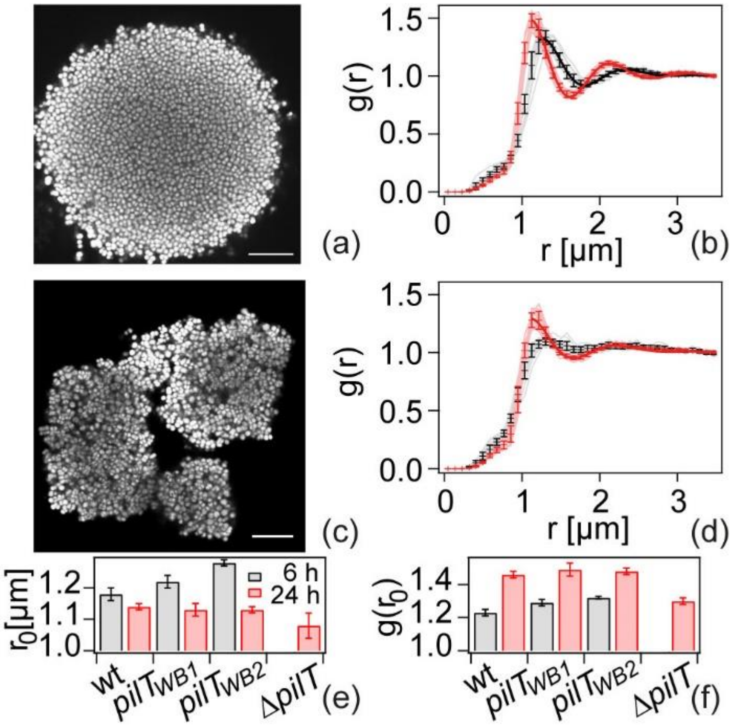

Figure 71: a) Typical confocal section after 6 h and b) radial distribution functions *g(r)* of T4P retraction reduced *WB2* microcolony after 6 h (black) and 24 h (red). c) Typical confocal section after 6 h and d) radial distribution functions *g(r)* of T4P retraction inhibited Δ*pilT* microcolony after 6 h (black) and 24 h (red). Shaded lines: *g(r)* of individual colonies. Full line: fit to eq. (17). Dots and error bars: mean and standard deviation of at least 15 colonies from 3 independent experiments. Scale bar: 10 µm. e) Contact distance r_0 and f) value of radial distribution function at r_0 obtained from fit to eq. (17). Experiments were performed by Anton Welker. Adapted from [126].

6.3 CELL-CELL INTERACTIONS TUNE POSITIONING, HETEROGENEITY AND POPULATION DYNAMICS

In this part of the study, cell sorting based on mutational loss of T4P was investigated. Cells without T4P show weak interaction when compared to piliated cells. We characterized positioning of cells within macroscopic microbial communities and linked our findings to bacterial fitness.

6.3.1 Manipulation of biofilm shape and positioning by switching interaction-strength

Phase and antigenic variation have different functions in microbes. They create genetic heterogeneity and are involved in evading immune response, nutrient acquisitions, motility or gene regulation [196][197][198][199].

In our system pilin antigenic and phase variation (AV and PV) act as switch between the piliated and the non-piliated state. In the piliated state (P+) cells have T4P to actively generate forces, whereas cells in the non-piliated state (P-) show weak interaction. Switching physical interactions from the P+ to the P- state induces cell sorting of weakly interacting P- cells to the front of expanding populations. Spatial sequencing revealed, that pilin AV and PV are important, but not exclusive factors for naturally occurring segregation induced by state switching. We suggest that phase variation of *pilC,* a gene that is essential for T4P generation, is involved in creating a standing fraction of P- cells within a gonococcal population [174][131].

Positioning at the center of a biofilm is considered to help microbes to evade mechanical or chemical stresses. Positioning at the periphery is often related to dispersal and expansion of biofilms. Previous studies have shown that bacteria differentiate depending on the position within biofilms [200]. Our data show that weakly interacting P- cells segregate to the front of growing populations. Notably, cellular automatons were used to successfully model the observed patterns in growing cell-communities based on cell-cell adhesions [201]. A similar positional effect was found for *Pseudomonas fluorescens,* where change of physical interaction favors positioning on the surface of biofilms [202]. Moreover, studies show that mixed populations of bacteria sort according to specific properties affecting T4P dynamics. Specifically, T4P density, post-translational modifications, or retraction competence induce sorting behavior [104][201][13][30].

These cases highlight that microbes have evolved strategies to manipulate their position within cell communities, e.g. by tuning T4P dynamics. Based on our findings, it seems probable, that physical interactions are a common tool to manipulate positioning within microbial communities and initiate dispersal.

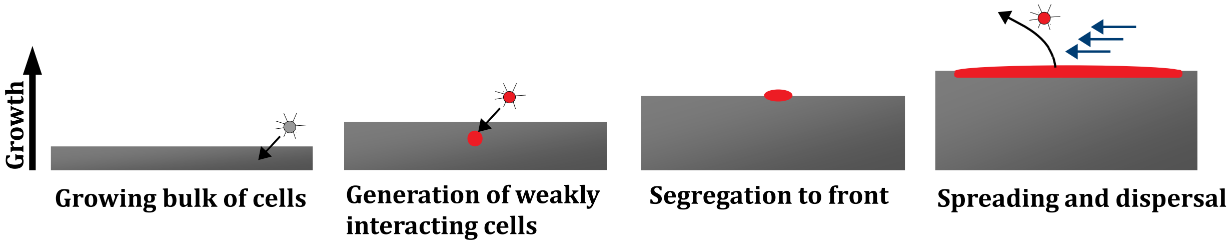

Figure 72: Model of bacterial positioning based on physical cell-cell interactions. Within a growing population (grey) mutations generate weakly interacting cells (red) that segregate to the front. These cells spread along the contour. Weakly interacting cells are subject to dispersal by mechanical flows (blue arrows).

6.3.2 Role of differential physical interactions for growing and evolving biofilms

Positional rearrangement of cells has important implications for selection in structured environments [117]. Cells benefit from exposed positions on the outside of biofilms because of unhindered nutrient supply and unlimited space for growth. However, in the presence of mechanical flow or chemicals, exposed cells have to endure the external stress without protection. Recently it was shown, that strongly adhesive cells accumulate within the biofilm and force less adhesive cells out of the cell-community [203]. This process leads to fitness advantages in case of growth on host cells. In our study a similar mechanism was observed. Switching from the strongly interacting state P+ to the weakly interacting state P- induces sorting of non-piliated (P-) cells to the front of expanding colonies where they show a competitive advantage. Strikingly, the fitness advantage induced by change of physical interactions is strong enough to compensate for severely decreased exponential growth rates. In general, our findings indicate that physical interactions on the single cell level can have direct and drastic consequences for competition in microbial communities.

Consistent with our results, simulations predicted that deleterious mutations are able to accumulate in the front of growing communities in abundance [204][205]. Our result showing that cells with severely decreased exponential growth rates accumulate on the outside of the expanding populations raises the question, to what extend deleterious mutations accumulate within the front and dispersed communities. However, in wild-type range expansions a variety of pilin-variants segregate to the front. This highlights that AV and likely pilin PTM create a standing variation of weakly interacting genotypes that counteract homogeneity induced by genetic drift of the outermost locally small populations.

In natural environments the presence of mechanical flows drives dispersal of the weakly aggregated cells in the periphery of cell communities. Hence, we conclude that tuning of cell-cell interaction to lower levels is connected to dispersal in biofilms. Here, weakly interacting cells residing at the periphery of a colony showed genotypic variability. Dispersal of these cells by fluid flow may ensure diversity during colonization.

In summary, our data suggest that weakly interacting cells segregate to the front of growing communities and gain competitive advantage in structured environments. These cells likely serve the cellular community through dispersal by mechanical flows or by protecting the innermost cells in case of environmental stresses.

6.4 TOWARDS UNDERSTANDING HOW PHYSICAL INTERACTIONS EVOLVE

In the course of this study an evolution experiment that connects evolution to interaction on the single cell level was performed. Our findings suggest that cell-cell interactions may be targeted by multiple mutational pathways.

6.4.1 Gonococci form pellicle-like biofilms after several days of growth

So far, most laboratory evolution experiments have been carried out in liquid culture. The famous long-term evolution experiment of Lenski et al. has started in 1988 and reached over 60,000 generations [206][207]. After 31,500 generations they found newly acquired metabolic traits that could allow for defining a new sub-species [208][209]. Recent studies aim to predicting evolutionary processes and focus on sequence data acquired with high temporal resolution [178][210][211][212]. In contrast to laboratory strains of *E. coli* used in most of these studies, *N. gonorrhoeae* lives at surfaces. To study biofilm evolution and in particular the role of T4P we followed the experimental approach of Poltak and Cooper [121]. Glass beads that were in contact to a growing population were transferred to fresh medium were transferred cells colonized new sterile beads. After 17 days of repeated bead transfer and evolution severe phenotypic changes were observed.

We found macroscopic structures and pellicles within the growth chambers. Pellicle formation is common for several species, such as *B. subtilis* or *P. aeruginosa* [213][214], but was not described for *N. gonorrhoeae* [215]. Interestingly, pellicle formation is associated with aerotaxis [176]. In our pellicles, local hotspots that show bright fluorescent signals were observed. These hotspots indicate localized cell-growth of subpopulations. This pattern is reminiscent of similar patterns in biofilms with heterogeneous growth or division of labor [216][217]. Fluorescent signals could also be detected for the structures within the medium, confirming that they were aggregates of off-spring cells. These structures were not connected to the walls of the chamber and seemed stable in z-direction, indicating that some mechanism transported the cells and prevented sedimentation.

When cells within small volumes were picked from the center of the growth chambers ~ 90 % of the cells within these volumes performed twitching motility. Twitching motility proves that cells have not lost their T4P and are still able to interact actively with adjacent cells and surfaces.

Based on the findings, we propose a possible explanation for the observed facts: The growth chambers are subject to evaporation. Experimentally, an evaporation rate of (4.5 ± 1.3) µg/h per well was determined. As a consequence of the evaporation of medium, the upper layers are constantly cooled. The result is a temperature gradient that induces thermal convection from the warmer bottom to the cooler top of the chambers. It is likely that the generated flux transports cells from the bottom to upper layers and eventually the gas-liquid interface where they stick and induce pellicle formation. A convection flow velocity in the order of the sedimentation velocity would lead to no net velocity and explain the static structures and floating cells within the growth chambers. It is tempting to speculate that the cells increase their viscous drag by T4P production and disperse arrangements, to efficiently use the putative convective transport. Using bright-field microscopy several sedimented cell layers on the bottom of the chambers were observed. Since these cells metabolize CO_2 and O_2, we expect a gradient of CO_2 and O_2 from top to bottom of the chamber. To exploit high concentrations of CO_2 and O_2 cells were forced to grow along the z-axis and form pellicles.

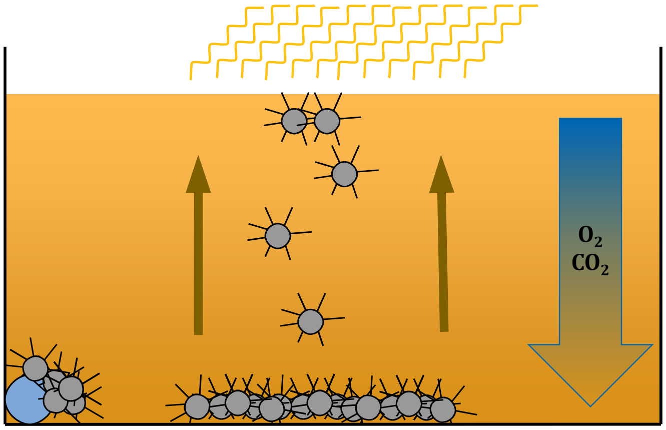

Figure 73: Hypothesis of cell transport within the growth chambers. Cells were inoculated with beads (blue). The growing population has evolved to favor dispersed cells over dense aggregates. Evaporation at the gas-liquid interface cools the upper layer of the liquid medium and induces thermal convection. Dispersed cells use convection streams to reach higher levels. A CO_2 and O_2 concentration gradient imposes selective environment that favors cell-division in upper levels of the growth chamber.

6.4.2 Cell-cell interactions change towards disperse arrangements

Importantly, pellicle and structure formation described in section 5.5.1 was not reproducible after the procedure of freezing and reculturing of the evolved populations, indicating that the process of structure formation cannot be initiated overnight and relies on direct transfer from growth chamber to growth chamber via glass beads. Further investigation of evolved populations within growth chambers revealed that the evolved lines had lost their ability to aggregate and form spherical microcolonies. Additionally, colony morphologies on agar were reminiscent of non-piliated cells, indicating impaired dense aggregation. Considering that ~ 90 % of the evolved cells have pili (as seen in the twitching motility assay), we conclude that cells have tuned their intercellular interaction, such that they favor disperse and mobile arrangements over dense packing and auto-aggregation of the ancestors (Figure 65).

6.4.3 Multiple mutational pathways tune physical interactions

We found that 17 days of evolution in liquid growth chambers has several phenotypic consequences. Our findings suggest that intercellular interaction has been modified to favor disperse and mobile arrangements over dense packing and auto-aggregation. WGS [218][219] was used to investigate whether evolved lines show specific mutations that can be related to the observed phenotypic changes following a previously published protocol [128][220]. To this end we compared the sequences of the evolved lines to the ancestral strain. Previously, it was shown that low oxygen concentrations lead to changed T4P-activity, colony disassembly and disperse arrangements [52][185]. Under high oxygen conditions cells auto-aggregate. It seems likely that the dispersal effect contributes to the initial adaption of cells at the bottom of the chambers. However, evolved cells lost their ability to 'react' and auto-aggregate when supplied with oxygen. Hence, we conclude that, rather than quick (possibly regulatory) responses to environmental oxygen concentration, mutations which changed intercellular interaction cause the dispersed phenotype.

Overall 20 mutational targets were identified in the evolved lines. We expected that the observed disperse phenotype is likely to be caused by modified force generation of the T4P-machinery. Indeed, we found mutations in *pilE* and *pilC* within all five samples. Specifically, the data suggests that either a point mutation in *pilC2*, multiple mutations in *pilE* or combinations of both cause the phenotypic effect. The fact that *pilE* has multiple semi- and hypervariable regions complicates the interpretation of the sequence data. Likely, various combinations of SNPs have similar phenotypic effects on microcolony formation. In addition to mutations in T4P related genes, other genes have been observed consistently in all samples. However, these targets, specifically *aspA, rusA*, *opa*, *pap*, *mafB* and *fetA,* are not directly connected to the T4P-machinery or active force generation [221][222][76][223][224]. Interestingly, *opa*, *mafB* and *fetA* are associated with surface structures and may affect colony formation. *fetA* is an iron-regulated outer membrane transporter [224]. *mafB* is associated with toxic activity and competitive advantage [223]. It seems plausible, that the observed mutation in *mafB* confers a selective advantage in the given environment. *opa*-genes were mutated in various loci. It may be possible, that surface exposed phase-variable *opa*-adhesives decrease binding of T4P and affect cell-cell interaction.

We note, that the putative contributions of surface associated genes to cell-cell interactions are small with respect to forces generated by T4P. Hence, the T4P-related mutations in *pilE* and *pilC* are the best candidates for tuning interactions and affecting microcolony formation. It seems likely that combined mutations in *pilE* and *pilC2* cause phenotypic- and morphologic changes.

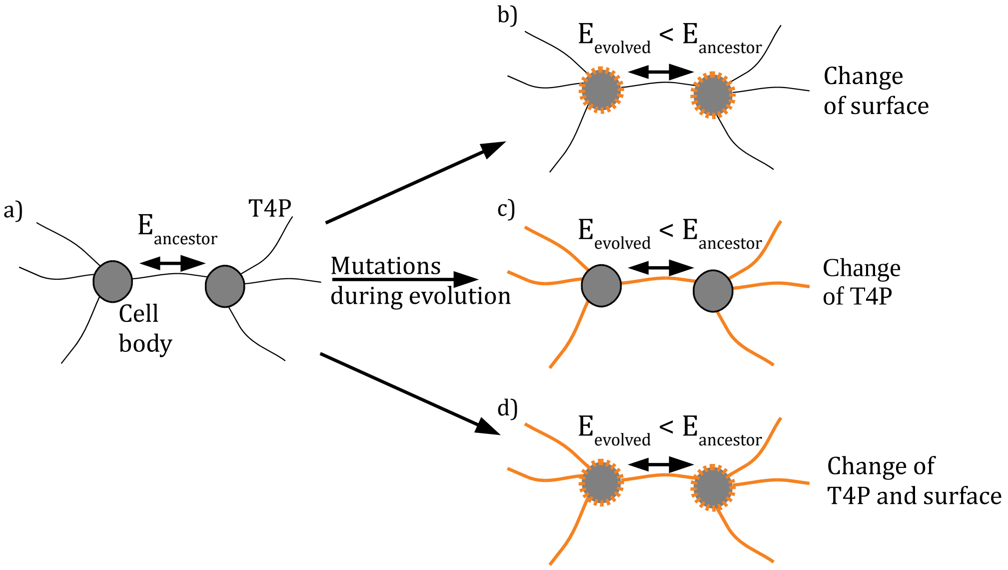

Figure 74: Model of possible structures targeted by mutations that lower T4P-mediated interaction and favor disperse arrangements. T4P are used to bind to adjacent cells and generate forces. Ancestral cells favor dense aggregations and show a T4P mediated cell-cell binding energy $E_{ancestor}$ (a). Based on WGS-data we expect that during evolution, (b) cells changed their surface (e.g. opa-adhesins), (c) their T4P (e.g. *pilE*, *pliC*) or (d) both in order to lower the T4P-mediated binding energy $E_{evolved}$ and favor disperse arrangements.

7 OUTLOOK

7.1 BINDING OF T4P AND CELL MECHANICS

Here, we demonstrated that both motor activity and PTM fine-tune intercellular interaction. However, a detailed view on the binding of T4P remains unclear. It has been shown that T4P co-localize and form bundles [49]. Yet it is unknown, if there is a minimal number of pili involved in bundling, how pili bind to each other and how cells form bundles dynamically. In this study, dual laser tweezers have been developed to investigate T4P mediated single cell interactions. Recently, high speed cameras have been established to characterize single cells and live tracking of particles [225][149]. In combination with high speed imaging dual laser tweezers could be a novel tool to investigate binding of T4P in greater detail. Frequency analysis in Fourier space could provide new information about the number of pili and potentially the number of binding sites. Force dependent measurements could reveal precise levels of binding energies. Furthermore, it was shown that T4P-fibers can be labeled by integration of fluorescent markers [155]. In combination with dual laser tweezers, one could investigate if cellular interaction is mediated by T4P-T4P-bonds or T4P-cell-surface-bonds.

In addition to characteristic binding kinetics cells dynamically deform within laser tweezers. Since little is known about prokaryotic cell mechanics it is tempting to continue and perform a systematic analysis of cellular deformation in laser tweezers. Recent studies have demonstrated, that (high-speed) holographic imaging contains 3D-information that enabled to deduce information on shape and direction [226][227][228]. Combining holographic imaging with dual laser tweezers could provide a detailed image on cell mechanics and add information to a fundamental elastic description of prokaryotic cells.

7.2 HYDRODYNAMICS OF T4P

We have proposed a model that describes transport of cells within liquid by thermal convection. Typically, movement in liquid is well studied but mainly described for micro swimmers that use flagella [229][230]. Apart from flagella driven transport by liquid flows is considered to be the driving force behind biofilm dispersal [230]. However, little is known about the exact properties of passive mechanical transport within liquids. Since biofilms (which are initiated by dispersed cells) are crucial for survival, passive dispersal is likely to be a decisive step that forced cells to evolve specific traits. Results drawn from this study's evolution experiment indicate that T4P are maintained during passive transport in liquid despite their considerable cost [13]. Using laser tweezers, single cells can be trapped and mechanically pulled through liquid. This could reveal, to what extend T4P are able to increase viscous drag. Wild-type measurements in combination with mutants that have reduced numbers of T4P could provide information about hydrodynamics of T4P and their relevance for biofilm dispersal. Following the approach of Ellison et al., fluorescently labeled T4P could reveal dynamical responses to artificial flow conditions [155].

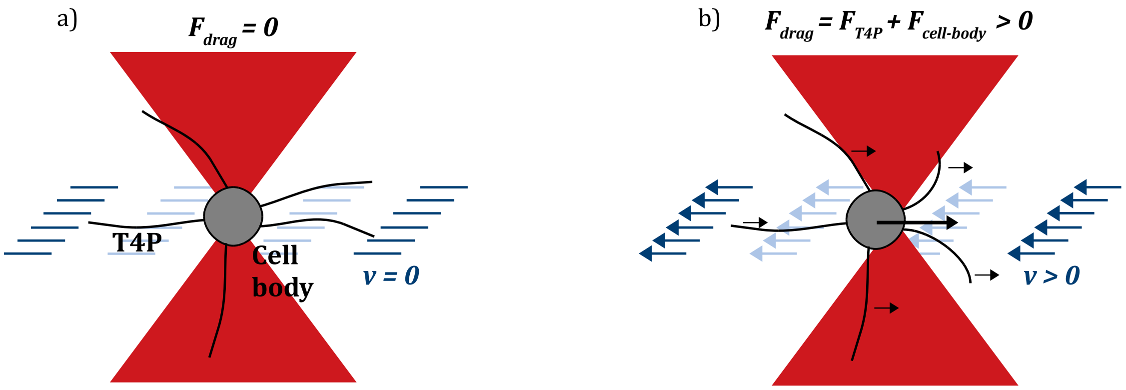

Figure 75: Experimental design to characterize hydrodynamic drag of T4P. a) In the absence of flow (v = 0) the drag force F_d of cells including T4P is zero. b) In the presence of flow (v > 0) the drag force is the superposition of the drag of T4P and the cell body. Measurements of piliated and unpiliated cells enable to calculate the drag of T4P.

7.3 FINE-TUNING CELL-CELL INTERACTION BY PILC AND PILE

Our experiments hint that evolution in liquid environment favors disperse arrangements mediated by mutations in the T4P-related protein PilC and/or PilE. Both, PilC and PilE have been studied extensively [77][45][231]. However, is remains unclear how mutations of the related genes *pilC1*, *pilC2* and *pilE* affect intercellular interaction and biofilm formation. To this end it would be necessary to create mutant strains that have specific mutations. Site-directed mutations could be inspired by the natural mutations observed in the evolution experiment that was performed in this study. Subsequent characterization of twitching motility, auto-aggregation, shape relaxation and intercellular interaction could provide a deeper understanding to the connection of mutations to interaction on the single cell level and collective behavior.

8 APPENDIX

8.1 ABBREVIATIONS

ADP	Adenosine diphosphate
AFM	Atomic force microscopy
AOD	Acousto-optic deflector
ATP	Adenosine triphosphate
AV	Antigenic variation
CCCP	Carbonyl cyanidem-chlorophenyl hydrazone
CCD	Charge-coupled device
CFU	Colony forming units
DCCD	N,N'-Dicyclohexylcarbodiimide
DNA	Desoxyribonucleic acid
DSAH	Differential strength of adhesion hypothesis
eDNA	Extracellular DNA
EPS	Exopolysaccharides
gfp	Green fluorescent protein
GLMT	Generalized Lorentz-Mie theory
IM	Inner membrane
LMT	Lorentz-Mie theory
mcherry	Red fluorescent protein
MIC	Minimal inhibitory concentration
MM	Micro manager
OD	Optical density
OM	Outer membrane
Opa	Opacity-associated protein
P-	Non-piliated state where gonococci show weak interactions
P+	Piliated state where gonococci show strong interactions
Pap	Phage associated protein
PBS	Phosphate buffered saline
PCR	Polymerase chain reaction
PFA	Paraformaldehyde
PMF	Proton motive force
PMP	Polymethylpentene
PTM	Post-translational modification
PV	Phase variation
QPD	Quadrant photo-diode
RAM	Reaction assay medium
ROI	Region of interest
T4P	Type 4 pilus
WB	Walker B
WGS	Whole genome sequencing
yfp	Yellow fluorescent protein

8.2 GRAPHICAL USER INTERFACE

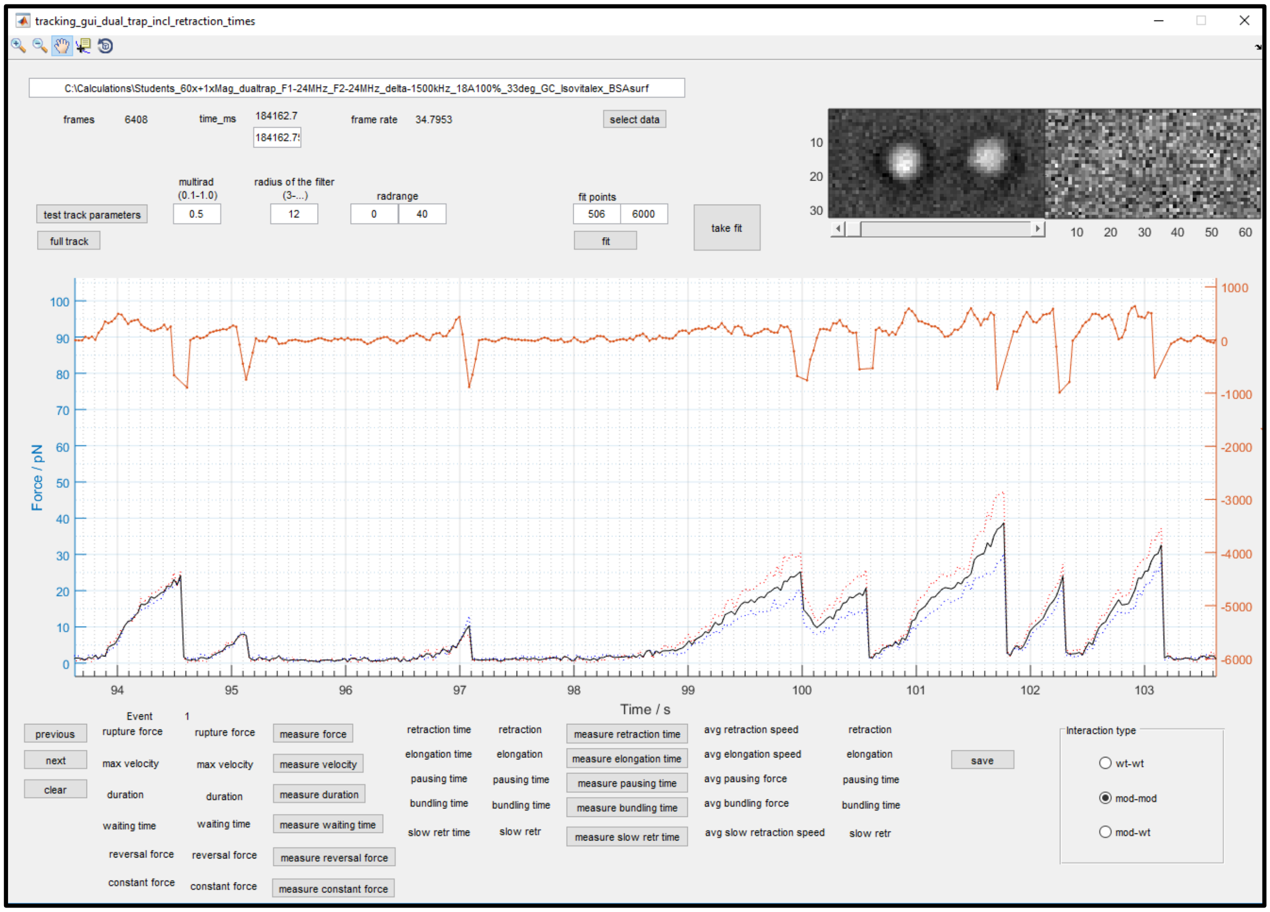
tracking_gui_dual_trap_incl_retraction_times

C:\Calculations\Students_60x+1xMag_dualtrap_F1-24MHz_F2-24MHz_delta-1500kHz_18A100%_33deg_GC_Isovitalex_BSAsurf

frames 6408

time_ms 184162.7

184162.7!

frame rate 34.7953

multirad (0.1-1.0): 0.5

radius of the filter (3-...): 12

radrange: 0 40

fit points: 506 6000

Event 1

Interaction type: ○ wt-wt ● mod-mod ○ mod-wt

Figure 76: Graphical user interface (*tracking_gui_dual_trap.m*). This user interface was used to process raw data.

8.3 LISTS OF MUTATIONS WITHIN EVOLVED POPULATIONS

Line	POS	REF	ALT	Fraction
1	48939	G	T	0,56
1	48955	A	G	0,53
1	55640	T	C	0,99
1	57515	T	C	0,99
1	57516	G	A	0,99
1	57540	C	T	0,93
1	57545	A	G	0,93
1	57626	T	G	0,26
1	57632	T	C	0,53

1	57642	G	A	0,23
1	197854	G	C	0,41
1	458548	T	C	0,48
1	459125	T	G	0,28
1	459271	C	T	0,14
1	461265	GC	G	1,00
1	500732	TC	T	0,88
1	500736	C	G	0,80
1	536442	ACGGG	A	0,12
1	536449	ACGTTGT	A	0,08
1	987328	T	C	0,18
1	1134253	G	C	0,52
1	1144066	C	A	0,63
1	1144862	G	A	0,44
1	1232798	T	TCAGGGCGAAGATGTGGTACAGCGG	0,98
1	1412137	C	A	1,00
1	1501197	A	AG	0,92
1	1501198	A	AGAAGAGAAG	0,96
1	1538696	G	A	0,73
1	1660099	T	C	0,83
1	1660100	T	C	0,83
1	1837103	C	A	0,11
1	1945619	CT	C	1,00
1	2020779	T	C	0,62
1	2020780	G	A	0,63
1	2109298	T	TTTC	0,82
1	2109304	T	C	0,84
1	2109305	G	T	0,82
1	2109310	C	CGGTGGT	0,82
1	2109411	T	C	0,97
1	2109421	T	G	0,97
1	2109428	A	T	1,00
1	2109441	C	G	1,00
1	2109447	A	G	1,00
1	2109448	G	C	1,00
1	2109453	G	T	1,00
1	2109454	T	C	1,00
1	2113072	T	C	0,07
1	2113078	C	CGGTGGT	0,08
1	2151354	C	CGG	0,94
1	2214008	CG	C	0,16
2	56485	G	C	0,23
2	57632	T	C	0,43
2	70170	G	GGAAGA	0,12
2	102048	C	T	0,12
2	197854	G	C	0,46
2	274524	A	T	0,11
2	274526	T	TGGCTAACA	0,09

2	458548	T	C	0,45
2	459125	T	G	0,28
2	459271	C	T	0,18
2	536435	T	TCTTATGC	0,14
2	536442	ACG	A	0,09
2	536445	G	A	0,08
2	770046	C	G	0,19
2	770049	G	A	0,19
2	770125	A	G	0,10
2	770823	C	G	0,10
2	987328	T	C	0,20
2	1134253	G	C	0,52
2	1144066	C	A	0,60
2	1144862	G	A	0,38
2	1301273	CCTTCT	C	0,51
2	1501188	GAGAAGAGAAA	G	0,53
2	1501198	A	G	0,30
2	1538236	A	C	0,14
2	1538696	G	A	0,71
2	1660099	T	C	1,00
2	1660100	T	C	1,00
2	1837103	C	A	0,09
2	1945619	CT	C	1,00
2	2020779	T	C	0,56
2	2020780	G	A	0,56
2	2107876	GC	G	0,08
2	2107880	C	T	0,08
2	2107914	T	A	0,10
2	2107920	G	C	0,11
2	2108825	G	T	0,12
2	2109220	A	G	0,11
2	2109245	T	G	0,12
2	2109246	T	C	0,12
2	2109254	AG	A	0,13
2	2109257	T	A	0,13
2	2109258	GCC	G	0,13
2	2109306	T	G	0,07
2	2109411	T	C	0,25
2	2109421	T	G	0,24
2	2109428	A	T	0,14
2	2109531	C	T	0,86
2	2109547	T	C	0,19
2	2109550	C	T	0,14
2	2109558	T	A	0,37
2	2109559	T	C	0,20
2	2109584	G	A	0,11
2	2109913	G	T	0,24
2	2110102	G	A	0,09
2	2151354	C	CGGGG	0,99
2	2211139	C	CG	0,34

2	2214008	CG	C	0,17
3	57632	T	C	0,44
3	75641	G	GGAAGA	0,68
3	197852	AG	A	0,14
3	197854	G	C	0,48
3	458548	T	C	0,53
3	459125	T	G	0,29
3	459271	C	T	0,17
3	500735	C	G	0,74
3	536436	C	CTTCTGCT	0,17
3	536449	ACGTTGT	A	0,06
3	1106931	T	C	0,25
3	1134253	G	C	0,54
3	1144066	C	A	0,58
3	1144862	G	A	0,34
3	1232999	G	A	1,00
3	1501193	GAGAAA	G	0,70
3	1538696	G	A	0,70
3	1660099	T	C	1,00
3	1660100	T	C	1,00
3	1962193	G	GC	0,51
3	1962206	G	C	0,18
3	2020779	T	C	0,68
3	2020780	G	A	0,69
3	2109384	T	G	1,00
3	2109385	T	C	1,00
3	2109393	T	C	1,00
3	2109411	T	C	1,00
3	2109421	T	G	1,00
3	2109547	T	C	1,00
3	2109550	C	T	0,78
3	2109559	T	C	1,00
3	2109565	G	T	0,86
3	2109584	G	A	0,97
3	2110663	T	G	0,26
3	2110667	G	C	0,26
3	2110672	T	C	0,25
3	2110690	T	C	0,24
3	2110700	T	G	0,25
3	2110720	C	G	0,25
3	2110726	A	G	0,23
3	2110727	G	C	0,23
3	2110732	G	T	0,23
3	2110733	T	C	0,23
3	2113107	G	C	0,06
3	2113111	C	T	0,09
3	2113152	T	G	0,16
3	2113153	T	C	0,16
3	2113161	T	C	0,19
3	2113196	T	A	0,18

3	2151354	C	G,CG	0,56
3	2214008	CG	C	0,18
1 - H2O2	57632	T	C	0,45
1 - H2O2	149107	T	C	0,09
1 - H2O2	197854	G	C	0,45
1 - H2O2	458548	T	C	0,52
1 - H2O2	459125	T	G	0,30
1 - H2O2	459271	C	T	0,16
1 - H2O2	461265	GC	G	1,00
1 - H2O2	500735	C	G	0,72
1 - H2O2	536442	ACGGG	A	0,12
1 - H2O2	1064327	GGAAGA	G	0,11
1 - H2O2	1134253	G	C	0,51
1 - H2O2	1143050	G	A	0,12
1 - H2O2	1143051	C	G	0,15
1 - H2O2	1143055	A	G	0,30
1 - H2O2	1143058	A	G	0,33
1 - H2O2	1144066	C	A	0,65
1 - H2O2	1144862	G	A	0,37
1 - H2O2	1501184	G	GGAAGAGACGAGAAGA	0,01
1 - H2O2	1501198	A	G,AAGAAGAGAAGAGAAG	0,99
1 - H2O2	1538236	A	C	0,14
1 - H2O2	1538696	G	A	0,72
1 - H2O2	1669873	T	TCGTCCGC	1,00
1 - H2O2	1793936	G	GGTCGTTGTTTCTGTCAAGAAACAACGACAGTTTATAAACT	0,23
1 - H2O2	1837103	C	A	0,09
1 - H2O2	1962193	GC	G	0,18
1 - H2O2	1993988	TCGC	T	1,00
1 - H2O2	2020779	T	C	0,51
1 - H2O2	2020780	G	A	0,52
1 - H2O2	2109301	T	TGCCGTC	0,07
1 - H2O2	2109304	T	TGCC	0,10
1 - H2O2	2109306	T	G	0,11
1 - H2O2	2109325	C	T	0,41
1 - H2O2	2109332	GTCT	G	0,40
1 - H2O2	2109342	G	T	0,41
1 - H2O2	2109343	C	T	0,41
1 - H2O2	2109411	T	C	0,32
1 - H2O2	2109421	T	G	0,24
1 - H2O2	2109428	A	T	0,13
1 - H2O2	2109514	T	TG	0,23
1 - H2O2	2109520	G	A	0,79
1 - H2O2	2109541	T	C	0,09
1 - H2O2	2109547	T	C	0,80
1 - H2O2	2109559	T	C	0,81

1 - H2O2	2151354	C	CGGG,CGGGGG	0,59
1 - H2O2	2214008	CG	C	0,14
3 - H2O2	49402	C	T	0,11
3 - H2O2	56485	G	C	0,20
3 - H2O2	57632	T	C	0,44
3 - H2O2	197854	G	C	0,45
3 - H2O2	458548	T	C	0,50
3 - H2O2	459125	T	G	0,25
3 - H2O2	459271	C	T	0,15
3 - H2O2	536442	ACGGG	A	0,14
3 - H2O2	536449	ACGTTGT	A	0,08
3 - H2O2	1134253	G	C	0,53
3 - H2O2	1144066	C	A	0,65
3 - H2O2	1144862	G	A	0,42
3 - H2O2	1232536	A	C	1,00
3 - H2O2	1501184	G	GGAAGAGCAGA	0,00
3 - H2O2	1501198	A	G,AAGAAGAGAAG	0,99
3 - H2O2	1538696	G	A	0,71
3 - H2O2	1553380	A	ACCG	0,08
3 - H2O2	1553381	A	G	0,08
3 - H2O2	1553384	A	ACGACGG	0,09
3 - H2O2	1660099	T	C	1,00
3 - H2O2	1660100	T	C	1,00
3 - H2O2	1837103	C	A	0,10
3 - H2O2	1962193	G	GC	0,17
3 - H2O2	2020779	T	C	0,58
3 - H2O2	2020780	G	A	0,59
3 - H2O2	2087833	T	C	0,23
3 - H2O2	2087840	G	GTCT	0,20
3 - H2O2	2087847	T	G	0,19
3 - H2O2	2087848	T	C	0,19
3 - H2O2	2108996	G	A	0,18
3 - H2O2	2109301	T	TGCCGTC	0,60
3 - H2O2	2109304	T	TGCC	0,71
3 - H2O2	2109306	T	G	0,72
3 - H2O2	2109520	G	A	1,00
3 - H2O2	2109547	T	C	1,00
3 - H2O2	2109550	C	T	0,10
3 - H2O2	2109559	T	C	0,94
3 - H2O2	2113161	T	C	0,13
3 - H2O2	2113164	G	C	0,13
3 - H2O2	2113763	C	G	0,17
3 - H2O2	2113769	T	G	0,20
3 - H2O2	2113770	T	C	0,20
3 - H2O2	2113775	G	T	0,20
3 - H2O2	2113776	T	C	0,20
3 - H2O2	2113869	T	C	0,31
3 - H2O2	2113877	A	T	0,30
3 - H2O2	2113878	T	C	0,29

3 - H2O2	2113903	A	G	0,23
3 - H2O2	2151354	C	CGG,CGGG	0,91

Table 9: List of all genetic changes within the chromosome of all evolved lines.

8.4 EXEMPLARY GROWTH CURVES OF EVOLVED LINES

We tested, whether growth behavior in liquid environment has changed for the evolved lines. To this end, the five evolved lines were inoculated into 1 ml GC in well plates. The optical density (OD600) was measured at 12 distinct positions of each well and then averaged. This was necessary to avoid jumps of the optical density that are induced by clusters and clumps of cells. The temporal resolution was set to $\Delta t = 10$ min. Wells were not shaken at any point in time in order to have similar growth behavior, compared to the evolution experiment. In comparison to parental cells, all evolved lines show slightly faster growth and lower carrying capacities. After a short phase of exponential growth the cells grow linearly until $t \approx 12.5$ h (Figure 77). At $t \approx 12.5$ h and $t \approx 20$ h kinks appear in the optical density. These kinks could be related to various processes such as flocculation, sedimentation or nutrient limitation. However, OD-measurements did not allow for assigning a specific process to the kinks.

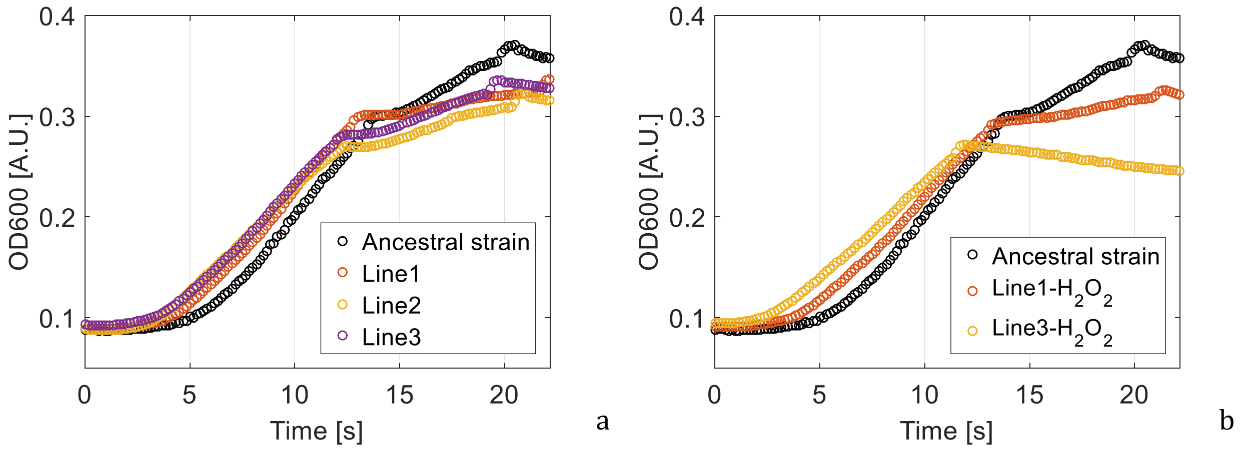

Figure 77: Growth curves of evolved strains. All evolved lines were unfrozen and inoculated at OD = 0.1 into 1 ml GC in well plates. The optical density was measured at 12 positions of each well and averaged. The temporal resolution is $\Delta t = 10$ min. Wells were not shaken at any point in time. a) Growth curves of evolved strains without H_2O_2 treatment. c) Growth curves of evolved strains with H_2O_2 treatment.

8.5 DUAL TRAP VELOCITY MEASUREMENTS OF *PILT*-INDEPENDENT RETRACTION

Based on PilT-driven T4P retraction, it was expected that at some opposing force the velocity should drop to zero. This force is called stalling force F_s. In addition to F_s, a maximum velocity v_{max} was expected. PilT-driven T4P retraction can be described by the empirical formula $v(F) = v_{max}(1 - F/F_s)$, where $v(F)$ is the force dependent velocity. To characterize the molecular motor that is responsible for PilT-independent retraction of T4P, velocities of *ΔpilT* in steeper trapping potentials, at stiffness values of $k_{5\%}{\sim}5$ fN/nm, $k_{7\%}{\sim}7$ fN/nm and $k_{10\%}{\sim}10$ fN/nm were measured in dual laser tweezers. Tuning of the trapping potential was necessary because the dual optical tweezer setup was not equipped with a force feedback mechanism, that allows to keep deflection and restoring forces constant.

At various trap stiffness values, velocities of $v_{5\%} = (6.5 \pm 3.3)$ nm/s, $v_{7\%} = (5.7 \pm 3.7)$ nm/s and $v_{10\%} = (1.8 \pm 1.3)$ nm/s were found. Notably, several events show velocities between ~20 nm/s and ~40 nm/s (Figure 78).

It is important to note, that no stalling events show up in the dual trap data. Furthermore, events show no decreasing velocities at higher deflections. Preliminary measurements at $k_{25\%}{\sim}25$ fN/nm and $k_{50\%}{\sim}50$ fN/nm show retraction events comparable to measurements $k_{2\%}{\sim}2$ fN/nm without stalling and confirm this tendency. Interestingly, velocities observed at $k_{10\%}{\sim}10$ fN/nm show a low median velocity.

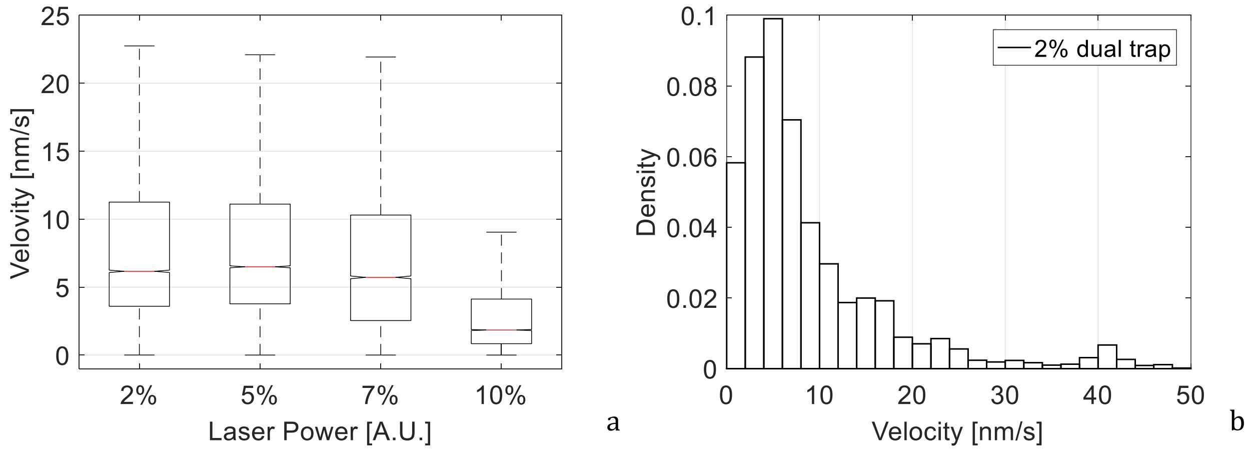

Figure 78: Retraction velocities of *ΔpilT*-cells (Ng178) in various trapping potentials were measured with dual laser tweezers. a) Boxplot of *ΔpilT* retraction speeds at various trap stiffness values $k_{2\%}{\sim}2$ fN/nm, $k_{5\%}{\sim}5$ fN/nm, $k_{7\%}{\sim}7$ fN/nm and $k_{10\%}{\sim}10$ fN/nm. Median values are displayed as red lines. N = (10-37) retraction events. b) Probability density of *ΔpilT* retraction velocities at $k_{2\%}{\sim}2$ fN/nm. N = 37 retraction events.

9 REFERENCES

[1] “Microbiology by numbers,” *Nature Reviews Microbiology*, vol. 9, no. 9, Nature Publishing Group, p. 628, 01-Sep-2011.

[2] M. L. Smith, J. N. Bruhn, and J. B. Anderson, “The fungus Armillaria bulbosa is among the largest and oldest living organisms,” *Nature*, vol. 356, no. 6368, pp. 428–431, Apr. 1992.

[3] S. Arnaud-Haond, C. M. Duarte, E. Diaz-Almela, N. Marbà, T. Sintes, and E. A. Serrão, “Implications of extreme life span in clonal organisms: Millenary clones in meadows of the threatened seagrass posidonia oceanica,” *PLoS ONE*, vol. 7, no. 2. Public Library of Science, p. e30454, 2012.

[4] F. Mwalongo, M. Krone, M. Becher, G. Reina, and T. Ertl, “GPU-based remote visualization of dynamic molecular data on the web,” *Graph. Models*, vol. 88, pp. 57–65, Nov. 2016.

[5] O. Reynolds, “An Experimental Investigation of the Circumstances Which Determine Whether the Motion of Water Shall Be Direct or Sinuous, and of the Law of Resistance in Parallel Channels,” *Philos. Trans. R. Soc. London*, vol. 174, no. 224–226, pp. 935–982, Jan. 1883.

[6] M. C. Marchetti *et al.*, “Hydrodynamics of soft active matter,” *Rev. Mod. Phys.*, vol. 85, no. 3, pp. 1143–1189, Jul. 2013.

[7] J. Elgeti, R. G. Winkler, and G. Gompper, “Physics of microswimmers - Single particle motion and collective behavior: A review,” *Reports Prog. Phys.*, vol. 78, no. 5, p. 056601, May 2015.

[8] M. Hennes, J. Tailleur, G. Charron, and A. Daerr, “Active depinning of bacterial droplets: The collective surfing of Bacillus subtilis,” *Proc. Natl. Acad. Sci.*, vol. 114, no. 23, pp. 5958–5963, May 2017.

[9] M. Valignat, O. Theodoly, J. C. Crocker, W. B. Russel, and P. M. Chaikin, “Reversible self-assembly and directed assembly of DNA-linked micrometer-sized colloids,” *Proc. Natl. Acad. Sci.*, vol. 102, no. 12, pp. 4225–4229, 2005.

[10] K. Drescher *et al.*, “Architectural transitions in Vibrio cholerae biofilms at single-cell resolution,” *Proc. Natl. Acad. Sci.*, vol. 113, no. 14, pp. E2066–E2072, Apr. 2016.

[11] W. P. J. Smith, Y. Davit, J. M. Osborne, W. Kim, K. R. Foster, and J. M. Pitt-Francis, “Cell morphology drives spatial patterning in microbial communities,” *Proc. Natl. Acad. Sci.*, vol. 114, no. 3, pp. E280–E286, 2017.

[12] D. Bonazzi *et al.*, “Intermittent Pili-Mediated Forces Fluidize Neisseria meningitidis Aggregates Promoting Vascular Colonization,” *Cell*, vol. 174, no. 1, p. 143–155.e16, 2018.

[13] E. R. Oldewurtel, N. Kouzel, L. Dewenter, K. Henseler, and B. Maier, “Differential interaction forces govern bacterial sorting in early biofilms,” *Elife*, vol. 4, no. September, pp. 1–21, 2015.

[14] B. Maier and G. C. L. Wong, “How Bacteria Use Type IV Pili Machinery on Surfaces,” *Trends in Microbiology*, vol. 23, no. 12. Elsevier Current Trends, pp. 775–788, 01-Dec-2015.

[15] J. Taktikos, Y. T. Lin, H. Stark, N. Biais, and V. Zaburdaev, “Pili-induced clustering of N. Gonorrhoeae Bacteria,” *PLoS One*, vol. 10, no. 9, 2015.

[16] D. R. Zusman, A. E. Scott, Z. Yang, and J. R. Kirby, “Chemosensory pathways, motility and development in Myxococcus xanthus,” *Nature Reviews Microbiology*, vol. 5, no. 11. Nature Publishing Group, pp. 862–872, 01-Nov-2007.

[17] D. Bhaya, K. Nakasugi, F. Fazeli, and M. S. Burriesci, “Phototaxis and impaired motility in adenylyl cyclase and cyclase receptor protein mutants of Synechocystis sp. strain PCC 6803,” *J. Bacteriol.*, vol. 188, no. 20, pp. 7306–7310, Oct. 2006.

[18] D. Nakane and T. Nishizaka, “Asymmetric distribution of type IV pili triggered by directional light in unicellular cyanobacteria,” *Proc. Natl. Acad. Sci.*, vol. 114, no. 25, 2017.

[19] P. Varuni, S. N. Menon, and G. I. Menon, “Phototaxis as a Collective Phenomenon in Cyanobacterial Colonies,” *Sci. Rep.*, vol. 7, no. 1, p. 17799, Dec. 2017.

[20] M. Sidortsov, Y. Morgenstern, and A. Be’Er, “Role of tumbling in bacterial swarming,”

Phys. Rev. E, vol. 96, no. 2, 2017.

[21] S. H. Larsen, R. W. Reader, E. N. Kort, W. W. Tso, and J. Adler, "Change in direction of flagellar rotation is the basis of the chemotactic response in Escherichia coli," *Nature*, vol. 249, no. 5452, pp. 74–77, May 1974.

[22] N. C. Darnton, L. Turner, S. Rojevsky, and H. C. Berg, "On torque and tumbling in swimming Escherichia coli," *J. Bacteriol.*, vol. 189, no. 5, pp. 1756–1764, 2007.

[23] G. H. Wadhams and J. P. Armitage, "Making sense of it all: Bacterial chemotaxis," *Nature Reviews Molecular Cell Biology*, vol. 5, no. 12. Nature Publishing Group, pp. 1024–1037, 01-Dec-2004.

[24] M. Hennes, "Du fluide passif à la matière active: Mouillage de gels et dynamique collective de bactéries," UNIVERSITÉ DE PARIS VII - U.F.R DE PHYSIQUE, 2017.

[25] D. Julkowska, M. Obuchowski, I. B. Holland, and S. J. Séror, "Comparative analysis of the development of swarming communities of Bacillus subtilis 168 and a natural wild type: Critical effects of surfactin and the composition of the medium," in *Journal of Bacteriology*, 2005, vol. 187, no. 1, pp. 65–76.

[26] F. D. C. Farrell, O. Hallatschek, D. Marenduzzo, and B. Waclaw, "Mechanically driven growth of quasi-two-dimensional microbial colonies," *Phys. Rev. Lett.*, vol. 111, no. 16, p. 168101, Oct. 2013.

[27] J. Ribbe, A. E. Baker, S. Euler, G. A. O'Toole, and B. Maier, "Role of cyclic di-GMP and exopolysaccharide in type IV pilus dynamics," *J. Bacteriol.*, vol. 199, no. 8, pp. e00859-16, 2017.

[28] T. Kohler, L. K. Curty, F. Barja, C. Van Delden, and J. C. Pechere, "Swarming of Pseudomonas aeruginosa is dependent on cell-to-cell signaling and requires flagella and pili," *J. Bacteriol.*, vol. 182, no. 21, pp. 5990–5996, Nov. 2000.

[29] J. Overhage, M. Bains, M. D. Brazas, and R. E. W. Hancock, "Swarming of Pseudomonas aeruginosa is a complex adaptation leading to increased production of virulence factors and antibiotic resistance," *J. Bacteriol.*, vol. 190, no. 8, pp. 2671–2679, Apr. 2008.

[30] M. E. Anyan *et al.*, "Type IV pili interactions promote intercellular association and

moderate swarming of Pseudomonas aeruginosa," *Proc. Natl. Acad. Sci.*, vol. 111, no. 50, pp. 18013–18018, Dec. 2014.

[31] M. Klausen *et al.*, "Biofilm formation by Pseudomonas aeruginosa wild type, flagella and type IV pili mutants," *Mol. Microbiol.*, vol. 48, no. 6, pp. 1511–1524, 2003.

[32] B. Nan, M. J. McBride, J. Chen, D. R. Zusman, and G. Oster, "Bacteria that glide with helical tracks," *Current Biology*, vol. 24, no. 4. 2014.

[33] M. Sun, M. Wartel, E. Cascales, J. W. Shaevitz, and T. Mignot, "Motor-driven intracellular transport powers bacterial gliding motility," *Proc. Natl. Acad. Sci.*, vol. 108, no. 18, pp. 7559–7564, 2011.

[34] R. P. Burchard and A. Rich, "Gliding Motility and Taxes," no. Kilhlwein 1957, pp. 139–164, 1984.

[35] V. H. Bustamante, I. Martínez-Flores, H. C. Vlamakis, and D. R. Zusman, "Analysis of the Frz signal transduction system of Myxococcus xanthus shows the importance of the conserved C-terminal region of the cytoplasmic chemoreceptor FrzCD in sensing signals," *Mol. Microbiol.*, vol. 53, no. 5, pp. 1501–1513, Jul. 2004.

[36] K. F. Jarrell and M. J. McBride, "The surprisingly diverse ways that prokaryotes move," *Nature Reviews Microbiology*, vol. 6, no. 6. Nature Publishing Group, pp. 466–476, 07-Jun-2008.

[37] R. Phillips, J. Kondev, J. Theriot, H. Garcia, and B. Chasan, *Physical Biology of the Cell*, vol. 78, no. 11. 2010.

[38] C. S. Peskin, G. M. Odell, and G. F. Oster, "Cellular motions and thermal fluctuations: the Brownian ratchet," *Biophys. J.*, vol. 65, no. 1, pp. 316–324, 1993.

[39] E. Sackmann and R. Merkel, *Lehrbuch der Biophysik*. 2010.

[40] N. Thomas, Y. Imafuku, and K. Tawada, "Molecular motors: Thermodynamics and the random walk," *Proc. R. Soc. B Biol. Sci.*, vol. 268, no. 1481, pp. 2113–2122, Oct. 2001.

[41] Y. Sowa *et al.*, "Direct observation of steps in rotation of the bacterial flagellar motor," *Nature*, vol. 437, no. 7060, pp. 916–919, Oct. 2005.

[42] V. A. M. Gold, R. Salzer, B. Averhoff, and W. Kühlbrandt, "Structure of a type IV pilus

machinery in the open and closed state," *Elife*, vol. 4, no. MAY, 2015.

[43] T. J. Herdendorf, D. R. McCaslin, and K. T. Forest, "Aquifex aeolicus PilT, homologue of a surface motility protein, is a thermostable oligomeric NTPase," *J. Bacteriol.*, vol. 184, no. 23, pp. 6465–6471, Dec. 2002.

[44] M. McCallum, S. Tammam, A. Khan, L. L. Burrows, and P. L. Howell, "The molecular mechanism of the type IVa pilus motors," *Nat. Commun.*, vol. 8, 2017.

[45] T. Rudel, D. Facius, R. Barten, I. Scheuerpflug, E. Nonnenmacher, and T. F. Meyer, "Role of pili and the phase-variable PilC protein in natural competence for transformation of Neisseria gonorrhoeae.," *Proc. Natl. Acad. Sci. U. S. A.*, vol. 92, no. 17, pp. 7986–90, Aug. 1995.

[46] T. Rudel, I. Scheuerpflug, and T. F. Meyer, "Neisseria PilC protein identified as type-4 pilus tip-located adhesin," *Nature*, vol. 373, no. 6512, pp. 357–359, Jan. 1995.

[47] B. Maier, L. Potter, M. So, H. S. Seifert, and M. P. Sheetz, "Single pilus motor forces exceed 100 pN," *Proc. Natl. Acad. Sci.*, vol. 99, no. 25, pp. 16012–16017, Dec. 2002.

[48] G. O'Toole, H. B. Kaplan, and R. Kolter, "Biofilm Formation as Microbial Development," *Annu. Rev. Microbiol.*, vol. 54, no. 1, pp. 49–79, Oct. 2000.

[49] N. Biais, B. Ladoux, D. Higashi, M. So, and M. Sheetz, "Cooperative retraction of bundled type IV pili enables nanonewton force generation," *PLoS Biol.*, vol. 6, no. 4, pp. 907–913, 2008.

[50] M. Clausen, V. Jakovljevic, L. Søgaard-Andersen, and B. Maier, "High-force generation is a conserved property of type IV pilus systems," *J. Bacteriol.*, vol. 191, no. 14, pp. 4633–4638, 2009.

[51] R. Kurre, N. Kouzel, K. Ramakrishnan, E. R. Oldewurtel, and B. Maier, "Speed Switching of Gonococcal Surface Motility Correlates with Proton Motive Force," *PLoS One*, vol. 8, no. 6, 2013.

[52] R. Kurre and B. Maier, "Oxygen depletion triggers switching between discrete speed modes of gonococcal type IV pili," *Biophys. J.*, vol. 102, no. 11, pp. 2556–2563, Jun. 2012.

[53] R. Marathe *et al.*, "Bacterial twitching motility is coordinated by a two-dimensional tug-

of-war with directional memory," *Nat. Commun.*, vol. 5, no. May, p. 3759, 2014.

[54] J. Swanson, "Studies on gonococcus infection. IV. Pili: their role in attachment of gonococci to tissue culture cells.," *J. Exp. Med.*, vol. 137, no. 3, pp. 571–89, Mar. 1973.

[55] V. Zaburdaev *et al.*, "Uncovering the mechanism of trapping and cell orientation during Neisseria gonorrhoeae twitching motility," *Biophys. J.*, vol. 107, no. 7, 2014.

[56] C. Meel, N. Kouzel, E. R. Oldewurtel, and B. Maier, "Three-dimensional obstacles for bacterial surface motility," *Small*, vol. 8, no. 4, pp. 530–534, Feb. 2012.

[57] R. M. May *et al.*, "Micro-patterned surfaces reduce bacterial colonization and biofilm formation in vitro: Potential for enhancing endotracheal tube designs," *Clin. Transl. Med.*, vol. 3, no. 1, p. 8, Apr. 2014.

[58] A. Persat, Y. F. Inclan, J. N. Engel, H. A. Stone, and Z. Gitai, "Type IV pili mechanochemically regulate virulence factors in Pseudomonas aeruginosa," *Proc. Natl. Acad. Sci.*, vol. 112, no. 24, pp. 7563–7568, 2015.

[59] Y. Luo *et al.*, "A hierarchical cascade of second messengers regulates Pseudomonas aeruginosa Surface Behaviors," *MBio*, vol. 6, no. 1, 2015.

[60] A. Ashkin, J. M. Dziedzic, J. E. Bjorkholm, and S. Chu, "Observation of a single-beam gradient force optical trap for dielectric particles," *Opt. Lett.*, vol. 11, no. 5, p. 288, 1986.

[61] "The Nobel Prize in Physics 2018," *Nobel Media AB*. [Online]. Available: https://www.nobelprize.org/prizes/physics/2018/summary/. [Accessed: 15-Oct-2018].

[62] E. A. Abbondanzieri, W. J. Greenleaf, J. W. Shaevitz, R. Landick, and S. M. Block, "Direct observation of base-pair stepping by RNA polymerase," *Nature*, vol. 438, no. 7067, pp. 460–465, Nov. 2005.

[63] B. Sabass, M. D. Koch, G. Liu, H. A. Stone, and J. W. Shaevitz, "Force generation by groups of migrating bacteria," *Proc. Natl. Acad. Sci. U. S. A.*, vol. 114, no. 28, pp. 7266–7271, Jul. 2017.

[64] N. Biais, D. L. Higashi, J. Brujic, M. So, and M. P. Sheetz, "Force-dependent polymorphism in type IV pili reveals hidden epitopes," *Proc. Natl. Acad. Sci.*, vol. 107, no. 25, pp.

11358–11363, Jun. 2010.

[65] G. Anastasiadi, M. Leonard, L. Paterson, and W. N. Macpherson, "Fabrication and characterization of machined multi-core fiber tweezers for single cell manipulation," *Opt. Express*, vol. 26, no. 3, pp. 239–246, 2018.

[66] L. A. Shaw, C. M. Spadaccini, and J. B. Hopkins, "Scanning holographic optical tweezers," *Opt. Lett.*, vol. 42, no. 15, p. 2862, Aug. 2017.

[67] Y. Harada and T. Asakura, "Radiation forces on a dielectric sphere in the Rayleigh scattering regime," *Opt. Commun.*, vol. 124, no. 5–6, pp. 529–541, 1996.

[68] K. C. Neuman and S. M. Block, "Optical trapping," *Rev. Sci. Instrum.*, vol. 75, no. 9, pp. 2787–2809, 2004.

[69] A. Ashkin, "Forces of a single-beam gradient laser trap on a dielectric sphere in the ray optics regime," *Biophys. J.*, vol. 61, no. 2, pp. 569–582, Feb. 1992.

[70] K. Visscher, S. P. Gross, and S. M. Block, "Construction of multiple-beam optical traps with nanometer-resolution position sensing," *IEEE J. Sel. Top. Quantum Electron.*, vol. 2, no. 4, pp. 1066–1076, 1996.

[71] D. G. Grier, "A revolution in optical manipulation.," *Nature*, vol. 424, no. 6950, pp. 810–6, Aug. 2003.

[72] G. Whyte, G. Gibson, J. Leach, M. Padgett, D. Robert, and M. Miles, "An optical trapped microhand for manipulating micron-sized objects," *Opt. Express*, vol. 14, no. 25, p. 12497, Dec. 2006.

[73] G. D. Reddy and P. Saggau, "Fast three-dimensional laser scanning scheme using acousto-optic deflectors," *J. Biomed. Opt.*, vol. 10, no. 6, p. 064038, 2005.

[74] M. Van Der Woude and A. Bäumler, "Phase and antigenic variation in bacteria," *Clin. Microbiol. Rev.*, vol. 17, no. 3, p. 581–611, table of contents, 2004.

[75] F. Wisniewski-Dyé and L. Vial, "Phase and antigenic variation mediated by genome modifications," *Antonie van Leeuwenhoek, International Journal of General and Molecular Microbiology*, vol. 94, no. 4. pp. 493–515, 2008.

[76] S. Makino, J. P. van Putten, and T. F. Meyer, "Phase variation of the opacity outer

membrane protein controls invasion by Neisseria gonorrhoeae into human epithelial cells.," *EMBO J.*, vol. 10, no. 6, pp. 1307–15, Jun. 1991.

[77] T. Rudel, J. P. M. van Putten, C. P. Gibbs, R. Haas, and T. F. Meyer, "Interaction of two variable proteins (PilE and PilC) required for pilus-mediated adherence of Neisseria gonorrhoeae to human epithelial cells," *Mol. Microbiol.*, vol. 6, no. 22, pp. 3439–3450, Nov. 1992.

[78] T. Davidsen and T. Tønjum, "Meningococcal genome dynamics," *Nature Reviews Microbiology*, vol. 4, no. 1. Nature Publishing Group, pp. 11–22, 01-Jan-2006.

[79] R. Zöllner, E. R. Oldewurtel, N. Kouzel, and B. Maier, "Phase and antigenic variation govern competition dynamics through positioning in bacterial colonies," *Sci. Rep.*, vol. 7, no. 1, p. 12151, 2017.

[80] E. Rotman and H. S. Seifert, "The Genetics of Neisseria Species," *Annu. Rev. Genet.*, vol. 48, no. 1, pp. 405–431, Nov. 2014.

[81] L. A. Cahoon and H. S. Seifert, "An alternative DNA structure is necessary for pilin antigenic variation in Neisseria gonorrhoeae," *Science (80-.).*, vol. 325, no. 5941, pp. 764–767, 2009.

[82] E. Rotman and H. Steven Seifert, "Neisseria gonorrhoeae muts affects pilin antigenic variation through mismatch correction and not by pilE guanine quartet binding," *J. Bacteriol.*, vol. 197, no. 10, pp. 1828–1838, 2015.

[83] H. E. Parge, K. T. Forest, M. J. Hickey, D. A. Christensen, E. D. Getzoff, and J. A. Tainer, "Structure of the fibre-forming protein pilin at 2.6 Å resolution," *Nature*, vol. 378, no. 6552, pp. 32–38, 1995.

[84] F. T. Hegge *et al.*, "Unique modifications with phosphocholine and phosphoethanolamine define alternate antigenic forms of Neisseria gonorrhoeae type IV pili," *Proc. Natl. Acad. Sci.*, vol. 101, no. 29, pp. 10798–10803, Jul. 2004.

[85] F. E. Aas, Å.° Vik, J. Vedde, M. Koomey, and W. Egge-Jacobsen, "Neisseria gonorrhoeae O-linked pilin glycosylation: Functional analyses define both the biosynthetic pathway and glycan structure," *Mol. Microbiol.*, vol. 65, no. 3, pp. 607–624, Jun. 2007.

[86] C. L. Næssan *et al.*, “Genetic and functional analyses of PptA, a phospho-form transferase targeting type IV pili in Neisseria gonorrhoeae,” *J. Bacteriol.*, vol. 190, no. 1, pp. 387–400, 2008.

[87] R. Zöllner, T. Cronenberg, N. Kouzel, A. Welker, M. Koomey, and B. Maier, “Type IV pilin post-translational modifications modulate materials properties of bacterial colonies,” *bioRxiv*, p. 389882, Aug. 2018.

[88] G. Wayne Brodland and H. H. Chen, “The mechanics of cell sorting and envelopment,” *J. Biomech.*, vol. 33, no. 7, pp. 845–851, Jul. 2000.

[89] J. H. Shawky and L. A. Davidson, “Tissue mechanics and adhesion during embryo development,” *Dev. Biol.*, vol. 401, no. 1, pp. 152–164, May 2015.

[90] L. L. Greiner, J. L. Edwards, J. Shao, C. Rabinak, D. Entz, and M. A. Apicella, “Biofilm formation by Neisseria gonorrhoeae,” *Infect. Immun.*, vol. 73, no. 4, pp. 1964–1970, 2005.

[91] H. C. Flemming, J. Wingender, U. Szewzyk, P. Steinberg, S. A. Rice, and S. Kjelleberg, “Biofilms: An emergent form of bacterial life,” *Nature Reviews Microbiology*, vol. 14, no. 9. Nature Publishing Group, pp. 563–575, 01-Sep-2016.

[92] M. E. Ramsey, K. L. Woodhams, and J. P. Dillard, “The gonococcal genetic island and type IV secretion in the pathogenic Neisseria,” *Front. Microbiol.*, vol. 2, 2011.

[93] P. S. Stewart and J. W. Costerton, “Antibiotic resistance of bacteria in biofilms.,” *Lancet*, vol. 358, no. 9276, pp. 135–8, Jul. 2001.

[94] A. Dötsch and D. Eckweiler, “The Pseudomonas aeruginosa transcriptome in planktonic cultures and static biofilms using RNA sequencing,” *PLoS One*, vol. 7, no. 2, p. e31092, Jan. 2012.

[95] T. Mah and G. O’Toole, “Mechanisms of biofilm resistance to antimicrobial agents,” *Trends Microbiol.*, vol. 9, no. 1, pp. 34–39, Jan. 2001.

[96] A. L. Spoering and K. Lewis, “Biofilms and planktonic cells of Pseudomonas aeruginosa have similar resistance to killing by antimicrobials,” *J. Bacteriol.*, vol. 183, no. 23, pp. 6746–6751, 2001.

[97] K. Sauer, “The genomics and proteomics of biofilm formation,” *Genome Biology*, vol. 4, no. 6. BioMed Central, p. 219, 27-May-2003.

[98] S. L. Kuchma, E. F. Griffin, and G. A. O’Toole, “Minor pilins of the type IV pilus system participate in the negative regulation of swarming motility,” *J. Bacteriol.*, vol. 194, no. 19, pp. 5388–5403, 2012.

[99] C. D. Nadell, D. Ricaurte, J. Yan, K. Drescher, and B. L. Bassler, “Flow environment and matrix structure interact to determine spatial competition in Pseudomonas aeruginosa biofilms,” *Elife*, vol. 6, Jan. 2017.

[100] C. Beloin, A. Roux, and J. M. Ghigo, “Escherichia coli biofilms,” *Current Topics in Microbiology and Immunology*, vol. 322. Inserm, pp. 249–289, 2008.

[101] L. Vidakovic, P. K. Singh, R. Hartmann, C. D. Nadell, and K. Drescher, “Dynamic biofilm architecture confers individual and collective mechanisms of viral protection,” *Nat. Microbiol.*, vol. 3, no. 1, pp. 26–31, Jan. 2017.

[102] M. Lappann, J. A. J. Haagensen, H. Claus, U. Vogel, and S. Molin, “Meningococcal biofilm formation: Structure, development and phenotypes in a standardized continuous flow system,” *Mol. Microbiol.*, vol. 62, no. 5, pp. 1292–1309, Dec. 2006.

[103] A. M. Hockenberry, D. M. Hutchens, A. Agellon, and M. So, “Attenuation of the type IV pilus retraction motor influences Neisseria gonorrhoeae social and infection behavior,” *MBio*, 2016.

[104] W. Pönisch, C. A. Weber, G. Juckeland, N. Biais, and V. Zaburdaev, “Multiscale modeling of bacterial colonies: How pili mediate the dynamics of single cells and cellular aggregates,” *New J. Phys.*, vol. 19, no. 1, 2017.

[105] W. Pönisch *et al.*, “Pili mediated intercellular forces shape heterogeneous bacterial microcolonies as a precursor for multicellular differentiation,” *arXiv Prepr.*, vol. 8, no. 1, pp. 1–44, Dec. 2017.

[106] N. Kouzel, E. R. Oldewurtel, and B. Maier, “Gene transfer efficiency in gonococcal biofilms: Role of biofilm age, architecture, and pilin antigenic variation,” *J. Bacteriol.*, vol. 197, no. 14, pp. 2422–2431, Jul. 2015.

[107] M. S. Steinberg, “Reconstruction of tissues by dissociated cells,” *Sci. Sci.*, vol. 141, no. 3579, pp. 401–408, 1963.

[108] R. A. Foty and M. S. Steinberg, “Differential adhesion in model systems,” *Wiley Interdiscip. Rev. Dev. Biol.*, vol. 2, no. 5, pp. 631–645, Sep. 2013.

[109] a K. Harris, “Is Cell sorting caused by differences in the work of intercellular adhesion? A critique of the Steinberg hypothesis.,” *J. Theor. Biol.*, vol. 61, no. 2, pp. 267–285, 1976.

[110] M. A. Nowak, *Evolutionary dynamics*. Harvard University Press, 2006.

[111] M. Lässig, “From biophysics to evolutionary genetics: statistical aspects of gene regulation,” *BMC Bioinformatics*, vol. 8 Suppl 6, p. S7, Jan. 2007.

[112] O. Hallatschek, P. Hersen, S. Ramanathan, and D. R. Nelson, “Genetic drift at expanding frontiers promotes gene segregation.,” *Proc. Natl. Acad. Sci. U. S. A.*, vol. 104, no. 50, pp. 19926–30, Dec. 2007.

[113] K. Korolev, M. Müller, and N. Karahan, “Selective sweeps in growing microbial colonies,” *Phys. Biol.*, vol. 9, no. 2, p. 026008, Jan. 2012.

[114] S. Mitri, E. Clarke, and K. R. Foster, “Resource limitation drives spatial organization in microbial groups,” *ISME J.*, vol. 10, no. 6, pp. 1471–1482, 2016.

[115] I. Frost *et al.*, “Cooperation, competition and antibiotic resistance in bacterial colonies,” *ISME J.*, 2018.

[116] D. Fusco, M. Gralka, J. Kayser, A. Anderson, and O. Hallatschek, “Excess of mutational jackpot events in expanding populations revealed by spatial Luria-Delbrück experiments,” *Nat. Commun.*, vol. 7, 2016.

[117] C. D. Nadell, K. Drescher, and K. R. Foster, “Spatial structure, cooperation and competition in biofilms,” *Nature Reviews Microbiology*, vol. 14, no. 9. Nature Publishing Group, pp. 589–600, 25-Sep-2016.

[118] K. Ledwoch *et al.*, “Beware biofilm! Dry biofilms containing bacterial pathogens on multiple healthcare surfaces; a multi-centre study,” *Journal of Hospital Infection*, vol. 100, no. 3, W.B. Saunders, pp. e47–e56, 01-Nov-2018.

[119] H. P. Steenackers, I. Parijs, K. R. Foster, and J. Vanderleyden, “Experimental evolution

in biofilm populations," *FEMS Microbiology Reviews*, vol. 40, no. 3. Oxford University Press, pp. 373–397, 01-May-2016.

[120] L. Yang, Y. Liu, H. Wu, N. Høiby, S. Molin, and Z. Song, "Current understanding of multi-species biofilms," *Int. J. Oral Sci.*, vol. 3, no. 2, pp. 74–81, Apr. 2011.

[121] S. R. Poltak and V. S. Cooper, "Ecological succession in long-term experimentally evolved biofilms produces synergistic communities," *ISME J.*, vol. 5, no. 3, pp. 369–378, Mar. 2011.

[122] J. Friedman and J. Gore, "Ecological systems biology: The dynamics of interacting populations," *Current Opinion in Systems Biology*, vol. 1. pp. 114–121, 2017.

[123] I. Chen and D. Dubnau, "DNA uptake during bacterial transformation," *Nat. Rev. Microbiol.*, vol. 2, no. 3, pp. 241–249, Mar. 2004.

[124] R. Kurre, A. Höne, M. Clausen, C. Meel, and B. Maier, "PilT2 enhances the speed of gonococcal type IV pilus retraction and of twitching motility," *Mol. Microbiol.*, vol. 86, no. 4, pp. 857–865, Nov. 2012.

[125] C. Holz *et al.*, "Multiple pilus motors cooperate for persistent bacterial movement in two dimensions," *Phys. Rev. Lett.*, vol. 104, no. 17, p. 178104, 2010.

[126] A. Welker *et al.*, "Molecular Motors Govern Liquidlike Ordering and Fusion Dynamics of Bacterial Colonies," *Phys. Rev. Lett.*, vol. 121, no. 11, p. 118102, Sep. 2018.

[127] M. Wolfgang, "Components and dynamics of fiber formation define a ubiquitous biogenesis pathway for bacterial pili," *EMBO J.*, vol. 19, no. 23, pp. 6408–6418, 2000.

[128] J. J. Power, "Horizontal Gene Transfer Between Subspecies Affects Bacterial Genome Dynamics," Universität zu Köln, 2018.

[129] H. S. Seifert, C. J. Wright, A. E. Jerse, M. S. Cohen, and J. G. Cannon, "Multiple gonococcal pilin antigenic variants are produced during experimental human infections.," *J. Clin. Invest.*, vol. 93, no. 6, pp. 2744–9, Jun. 1994.

[130] C. J. Wright, A. E. Jerse, M. S. Cohen, J. G. Cannon, and H. S. Seifert, "Nonrepresentative PCR amplification of variable gene sequences in clinical specimens containing dilute, complex mixtures of microorganisms.," *J. Clin. Microbiol.*, vol. 32, no. 2, pp. 464–8, Feb.

1994.

[131] J. M. Koomey and S. Falkow, “Cloning of the recA gene of Neisseria gonorrhoeae and construction of gonococcal recA mutants,” *J. Bacteriol.*, vol. 169, no. 2, pp. 790–795, Feb. 1987.

[132] J. Swanson, “Studies on gonococcus infection. II. Freeze-fracture, freeze-etch studies on gonocci.,” *J. Exp. Med.*, vol. 136, no. 5, pp. 1258–71, Nov. 1972.

[133] H. S. Seifert, “Insertionally inactivated and inducible recA alleles for use in Neisseria,” *Gene*, vol. 188, no. 2, pp. 215–220, 1997.

[134] T. Tønjum, N. E. Freitag, E. Namork, and M. Koomey, “Identification and characterization of pilG, a highly conserved pilus-assembly gene in pathogenic Neisseria,” *Mol. Microbiol.*, vol. 16, no. 3, pp. 451–464, May 1995.

[135] D. Opitz, “Mechanical forces during the infection of human epithelial cells with Neisseria gonorrhoeae,” Westfälische Wilhelms-Universität Münster, 2011.

[136] N. Stuurman, N. Amdodaj, and R. Vale, “μManager: Open Source Software for Light Microscope Imaging,” *Micros. Today*, vol. 15, no. 3, pp. 42–43, May 2007.

[137] J. Schindelin *et al.*, “Fiji: an open-source platform for biological-image analysis,” *Nat. Methods*, vol. 9, no. 7, pp. 676–682, Jul. 2012.

[138] M. Richards, J. Scheer, W. Holm, and W. Melvin, *Principles of Modern Radar: Advanced techniques*. 2012.

[139] *AD9852 CMOS 300 MSPS Complete DDS Manual*. Analog Devices, 2007.

[140] P. V. C. Hough, “Method and means for recognizing complex patterns,” *US Pat. 3,069,654*, vol. 21, pp. 225–231, 1962.

[141] M. R. M. and M. K. Mohamed Rizon, Haniza Yazid, Puteh Saad, Ali Yeon Md Shakaff, Abdul Rahman Saad, Masanori Sugisaka, Sazali Yaacob, “Object Detection using Circular Hough Transform,” *Am. J. Appl. Sci.*, vol. 2, no. 12, pp. 1606–1609, 2005.

[142] L. D. Landau and E. M. Lifshitz, *Fluid mechanics*. Oxford: Elsevier, 2004.

[143] R. Feynman, *Feynman lectures on Physics Volume 2*. Basic Books, 1974.

[144] M. Rieutord, *Fluid Dynamics*. Cham: Springer International Publishing, 2015.

[145] K. C. Huang, R. Mukhopadhyay, B. Wen, Z. Gitai, and N. S. Wingreen, “Cell shape and cell-wall organization in Gram-negative bacteria,” *Proc. Natl. Acad. Sci.*, vol. 105, no. 49, pp. 19282–19287, Dec. 2008.

[146] C. D. Pericone, K. Overweg, P. W. M. Hermans, and J. N. Weiser, “Inhibitory and Bactericidal Effects of Hydrogen Peroxide Production by Streptococcus pneumoniae on Other Inhabitants of the Upper Respiratory Tract,” *Infect. Immun.*, vol. 68, no. 7, pp. 3990–3997, 2000.

[147] L. A. Cahoon and H. S. Seifert, “An alternative DNA structure is necessary for pilin antigenic variation in Neisseria gonorrhoeae,” *Science (80-.).*, vol. 325, no. 5941, pp. 764–767, 2009.

[148] J. L. Lozán and H. Kausch, *Angewandte Statistik für Naturwissenschaftler*. Wissenschaftliche Auswertungen, 2007.

[149] O. Otto *et al.*, “Real-time deformability cytometry: On-the-fly cell mechanical phenotyping,” *Nat. Methods*, vol. 12, no. 3, pp. 199–202, Mar. 2015.

[150] J. T. Bullerjahn, S. Sturm, and K. Kroy, “Theory of rapid force spectroscopy,” *Nat. Commun.*, vol. 5, pp. 1–10, 2014.

[151] A. M. Misic, K. A. Satyshur, and K. T. Forest, “P. aeruginosa PilT Structures with and without Nucleotide Reveal a Dynamic Type IV Pilus Retraction Motor,” *J. Mol. Biol.*, vol. 400, no. 5, pp. 1011–1021, 2010.

[152] R. Gordon, N. S. Goel, M. S. Steinberg, and L. L. Wiseman, “A rheological mechanism sufficient to explain the kinetics of cell sorting,” *J. Theor. Biol.*, vol. 37, no. 1, pp. 43–73, Oct. 1972.

[153] R. Grima and S. Schnell, “Can tissue surface tension drive somite formation?,” *Dev. Biol.*, vol. 307, no. 2, pp. 248–257, Jul. 2007.

[154] M. Wolfgang, P. Lauer, H. S. Park, L. Brossay, J. Hébert, and M. Koomey, “PilT mutations lead to simultaneous defects in competence for natural transformation and twitching motility in piliated Neisseria gonorrhoeae,” *Mol. Microbiol.*, vol. 29, no. 1, pp. 321–330,

Jul. 1998.

[155] C. K. Ellison *et al.*, “Retraction of DNA-bound type IV competence pili initiates DNA uptake during natural transformation in Vibrio cholerae,” *Nat. Microbiol.*, vol. 3, no. 7, pp. 773–780, Jul. 2018.

[156] D. Ng *et al.*, “The Vibrio cholerae Minor Pilin TcpB Initiates Assembly and Retraction of the Toxin-Coregulated Pilus,” *PLoS Pathog.*, vol. 12, no. 12, p. e1006109, Dec. 2016.

[157] C. Holz, D. Opitz, J. Mehlich, B. J. Ravoo, and B. Maier, “Bacterial motility and clustering guided by microcontact printing,” *Nano Lett.*, vol. 9, no. 12, pp. 4553–4557, Dec. 2009.

[158] H. Gangel *et al.*, “Concerted Spatio-Temporal Dynamics of Imported DNA and ComE DNA Uptake Protein during Gonococcal Transformation,” *PLoS Pathog.*, vol. 10, no. 4, p. e1004043, Apr. 2014.

[159] C. Hepp and B. Maier, “Kinetics of DNA uptake during transformation provide evidence for a translocation ratchet mechanism.,” *Proc. Natl. Acad. Sci. U. S. A.*, vol. 113, no. 44, pp. 12467–12472, 2016.

[160] P. Novotny, J. A. Short, and P. D. Walker, “An electron-microscope study of naturally occurring and cultured cells of Neisseria Gonorrhoeae.,” *J. Med. Microbiol.*, vol. 8, no. 3, pp. 413–27, Aug. 1975.

[161] M. Clausen, M. Koomey, and B. Maier, “Dynamics of type IV Pili Is controlled by switching between multiple states,” *Biophys. J.*, vol. 96, no. 3, pp. 1169–1177, Feb. 2009.

[162] B. Maier, M. Koomey, and M. P. Sheetz, “A force-dependent switch reverses type IV pilus retraction,” *Proc. Natl. Acad. Sci.*, vol. 101, no. 30, pp. 10961–10966, 2004.

[163] H. S. M. Park, M. Wolfgang, and M. Koomey, “Modification of type IV pilus-associated epithelial cell adherence and multicellular behavior by the PilU protein of Neisseria gonorrhoeae,” *Infect. Immun.*, vol. 70, no. 7, pp. 3891–3903, Jul. 2002.

[164] D. R. Brown, S. Helaine, E. Carbonnelle, and V. Pelicic, “Systematic functional analysis reveals that a set of seven genes is involved in fine-tuning of the multiple functions mediated by type IV pili in Neisseria meningitidis,” *Infect. Immun.*, vol. 78, no. 7, pp. 3053–3063, Jul. 2010.

[165] T. Minamino and K. Namba, “Distinct roles of the FliI ATPase and proton motive force in bacterial flagellar protein export,” *Nature*, vol. 451, no. 7177, pp. 485–488, Jan. 2008.

[166] C. Bradbeer, “The proton motive force drives the outer membrane transport of cobalamin in Escherichia coli,” *J. Bacteriol.*, vol. 175, no. 10, pp. 3146–3150, May 1993.

[167] B. Maier, I. Chen, D. Dubnau, and M. P. Sheetz, “DNA transport into Bacillus subtilis requires proton motive force to generate large molecular forces,” *Nat. Struct. Mol. Biol.*, vol. 11, no. 7, pp. 643–649, Jul. 2004.

[168] J. Kasianowicz, R. Benz, and S. McLaughlin, “The kinetic mechanism by which CCCP (carbonyl cyanide m-Chlorophenylhydrazone) transports protons across membranes,” *J. Membr. Biol.*, vol. 82, no. 2, pp. 179–190, Jun. 1984.

[169] R. Kurre, “Mechanisms of Fine-tuning in Type IV Pilus Dynamics,” Westfälische Wilhelms-Universität Münster, 2012.

[170] M. S. Blake, C. M. MacDonald, and K. P. Klugman, “Colony morphology of piliated Neisseria meningitidis.,” *J. Exp. Med.*, vol. 170, no. 5, pp. 1727–36, Nov. 1989.

[171] C. Vink, G. Rudenko, and H. S. Seifert, “Microbial antigenic variation mediated by homologous DNA recombination,” *FEMS Microbiology Reviews*, vol. 36, no. 5. Oxford University Press, pp. 917–948, 01-Sep-2012.

[172] O. Hallatschek and D. R. Nelson, “Gene surfing in expanding populations,” *Theor. Popul. Biol.*, vol. 73, no. 1, pp. 158–170, Feb. 2008.

[173] Y. Wu and H. C. Berg, “Water reservoir maintained by cell growth fuels the spreading of a bacterial swarm,” *Proc. Natl. Acad. Sci.*, vol. 109, no. 11, pp. 4128–4133, 2012.

[174] A. K. Criss, K. A. Kline, and H. S. Seifert, “The frequency and rate of pilin antigenic variation in Neisseria gonorrhoeae,” *Mol. Microbiol.*, vol. 58, no. 2, pp. 510–519, Oct. 2005.

[175] E. V. Sechman, M. S. Rohrer, and H. S. Seifert, “A genetic screen identifies genes and sites involved in pilin antigenic variation in Neisseria gonorrhoeae,” *Mol. Microbiol.*, vol. 57, no. 2, pp. 468–483, Jul. 2005.

[176] T. Hölscher *et al.*, “Motility, Chemotaxis and Aerotaxis Contribute to Competitiveness

during Bacterial Pellicle Biofilm Development," *J. Mol. Biol.*, vol. 427, no. 23, pp. 3695–3708, Nov. 2015.

[177] J. Barrick *et al.*, "Genome evolution and adaptation in a long-term experiment with Escherichia coli," *Nature*, vol. 461, no. 7268, pp. 1243–1247, Oct. 2009.

[178] G. I. Lang *et al.*, "Pervasive genetic hitchhiking and clonal interference in forty evolving yeast populations," *Nature*, vol. 500, no. 7464, pp. 571–574, Aug. 2013.

[179] J. F. Dempsey, W. Litaker, A. Madhure, T. L. Snodgrass, and J. G. Cannon, "Physical map of the chromosome of Neisseria gonorrhoeae FA1090 with locations of genetic markers, including opa and pil genes," *J. Bacteriol.*, vol. 173, no. 17, pp. 5476–5486, Sep. 1991.

[180] J. Le Digabel, N. Biais, J. Fresnais, J. F. Berret, P. Hersen, and B. Ladoux, "Magnetic micropillars as a tool to govern substrate deformations," *Lab Chip*, vol. 11, no. 15, pp. 2630–2636, Aug. 2011.

[181] A. Beaussart, A. E. Baker, S. L. Kuchma, S. El-Kirat-Chatel, G. A. Otoole, and Y. F. Dufrêne, "Nanoscale adhesion forces of Pseudomonas aeruginosa type IV pili," *ACS Nano*, vol. 8, no. 10, pp. 10723–10733, 2014.

[182] P. Loskill *et al.*, "Reduction of the peptidoglycan crosslinking causes a decrease in stiffness of the staphylococcus aureus cell envelope," *Biophys. J.*, vol. 107, no. 5, pp. 1082–1089, Sep. 2014.

[183] G. Hummer and A. Szabo, "Kinetics from nonequilibrium single-molecule pulling experiments," *Biophys. J.*, vol. 85, no. 1, pp. 5–15, Jul. 2003.

[184] J. Chamot-Rooke *et al.*, "Posttranslational modification of pili upon cell contact triggers N. meningitidis dissemination," *Science (80-.).*, vol. 331, no. 6018, pp. 778–782, Feb. 2011.

[185] L. Dewenter, T. E. Volkmann, and B. Maier, "Oxygen governs gonococcal microcolony stability by enhancing the interaction force between type IV pili," *Integr. Biol.*, vol. 7, no. 10, 2015.

[186] C. V Gabel and H. C. Berg, "The speed of the flagellar rotary motor of Escherichia coli

varies linearly with protonmotive force," *Proc. Natl. Acad. Sci.*, vol. 100, no. 15, pp. 8748–8751, Jul. 2003.

[187] D. Ribet and P. Cossart, "Post-translational modifications in host cells during bacterial infection," *FEBS Letters*, vol. 584, no. 13. No longer published by Elsevier, pp. 2748–2758, 02-Jul-2010.

[188] J. A. Cain, N. Solis, and S. J. Cordwell, "Beyond gene expression: The impact of protein post-translational modifications in bacteria," *Journal of Proteomics*, vol. 97. pp. 265–286, 31-Jan-2014.

[189] B. Wallmeyer, S. Trinschek, S. Yigit, U. Thiele, and T. Betz, "Collective Cell Migration in Embryogenesis Follows the Laws of Wetting," *Biophys. J.*, vol. 114, no. 1, pp. 213–222, Jan. 2018.

[190] P. L. Biancaniello, A. J. Kim, and J. C. Crocker, "Colloidal interactions and self-assembly using DNA hybridization," *Phys. Rev. Lett.*, vol. 94, no. 5, p. 058302, Feb. 2005.

[191] E. Spruijt, H. E. Bakker, T. E. Kodger, J. Sprakel, M. A. Cohen Stuart, and J. Van Der Gucht, "Reversible assembly of oppositely charged hairy colloids in water," *Soft Matter*, vol. 7, no. 18, pp. 8281–8290, Sep. 2011.

[192] R. a. Foty and M. S. Steinberg, "The differential adhesion hypothesis: a direct evaluation," *Dev. Biol.*, vol. 278, no. 1, pp. 255–263, 2005.

[193] C. K. Ellison *et al.*, "Obstruction of pilus retraction stimulates bacterial surface sensing," *Science (80-.).*, vol. 358, no. 6362, 2017.

[194] D. L. Higashi, S. W. Lee, A. Snyder, N. J. Weyand, A. Bakke, and M. So, "Dynamics of Neisseria gonorrhoeae attachment: Microcolony development, cortical plaque formation, and cytoprotection," *Infect. Immun.*, vol. 75, no. 10, pp. 4743–4753, 2007.

[195] E. Matteoli and G. Ali Mansoori, "A simple expression for radial distribution functions of pure fluids and mixtures," *J. Chem. Phys.*, vol. 103, no. 11, pp. 4672–4677, Sep. 1995.

[196] M. Bergman, G. Del Prete, Y. van Kooyk, and B. Appelmelk, "Helicobacter pylori phase variation, immune modulation and gastric autoimmunity," *Nat. Rev. Microbiol.*, vol. 4, no. 2, pp. 151–159, Feb. 2006.

[197] F. Bidmos and C. Bayliss, “Genomic and Global Approaches to Unravelling How Hypermutable Sequences Influence Bacterial Pathogenesis,” *Pathogens*, vol. 3, no. 1, pp. 164–184, Feb. 2014.

[198] A. K. Criss and H. S. Seifert, “A bacterial siren song: Intimate interactions between Neisseria and neutrophils,” *Nature Reviews Microbiology*, vol. 10, no. 3. pp. 178–190, 31-Mar-2012.

[199] J. L. Brooks and K. K. Jefferson, “Phase Variation of Poly-N-Acetylglucosamine Expression in Staphylococcus aureus,” *PLoS Pathog.*, vol. 10, no. 7, p. e1004292, Jul. 2014.

[200] R. D. Monds and G. A. O’Toole, “The developmental model of microbial biofilms: ten years of a paradigm up for review,” *Trends in Microbiology*, vol. 17, no. 2. Elsevier Current Trends, pp. 73–87, 01-Feb-2009.

[201] J. J. Dong and S. Klumpp, “Simulation of colony pattern formation under differential adhesion and cell proliferation,” *Soft Matter*, vol. 14, no. 10, pp. 1908–1916, 2018.

[202] W. Kim, F. Racimo, J. Schluter, S. B. Levy, and K. R. Foster, “Importance of positioning for microbial evolution.,” *Proc. Natl. Acad. Sci. U. S. A.*, vol. 111, no. 16, pp. E1639-47, 2014.

[203] J. Schluter, C. D. Nadell, B. L. Bassler, and K. R. Foster, “Adhesion as a weapon in microbial competition,” *ISME J.*, vol. 9, no. 1, pp. 139–149, 2015.

[204] R. Lehe, O. Hallatschek, and L. Peliti, “The rate of beneficial mutations surfing on the wave of a range expansion.,” *PLoS Comput. Biol.*, vol. 8, no. 3, p. e1002447, Mar. 2012.

[205] J. M. J. Travis, T. Münkemüller, O. J. Burton, A. Best, C. Dytham, and K. Johst, “Deleterious mutations can surf to high densities on the wave front of an expanding population,” *Mol. Biol. Evol.*, vol. 24, no. 10, pp. 2334–2343, 2007.

[206] R. E. Lenski and M. Travisano, “Dynamics of adaptation and diversification: a 10,000-generation experiment with bacterial populations.,” *Proc. Natl. Acad. Sci.*, vol. 91, no. 15, pp. 6808–6814, Jul. 1994.

[207] B. H. Good, M. J. McDonald, J. E. Barrick, R. E. Lenski, and M. M. Desai, “The dynamics of

molecular evolution over 60,000 generations," *Nature*, vol. 551, no. 7678, pp. 45–50, Oct. 2017.

[208] Z. D. Blount, C. Z. Borland, and R. E. Lenski, "Historical contingency and the evolution of a key innovation in an experimental population of Escherichia coli," *Proc. Natl. Acad. Sci.*, vol. 105, no. 23, pp. 7899–7906, Jun. 2008.

[209] Z. D. Blount, J. E. Barrick, C. J. Davidson, and R. E. Lenski, "Genomic analysis of a key innovation in an experimental Escherichia coli population," *Nature*, vol. 489, no. 7417, pp. 513–518, Sep. 2012.

[210] M. Lukačišinová and T. Bollenbach, "Toward a quantitative understanding of antibiotic resistance evolution," *Current Opinion in Biotechnology*, vol. 46. Elsevier Current Trends, pp. 90–97, 01-Aug-2017.

[211] M. Luksza and M. Lässig, "A predictive fitness model for influenza.," *Nature*, vol. 507, no. 7490, pp. 57–61, Mar. 2014.

[212] D. H. Morris *et al.*, "Predictive Modeling of Influenza Shows the Promise of Applied Evolutionary Biology," *Trends in Microbiology*, 2017.

[213] D. B. Kearns, F. Chu, S. S. Branda, R. Kolter, and R. Losick, "A master regulator for biofilm formation by Bacillus subtilis," *Mol. Microbiol.*, vol. 55, no. 3, pp. 739–749, Dec. 2004.

[214] L. Friedman and R. Kolter, "Genes involved in matrix formation in Pseudomonas aeruginosa PA14 biofilms," *Mol. Microbiol.*, vol. 51, no. 3, pp. 675–690, Dec. 2004.

[215] T. Abee, Á. T. Kovács, O. P. Kuipers, and S. van der Veen, "Biofilm formation and dispersal in Gram-positive bacteria," *Current Opinion in Biotechnology*, vol. 22, no. 2. Elsevier Current Trends, pp. 172–179, 01-Apr-2011.

[216] A. Dragoš *et al.*, "Division of Labor during Biofilm Matrix Production," *Curr. Biol.*, vol. 28, no. 12, p. 1903–1913.e5, Jun. 2018.

[217] J. V. a N. Gestel, H. Vlamakis, and R. Kolter, "Division of Labor in Biofilms : the Ecology of Cell Differentiation," *Microbiol. Spectr.*, vol. 3, no. 2, pp. 1–24, Apr. 2015.

[218] K. Schwarze, J. Buchanan, J. C. Taylor, and S. Wordsworth, "Are whole-exome and whole-genome sequencing approaches cost-effective? A systematic review of the

literature," *Genet. Med.*, Feb. 2018.

[219] S. T. Park and J. Kim, "Trends in next-generation sequencing and a new era for whole genome sequencing," *International Neurourology Journal*, vol. 20, no. Suppl 2. Korean Continence Society, pp. 76–83, Nov-2016.

[220] J. J. Power *et al.*, "Fairly free recombination between subspecies of Bacillus subtilis," *Unpubl. Manuscr. Prep.*, 2018.

[221] D. P. J. Turner, K. G. Wooldridge, and D. A. A. Ala'Aldeen, "Autotransported serine protease A of Neisseria meningitidis: An immunogenic, surface-exposed outer membrane, and secreted protein," *Infect. Immun.*, vol. 70, no. 8, pp. 4447–4461, Aug. 2002.

[222] T. N. Mandal, A. A. Mahdi, G. J. Sharples, and R. G. Lloyd, "Resolution of Holliday intermediates in recombination and DNA repair: Indirect suppression of ruvA, ruvB, and ruvC mutations," *J. Bacteriol.*, vol. 175, no. 14, pp. 4325–4334, Jul. 1993.

[223] A. Jamet and X. Nassif, "Characterization of the Maf family of polymorphic toxins in pathogenic Neisseria species," *Microb. Cell*, vol. 2, no. 3, pp. 88–90, Mar. 2015.

[224] A. Hollander, A. D. Mercante, W. M. Shafer, and C. N. Cornelissen, "The iron-repressed, AraC-like regulator MpeR activates expression of fetA in Neisseria gonorrhoeae," *Infect. Immun.*, vol. 79, no. 12, pp. 4764–4776, Dec. 2011.

[225] O. Otto *et al.*, "Real-time particle tracking at 10,000 fps using optical fiber illumination.," *Opt. Express*, vol. 18, no. 22, pp. 22722–22733, 2010.

[226] T.-W. Su, L. Xue, and A. Ozcan, "High-throughput lensfree 3D tracking of human sperms reveals rare statistics of helical trajectories," *Proc. Natl. Acad. Sci.*, vol. 109, no. 40, pp. 16018–16022, 2012.

[227] L. G. Wilson, L. M. Carter, and S. E. Reece, "High-speed holographic microscopy of malaria parasites reveals ambidextrous flagellar waveforms," *Proc. Natl. Acad. Sci.*, vol. 110, no. 47, pp. 18769–18774, 2013.

[228] J. F. Jikeli *et al.*, "Sperm navigation along helical paths in 3D chemoattractant landscapes," *Nat. Commun.*, vol. 6, 2015.

[229] C. V Rao, J. R. Kirby, and A. P. Arkin, “Design and diversity in bacterial chemotaxis: A comparative study in Escherichia coli and Bacillus subtilis,” *PLoS Biol.*, vol. 2, no. 2, p. e49, Feb. 2004.

[230] G. A. O’Toole and R. Kolter, “Flagellar and twitching motility are necessary for Pseudomonas aeruginosa biofilm development,” *Mol. Microbiol.*, vol. 30, no. 2, pp. 295–304, Oct. 1998.

[231] S. Kolappan, M. Coureuil, X. Yu, X. Nassif, E. H. Egelman, and L. Craig, “Structure of the Neisseria meningitidis Type IV pilus,” *Nat. Commun.*, vol. 7, 2016.

10 LIST OF FIGURES

11 LIST OF TABLES

12 DANKSAGUNG

Ich möchte allen Personen, die mich auf dem Weg zu dieser Arbeit begleitet haben, aufrichtig danken.

Insbesondere danke ich **Prof. Dr. Berenike Maier** für die exzellente Betreuung und das Vertrauen. Mir war es eine große Freude gemeinsam in dem spannenden Feld der Biophysik zu arbeiten und frei zu forschen. Ich habe es durchweg genossen Teil der AG-Maier zu sein.

Ich danke **Prof. Dr. Tobias Bollenbach** für das Interesse und die Bereitschaft Zweitgutachter in meinem Prüfungskomitee zu sein.

Prof. Dr. Andreas Schadschneider danke ich für die nochmalige Zusammenarbeit, das Interesse und das Übernehmen des Prüfungsvorsitzes.

Ich danke allen ehemaligen, aktuellen und zukünftigen Mitgliedern der AG Maier. Ein besonderes Dankeschön dem …

… Team Support, **Thorsten**, **Gaby** und **Christina**, …

… dem Team Bacillus, **Jeff**, **Melih**, **Isabel** und **Mona**, …

… dem Team Gonorrhoeae, **Tom**, **Niklas**, **Marc**, **Sebastian**, **Anton**, …

…und den ehemaligen Gruppenmitgliedern, besonders **Enno**, **Christof**, **Nadzeya**, **Lena**, **Katja**, **Jan**, **Katja** und **Claudia,** …

für die Freude, eure Unterstützung, eure Hilfsbereitschaft und den Spaß den wir hatten und noch haben werden.

Herzlich danke ich **Lea** (blub-blub) und meiner großartigen **Familie** für die Aufmunterung, den Rückhalt und das Immerdasein. Ohne euch wäre ich nicht hier.

13 ERKLÄRUNG

Ich versichere, dass ich die von mir vorgelegte Dissertation selbständig angefertigt, die benutzten Quellen und Hilfsmittel vollständig angegeben und die Stellen der Arbeit einschließlich Tabellen, Karten und Abbildungen, die anderen Werken im Wortlaut oder dem Sinn nach entnommen sind, in jedem Einzelfall als Entlehnung kenntlich gemacht habe; dass diese Dissertation noch keiner anderen Fakultät oder Universität zur Prüfung vorgelegen hat; dass sie abgesehen von unten angegebenen Teilpublikationen noch nicht veröffentlicht worden ist sowie, dass ich eine solche Veröffentlichung vor Abschluss des Promotionsverfahrens nicht vornehmen werde. Die Bestimmungen der Promotionsordnung sind mir bekannt. Die von mir vorgelegte Dissertation ist von Frau Prof. Dr. Berenike Maier betreut worden.

Teilpublikationen:

R. Zöllner*, E. R. Oldewurtel*, N. Kouzel, and B. Maier, “Phase and antigenic variation govern competition dynamics through positioning in bacterial colonies,” *Sci. Rep.*, vol. 7, no. 1, p. 12151, 2017.

A. Welker*, T. Cronenberg*, R. Zöllner* *et al.*, “Molecular Motors Govern Liquidlike Ordering and Fusion Dynamics of Bacterial Colonies,” *Phys. Rev. Lett.*, vol. 121, no. 11, p. 118102, Sep. 2018.

R. Zöllner*, T. Cronenberg*, N. Kouzel, A. Welker, M. Koomey, and B. Maier, “Type IV pilin post-translational modifications modulate materials properties of bacterial colonies,” *bioRxiv*, p. 389882, Aug. 2018.

R. Zöllner*, T. Cronenberg* and B. Maier, “Motor properties of PilT-independent type 4 pilus retraction in gonococci,” *in preparation*

*Equal contributions

Köln, den ………………… …………………………..
Robert Zöllner